UNIVERSITY OF CALIFORNIA, SAN DIEGO

Insights from Molecular Simulations and Multi-Scale Mathematical Modeling of Biological Systems

A dissertation submitted in partial satisfaction of the requirements for the degree of Doctor of Philosophy

in

Chemistry with Specialization in Multi-Scale Biology

by

Vincent Tyler Metzger

Committee in charge:

Professor Andrew McCammon, Chair
Professor Andrew McCulloch
Professor Michael Galperin
Professor Elizabeth Komives
Professor Wei Wang

2014

The dissertation of Vincent Tyler Metzger is approved, and it is acceptable in quality and form for publication on microfilm and electronically:

Chair

University of California, San Diego

2014

Table of Contents

List of Figures

List of Tables

List of Abbreviations

AIDS - Acquired immune deficiency syndrome
AMD – Accelerated molecular dynamics
ART – Antiretroviral therapy
CMD – Conventional molecular dynamics
DHFR – Dihydrofolate Reductase
DHFR-TS – Dihydrofolate Reductase – Thymidylate Synthase
GPU – Graphical processing unit
HIV – Human immunodeficiency virus
IDU – Injection drug users
MD – Molecular dynamics
ODE – Ordinary differential equation
PDB – Protein data bank
PME – Particle mesh Ewald
PMF – Potential of mean force
PC – Principal component
PCA – Principal component analysis
RMSD – Root mean square deviation
RMSF – Root mean square fluctuations
SERCA - Sarcoplasmic reticulum Ca^{2+} ATPase
SAC – Sexual activity class
TIP – Therapeutic Interfering Particles
TM – Transmembrane
TS – Thymidylate Synthase
UNAIDS – United Nations AIDS Organization

Acknowledgements

I begin by thanking Professor J. Andrew McCammon who served as my advisor and as the committee chair for his support, encouragement, enthusiasm for lifelong learning and exceptional mentorship during my time in his lab. I thank my parents Janet Metzger and Louis Metzger III, my brothers Dr. Louis E. Metzger IV and Jack M. Metzger, and Jennifer Pomponio for their unconditional love and support during my graduate education. I thank my thesis committee members Prof. Wei Wang, Prof. Elizabeth A. Komives, Prof. Andrew D. McCulloch, and Prof. Michael Galperin for their roles as mentors and for their time and effort serving on my committee. I also thank Professor Leor Weinberger (currently at UCSF) for providing me with mentorship, guidance, and training during my first two years at UCSD. Additionally, I thank fellow University of New Mexico alumni Samuel Hopkins for insightful discussions and advice regarding computer science and engineering, respectively. I thank Dr. Louis E. Metzger IV for his valuable advice throughout graduate school and for sharing his contagious enthusiasm for scientific research.

I was fortunate to collaborate with many talented and enthusiastic researchers at UCSD including Dr. Pete Kekenes-Huskey, Dr. Changsun Eun, Dr. Sara E. Nichols, Dr. Yinglong Miao, Dr. Paul M. Gasper, Dr. Gary Huber, and Prof. James O. Lloyd-Smith (UCLA). I was also fortunate to have knowledgeable, experienced, and friendly co-workers such as Brian Fox, Patti Craft, Patrick Blachly, Dr. Mehrnoosh Arrar, Dr. Steffen Lindert, Dr. Kate Rogers, Nuo Wang, and other members of the McCammon lab.

I am especially thankful for the generous funding that I received from the HHMI Interfaces Training Grant, the UCSD Department of Chemistry and Biochemistry, and from the McCammon Lab. This funding and training was crucial to my success as a graduate student.

I would like to dedicate this dissertation to my parents Janet Metzger and Louis Metzger III for always encouraging me to pursue my dreams.

Chapter 2 is a minimally modified reprint of the material as it appears in Kekenes-Huskey PM*, Metzger, VT*, Grant BJ, McCammon JA. Calcium Binding and Allosteric Signaling Mechanisms for Sarcoplasmic Reticulum Ca^{2+} ATPase (SERCA). Protein Science. Oct;21(10):1429-43. doi: 10.1002/pro.2129. (2012) *Metzger VT and Kekenes-Huskey PM contributed equally to this research. I served as a primary investigator and author of this publication.

Chapter 3 is a minimally modified reprint of the material as it appears in Vincent T Metzger*, Changsun Eun*, Peter M. Kekenes-Huskey, Gary Huber, and J. Andrew McCammon. Electrostatic substrate channeling in P.falciparum DHFR-TS: Brownian dynamics simulations and continuum models. 2014 [Submited to Biophysical Journal – currently in review]. I served as the primary investigator and author of this publication.

Chapter 4 is a minimally modified reprint of the material as it appears in Metzger VT, Lloyd-Smith JO, Weinberger LS (2011). Autonomous Targeting of Infectious Superspreaders Using Engineered Transmissible Therapies. PLoS Computational Biology 7(3): e1002015. doi:10.1371/journal.pcbi.1002015. I was the primary investigator and author of this publication.

Vita

2009 B.A. in Chemistry with Minor in Mathematics
University of New Mexico

2011 M.S. in Chemistry
University of California, San Diego

2014 Ph.D. in Chemistry with Specialization in Multi-Scale Biology
University of California, San Diego

Publications

Metzger VT, Lloyd-Smith JO, Weinberger LS. (2011). Autonomous Targeting of Infectious Superspreaders Using Engineered Transmissible Therapies. PLoS Computational Biology. March 17; 7(3): e1002015. doi:10.1371/journal.pcbi.1002015

Kekenes-Huskey PM*, **Metzger, VT***, Grant BJ, McCammon JA. (2012). Calcium Binding and Allosteric Signaling Mechanisms for Sarcoplasmic Reticulum Ca^{2+} ATPase (SERCA). Protein Science. Oct;21(10):1429-43. doi: 10.1002/pro.2129.
*Authors contributed equally

Miao Y, Nichols SE, Gasper PM, **Metzger VT**, McCammon JA. (2013). Activation and dynamic network of the M2 muscarinic receptor. Proc. Natl. Acad. Sci. U.S.A. July 2;110(27):10982-7. doi: 10.1073/pnas.1309755110.

Eun C, Kekenes-Huskey PM, **Metzger VT**, McCammon JA. (2014). A model study of sequential enzyme reactions and electrostatic channeling. The Journal of Chemical Physics. March 20; 140, 105101; doi: 10.1063/1.4867286

Metzger VT*, Changsun Eun*, Kekenes-Huskey PM, Gary Huber, McCammon JA. (2014). Electrostatic channeling in *P.falciparum* DHFR-TS: Brownian dynamics and continuum modeling. [Biophysical Journal – accepted with minor revisions]
*Authors contributed equally

ABSTRACT OF THE DISSERTATION

Insights from Molecular Simulations and Multi-Scale
Mathematical Modeling of Biological Systems

by

Vincent Tyler Metzger

Doctor of Philosophy in Chemistry with Specialization in Multi-Scale Biology

University of California, San Diego, 2014

Professor Andrew McCammon, Chair

The techniques of Molecular Dynamics (MD) as well as Accelerated MD (AMD) are established computational methods for investigating the motions of biomolecules that can be successfully applied to large systems to achieve enhanced conformational sampling. Chapter 1 also introduces Brownian dynamics simulations for studying the diffusional encounter of ions or small molecules with binding sites. Additionally, the use of coupled ordinary differential equations (ODEs) enables mathematical modeling of complex biological systems at a variety of scales. In Chapter 2, AMD simulations are applied to the transmembrane Sarcoplasmic Reticulum Ca^{2+} ATPase (SERCA), a calcium pump that utilizes energy from ATP hydrolysis to drive calcium ions across a concentration gradient. The enhanced conformational sampling achieved with AMD allows identification of collective motions that partition SERCA crystallographic structures into several catalytically unique states and also supports the role of Glu309 gating in Ca^{2+} binding. Brownian dynamics simulations demonstrate the important contribution of surface-exposed, polar residues in the diffusional encounter of Ca^{2+} with SERCA. In chapter 3, Brownian dynamics simulations as well as continuum models of the

bifunctional *Plasmodium falciparum* dihydrofolate reductase-thymidylate synthase (*P. falciparum* DHFR-TS) are used to explore electrostatic-mediated substrate channeling. The results indicate that electrostatic-mediated channeling in this system is (~15% - 25%) at physiological pH and ionic strength and that removing the electric charges from key basic residues significantly reduces the electrostatic-mediated channeling efficiency of *P. falciparum* DHFR-TS. Subtle differences in structure, active-site geometry, and charge distribution in protozoan DHFR-TS enzymes appears to influence both electrostatic-mediated as well as proximity-mediated substrate channeling. In chapter 4, multi-scale mathematical models are used to study the dynamics of a hypothetical anti-HIV genetic therapy at the molecular, within-cell, within-host, and epidemiological scales. This multi-scale approach allows us to make predictions about ideal design parameters for a hypothetical anti-HIV genetic therapy. Our models show that a specific genetic therapy could autonomously target infectious superspreaders at the epidemiological scale, possibly lowering HIV/AIDS prevalence significantly. In chapter 5, insights into the systems detailed in the previous chapters are briefly discussed with an emphasis on the importance of both molecular simulations as well as multi-scale mathematical modeling.

Chapter 1: Molecular Simulations and Multi-Scale Mathematical Modeling to Study Complex Biological System

Introduction

For several decades, researchers have detailed the importance of constant changes in protein structure caused by thermal fluctuations of individual atoms that can promote fundamental biomolecular processes including enzyme catalysis, allosteric regulation of proteins and enzymes, and even molecular transport. It is now clear that detailed knowledge of molecular dynamics is crucial to understand protein function. As the number of solved biomolecular structures continues to increase, experiments and simulations exploring molecular dynamics will become increasingly important in identifying and studying the ensemble of intermediate conformations traversed by a protein at biologically relevant timescales and temperatures between experimentally determined structures with known atomic coordinates. This ensemble of biologically important conformations has often been finely tuned by the process of evolution to optimize specific biomolecular processes and is not random. An underlying potential energy surface (PES) exists which governs the kinetics and thermodynamics of protein conformational transitions. This PES originates from a very complex array of both intramolecular and intermolecular forces. In order to facilitate predictions capable of describing PES features, classical force fields have been constructed to model these forces at the atomic scale. Over the past few decades, these force fields have been improved significantly in support of molecular dynamics (MD) simulations that model protein dynamics via the iterative application of Newton's equations of motion from force field energies. The molecular trajectories obtained through MD simulations can provide

computational biochemists with detailed information regarding the predicted internal dynamics of biomolecules and associated insights into protein function.

While molecular simulation techniques can yield useful information about the dynamics of a system, sometimes it can also be advantageous to construct mathematical models using ordinary differential equations (ODEs) to track the dynamics of biologically important phenomenon at scales other than the molecular scale. Systems of ODEs describing dynamics at multiple biological scales can sometimes be linked in a manner that allows system dynamics at multiple scales to be considered in a multi-scale model. When possible, steady-state algebraic solutions to a system of ODEs describing the dynamics of a biological scale are incorporated into a system of ODEs describing another scale of the multi-scale biological model. If the dynamics of a biological scale are very complex and there is no apparent exact algebraic steady-state solution to the system, this scale can still be included in a multi-scale model by taking advantage of numerical integration techniques to gain insights into the solution space. Although multi-scale mathematical modeling of biological systems can be a powerful technique for theoretical and computational biochemists, the accuracy of a multi-scale biological model is sensitive to the accuracy (and existence) of experimentally measured parameters as well as experimentally verified relationships between state variables.

Molecular Dynamics Simulations

Molecular dynamics (MD) simulations are now considered to be a well-established technique for exploring the dynamics of biomolecules. To perform MD simulations, atomic structures usually obtained via x-ray crystallography or NMR are subjected to Newton's equations of motion propagated for each atom in the structure using relatively short (~femtosecond) time-steps where forces do not change significantly. For each time-step, the force active on each atom i is calculated from the gradient of the potential energy, F_i =

$-\nabla_i V(r)$, as determined by a molecular force field. In these force fields, deviations from equilibrium bond lengths and angles are modeled as perturbations of harmonic springs. Forces resulting from rotation about dihedral angles are accounted for via the addition of a periodicity term. The non-bonded van der Waals forces are modeled by a Lennard-Jones "6-12" potential term. Electrostatic interactions are accounted for in a Columbic term. The summation of these energetic terms gives the total potential, *V(r)* as shown in the equation below:

$$V(r) = \sum_{bonds} K_b(b - b_0)^2 + \sum_{angles} K_{\boldsymbol{\theta}}(\theta - \theta_0)^2 + \sum_{dihedrals} K_{\emptyset}\cos(n\emptyset - \gamma) + \sum_{van\ der\ Waals} \varepsilon_{ij}\left(\frac{A}{r_{ij}^{12}} - \frac{B}{r_{ij}^{6}}\right) + \sum_{electrostatic} \frac{q_i q_j}{\varepsilon_D r_{ij}}$$

When a molecular dynamics simulation achieves sufficient sampling, the resulting trajectory is said to be ergodic and representative of the ensemble of structures associated with the specified conditions of the MD simulation. As the number of atoms in a hypothetical MD simulation is increased, additional degrees of freedom are added to the system, resulting in an increase in the computational expense needed to perform *n* time-steps. Sometimes in large systems (such as SERCA imbedded in a phospholipid bilayer) which contain hundreds of thousands of atoms, advanced computational techniques such as parallelization and the use of graphical processing units (GPUs) for floating point calculations are necessary in order to obtain MD trajectories in the tens-to-hundreds of nanoseconds time-frame using available computational resources.

Although the detailed description of protein dynamics gained from conventional molecular dynamics (CMD) simulations can be extremely useful in understanding potential mechanisms of protein or enzyme function, unfortunately many biochemically interesting

protein dynamics cannot be well-explored by CMD in systems that either contain a large number of atoms and/or proteins in systems that make use of long-timescale dynamical events.

Accelerated molecular dynamics simulations

As mentioned in the above section, conformational sampling using CMD in large systems or systems that exhibit slow dynamics is normally limited by available computational resources. In order to explore the dynamics in such systems, it is necessary to achieve enhanced conformational sampling during the course of the MD simulation so that interesting dynamics can be observed in the resulting MD trajectory. Fortunately, numerous methods of enhanced sampling have been developed. One such method is accelerated molecular dynamics (AMD). When performing AMD simulations, the potential energy at each sampled conformation, *V(r)*, is modified by the addition of a boost energy $\nabla V(r)$ when the energy falls below a cutoff E (Fig. 1-1).

$$V^*(r) = \begin{Bmatrix} V(r), V(r) \geq E \\ V(r) + \Delta V(r), V(r) < E \end{Bmatrix}$$

$$\Delta V(r) = \frac{\left(E - V(r)\right)^2}{\alpha + (E - V(r))}$$

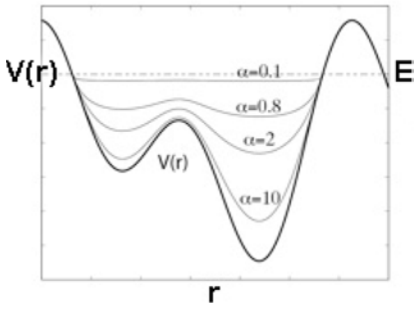

Figure 1-1. Hypothetical two-dimensional representations of AMD potential energy surfaces for increasing values of α with the same cutoff, E.

The modified potential, V*(r), is raised and flattened based on the value of α, which increases the probability of transitions between low energy states. The strength of the boost is determined by the depth of an energy well (the difference between E and V) as well as the 'tuning parameter" α which modifies the overall extent of flattening. The corrected canonical ensemble average of the AMD system can theoretically be obtained via reweighting each point by the strength of the Boltzmann factor of the bias energy, $\exp[\beta \Delta V(r)]$.

Although increasing the value of the boost energy increases conformational sampling of the system, "over-acceleration" may lead to poor statistics after reweighting because this causes high-energy conformations to be over-sampled. Also, over-acceleration is known to induce abnormal loss of secondary structure in some protein systems and can cause simulated phospholipid bilayers to separate. Therefore, it is necessary to sample a variety of acceleration factors in order to optimize AMD for each system being investigated.

Molecular simulations and multi-scale mathematical modeling of biological systems

In addition to molecular simulation methods such as CMD and AMD, multi-scale mathematical models are used to describe the proposed three-step process of Ca^{2+} diffusion from bulk solvent, recognition, and binding to the calcium-binding sites located in the transmembrane region of the SERCA Ca^{2+} pump in Chapter 2. Utilizing coupled systems of ordinary differential equations (ODEs), multi-scale mathematical modeling is also used in a separate investigation (Chapter 4) to construct a detailed mathematical framework capable of predicting the efficacy of a hypothetical genetic therapy targeting HIV infection at the molecular, cellular, within-host, and epidemiological scales. This mathematical framework can also be used to predict the efficacy of other hypothetical HIV interventions and could even be re-parameterized to track the viral dynamics of other retroviruses with the objective of predicting the efficacy of a hypothetical antiviral intervention. In Chapter 3, another molecular simulation method

(Brownian dynamics) is also used to investigate electrostatic-mediated channeling of the charged intermediate dihydrofolate from the thymidylate-synthase active site to the dihydrofolate-reductase active site of the bifunctional DHFR-TS enzyme from *Plasmodium falciparum*, the protozoan species associated with the majority of malaria infections worldwide.

Chapter 2: Calcium Binding and Allosteric Signaling Mechanisms for Sarcoplasmic Reticulum Ca^{2+} ATPase (SERCA)

Abstract

The sarcoplasmic reticulum Ca^{2+} ATPase (SERCA) is a membrane-bound pump that utilizes ATP to drive calcium ions from the myocyte cytosol against the higher calcium concentration in the sarcoplasmic reticulum. Conformational transitions associated with Ca^{2+}-binding are important to its catalytic function. We have identified collective motions that partition SERCA crystallographic structures into multiple catalytically-distinct states using principal component analysis. Using Brownian dynamics simulations, we demonstrate the important contribution of surface-exposed, polar residues in the diffusional encounter of Ca^{2+}. Molecular dynamics simulations indicate the role of Glu309 gating in binding Ca^{2+}, as well as subsequent changes in the dynamics of SERCA's cytosolic domains. Together these data provide structural and dynamical insights into a multistep process involving Ca^{2+} binding and catalytic transitions.

Introduction

The regulation of Ca^{2+} transport by ion channels, pumps, and exchangers is of crucial importance to excitation-contraction coupling in muscle cells. The sarcoplasmic reticulum Ca^{2+}ATPase (SERCA) is a transmembrane (TM) Ca^{2+} pump that transports two Ca^{2+} into the sarcoplasmic reticulum from the cytosol through ATP-dependent conformational transitions. This transport process is characterized by four sequential catalytic states (E1, E1P, E2P, and E2) with each having a distinct conformation [1]. E1 comprise the cytosol-facing, Ca^{2+}-free, and bound states (which we label as E1, E1(Ca), respectively); binding of ATP and subsequent

phosphorylation gives rise to the E1P state. E2P is obtained after the E1P state undergoes a transition that exposes bound Ca^{2+} to the SR lumen, after which liberation of the phosphate ion and Ca^{2+} to the lumen yields the E2 state. The pump finally exposes the empty Ca^{2+} ligand binding domain to the cytosol, whereby binding of cytosolic Ca^{2+} completes the cycle and returns SERCA to the E1 state. Understanding the E1→E1P transition thus provides insight into the calcium-dependent aspects of SERCA function during muscle relaxation.

Electron paramagnetic resonance, Forster resonance energy transfer, and X-ray crystallography of the four catalytic states [1-5] of SERCA have identified several components involved in its catalytic activity. These include transmembrane (TM) bundle helices M1 to M10, which bind Ca^{2+}, while the cytosolic domains N, P, and A are responsible for ATP binding and hydrolysis. (Fig. 2-1) [6]. Upon $Ca^{2+}$and ATP binding, shifts in transmembrane helices M4 and M2, bending of M1, and closing of the A and N cytosolic domains are suggested to promote interchange between the E1(Ca) and the E1P states [1]; these studies have furthermore identified two Ca^{2+} binding pockets (site I and site II) and residues implicated in Ca^{2+} coordination.

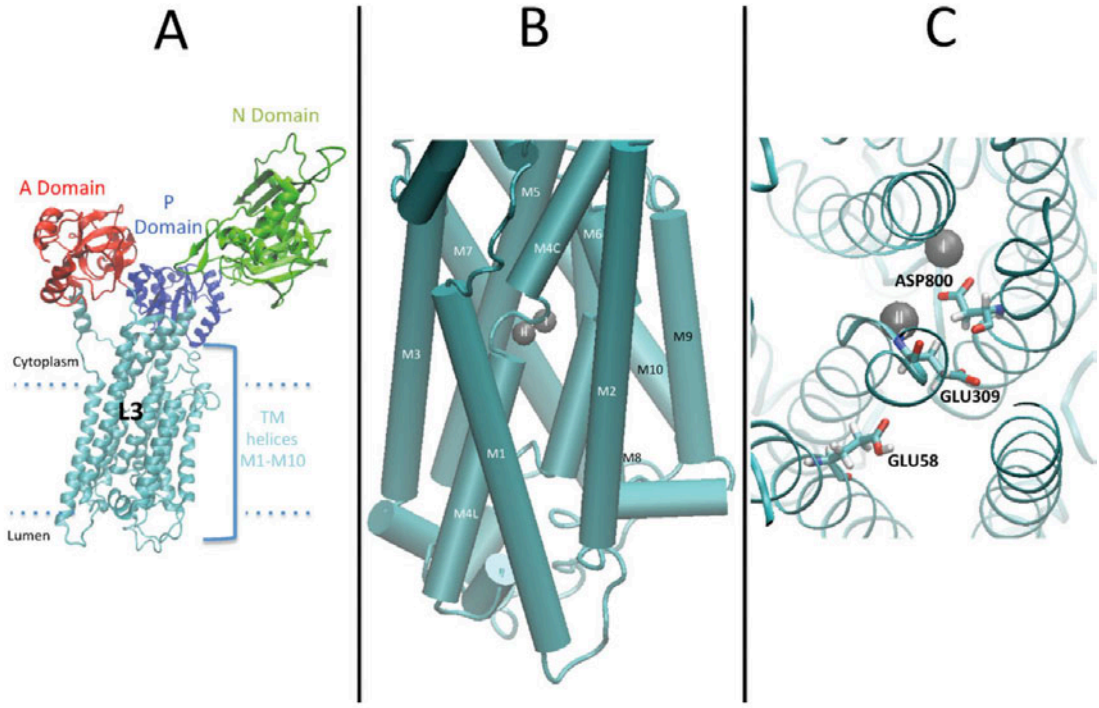

Figure 2-1. *a)* Holo SERCA (PDB ID 1SU4) showing the N, A, and P domains as well as the transmembrane helices *(teal)*. *b)* Transmembrane region of SERCA with important TM helices labeled. *c)* Holo SERCA (PDB ID 1SU4) with both Ca^{2+} ions bound *(gray)* surrounded by several coordinating residues (licorice representation).

Experiments and simulations have unveiled several key points regarding the cooperative binding of Ca^{2+}. The first calcium is known to bind to site I, which is buried deep with the TM region, and is followed by a second calcium binding to site II, which is closest to the cytoplasm [7]. Binding of calcium to site I increases the calcium affinity of site II, whereupon binding of a second Ca^{2+} is necessary for ATP hydrolysis and continuation of the reaction cycle [1]. Simulations of Ca^{2+} binding to SERCA [8] also indicate that Ca^{2+} binds first at site I, then site II. Bridging site II and the cytoplasm are solvent-exposed acidic residues thought to be involved in Ca^{2+} gating (M4: E309), [9] or recognition (M1: E51, E55, E58, D59 [10] and M2: D109 [11]) Fig. 2-1). Residues comprising the cytosolic loops between M6 and M7 (L67) as well as M8 and M9 (L89) have also been implicated in Ca^{2+} binding and ATP turnover and include D813, D815, and D818 [12]. However, it remains unclear to what extent these acidic residues are directly involved in Ca^{2+} gating and binding, and moreover, how this binding signal is communicated to the cytosolic domains responsible for ATP hydrolysis.

Molecular dynamics simulations of SERCA have provided substantial insight into the relationship between protein structure and mechanisms of substrate binding, selectivity, and conformational motions. Simulations by Musgaard *et al.,* [13] Huang *et al.,* [8] and Costa *et al.,* [14] have explored possible pathways of Ca^{2+} entry. Specifically, the regions near L67/L89 and M1/M2/M4 have been suggested as predominant pathways for Ca^{2+} binding, which we describe as L1 and L3, respectively (according to the convention in Huang *et al*.), based on MD and solutions of the Poisson-Boltzmann equation. Other simulations have focused on the Ca^{2+} binding domain, thereby, uncovering the importance of particular coordination residues and their protonation states in stabilizing Ca^{2+} [15,16]. Additionally, a recent simulation [17] demonstrated coupling between Ca^{2+} binding and closing of the A and N domains associated with conversion between the E1(Ca) and E1P states. While these studies constitute substantial progress in clarifying the Ca^{2+}-dependent steps of SERCA catalytic activity, the coupling

between bulk Ca^{2+} association with SERCA and subsequent catalytic activity has not been well-explored.

We sought to provide a comprehensive and quantitative picture that links Ca^{2+} binding to the protein with important conformational motions, taking into account the role of electrostatic interactions, diffusion into the binding site, and allosteric signaling of the A and N domains (Fig. 2-2). Here, we combine Brownian dynamics to probe Ca^{2+} binding to the outer SERCA surface, umbrella sampling to explore pathways leading from the SERCA surface to site II, and molecular dynamics (MD) to examine allosteric activity associated with Ca^{2+} binding. We focus in particular on the contributions of acidic surface residues along L3, in particular the role of the gating residue E309, which together we hypothesize serve as recognition residues for guiding Ca^{2+} association.

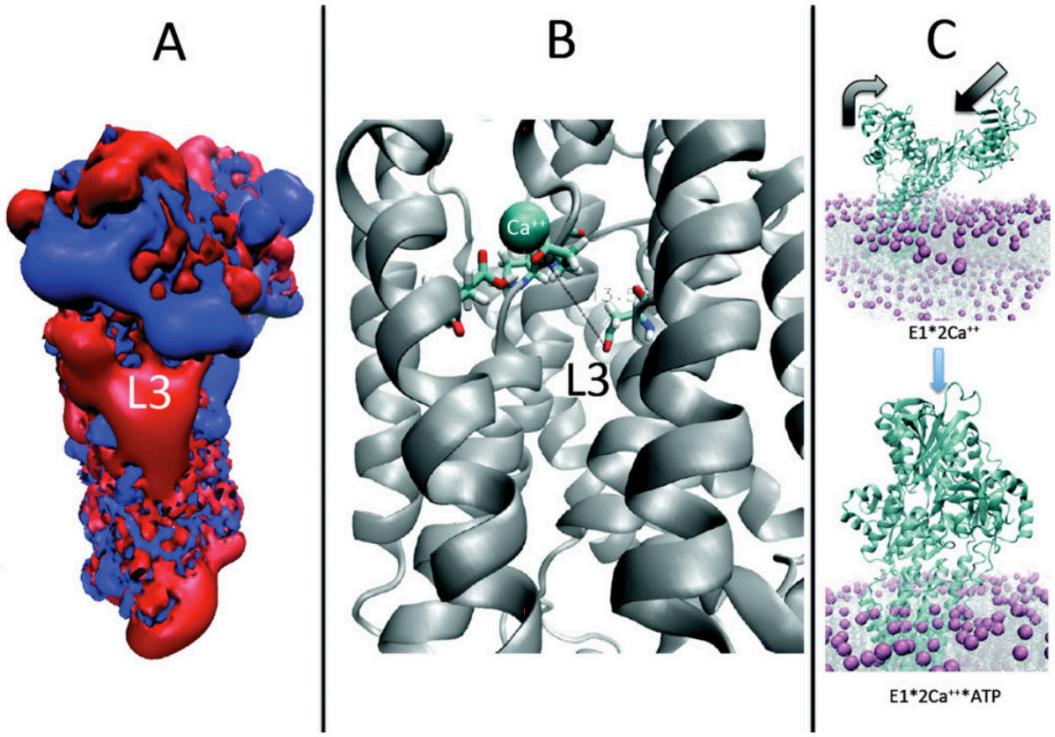

Figure 2-2. *a)* APBS-produced electrostatic map of apo SERCA (*red* = −3.0 kT/e, *blue* = +3.0 kT/e). Brownian dynamics simulations were used to investigate cation binding to the L3 region of SERCA. *b)* Umbrella sampling simulations were used to model the cation moving from the protein/solvent/lipid boundary to approximately 10 Å deep within the TM region where Ca^{2+} binding-site II is located. *c)* Upon Ca^{2+} binding, a gradual motion of the N and A cytosolic domains was observed in MD simulations.

Results

Diffusion-limited binding of Ca^{2+} to the SERCA molecular surface

We hypothesized that Ca^{2+} binding proceeds as a two-step process: (1) diffusion of Ca^{2+} from the bulk to the interface between solvent and the binding channel; (2) subsequent diffusion within the binding channel to the site II binding site. To investigate the first step, we used Browndye to estimate the Ca^{2+} association rate, k_{on}, to the Ca^{2+}-free (apo) E1 state. These results are reported in Table 1-1. We chose reaction coordinates based on association with D813 of L1 and E309 of L3, as these residues border the postulated Ca^{2+} entryways or "vestibules." E309 is of special interest, as it both borders site II and the vestibule just outside site II along the L3 pathway. We did not observe any association events near L1, which we believe was due to the small spacing between the lipid and cytosolic domain comprising L1, as well as the presence of a positively charged residue nearby (K329). For the L3 site, however, we found significant accumulation near the L3 site that yielded a predicted Ca^{2+} association rate, k_{on}, of $3.4 \pm 0.04 \times 10^9$ $M^{-1}s^{-1}$ at a physiological ionic strength of 0.15 M (see Supporting Information, reference [18]). To examine the role of favorable electrostatic interactions between Ca^{2+} and the negatively charged residues of the L3 vestibule, we computed k_{on} with ionic strengths ranging from 0.05–2.00 M. First, we found that k_{on} decreases with increasing ionic strength (7.9×10^9 down to 1.41×10^9) as is expected for electrostatically-driven, diffusion-limited reactions. Second, we found that k_{on} at physiological ionic strength was nearly two-orders of magnitude greater (0.06×10^9 $M^{-1}s^{-1}$) than at high ionic strength (200 M), where electrostatic interactions are substantially shielded, using adaptive Poisson Boltzmann Solver (APBS).

Post-encounter incorporation of Ca^{2+} into the binding site

Considerable evidence suggests that Ca^{2+} binds SERCA in a cooperative manner [19]. One prominent model for sequential calcium binding implicates the rearrangement of D800, which links site I and site II, to enhance the affinity of site II for Ca^{2+} following binding at site I [1]. Here, we complement studies, in which the binding of Ca^{2+} to site I was explored, to examine the role of residues lining the L3 binding pathway in facilitating the incorporation of bulk Ca^{2+} into site II. To this end, we estimated the pathway from bulk solvent toward D800 of the binding site using POcket Volume MEasurer (POVME) (Fig. 2-3), as D800 is the primary residue bridging sites I and II that coordinates both Ca^{2+} ions. POVME approximates the shape of a binding domain by placing spheres around a user-defined region and culling those that clash with the protein [20]; as such, it can identify potential pathways bridging the protein exterior and binding domain. We considered the free space around D800 and with POVME, we identified a region that connects site II with the protein exterior corresponding to the L3 binding pathway suggested by Huang *et al*. and others [8,13,14]. Based on this analysis, it appears that the L3 vestibule is relatively open, but as one approaches E309, the solvent-accessible volume constricts to a very narrow (diameter of approximately 2 Å) and nearly linear pathway leading to site II. For the L1 case, we were unable to find a pathway that led to incorporation of the ion, as the region about Y763 bridging the L1 vestibule and site I appears to be too tightly packed, in contrast to findings from Huang *et al* [8]. One possible explanation for the discrepancy is that Huang's simulation realized an opening of this region that permitted solvent exchange between L1 and calcium binding site I.

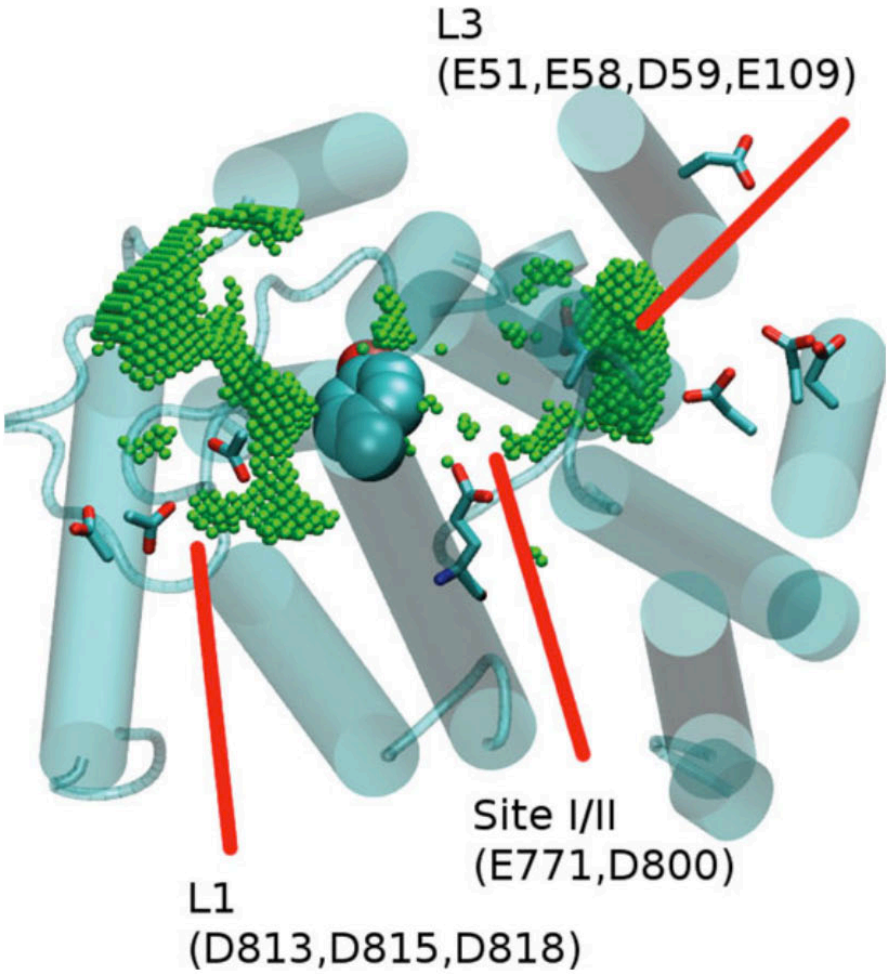

Figure 2-3. Top view of SERCA trans-membrane domain with L1 and L3 binding pathways and sites I and II Ca^{2+} coordination sites. Tyr 763 is represented with space-filling spheres. Green spheres were generated via POVME.

The accumulation of Ca^{2+} near the polar residues of L3 from Brownian dynamics (BD) simulations suggests the involvement of these residues in providing access to the TM binding domain. We examined conformations of the L3 residues E51, E55, D59, and E309 and found that only E309 assumes distinctly different distributions in the apo and holo states (Supporting Information, reference [18]). In the apo form, E309 peaks at approximately 180 degrees, corresponding to a conformation pointing toward the bulk solvent. In this conformation, E309 is in nearly continuous contact with the protonated E58 (see Supporting Information, [18]) and provides favorable electrostatic interactions with solvated cations. In the holo form, E309 shifts to −70 degrees (toward the binding site), where it forms a known coordination interaction with Ca^{2+} in site II. In contrast, we found that other charged residues, namely E51, E55, and D59, tend to freely rotate in both the apo and holo states without any clear conformational preference and are thus unlikely to play an active role in Ca^{2+} assimilation.

To investigate the ease of diffusion into site II along the approximately 12 Å-long L3 pathway, we estimate the Potential of Mean Force (PMF) along a reaction path leading from the bulk to the site II region. The trajectory, $\psi(x)$, consists of a linear path determined from POVME beginning at D800 ($\psi(x)$ = 2 Å) and ending in the bulk ($\psi(x)$ = 26 Å). The PMF was determined from umbrella sampling using 0.5 Å window sizes; values are reported relative to the minimum potential value at a favorable D800/Ca^{2+}coordination distance ($\psi(x) \approx 4$ Å). Far from the binding site, the PMF was nearly constant at 2.0 to 2.5 kcal/mol, but decreased by almost 1.5 kcal/mol as $\psi(x)$ approached a 7 Å separation from D800. At $\psi \approx 6$ Å we note a small barrier (≈ 0.5 kcal/mol) that we attribute to the formation of a bidentate interaction between Ca^{2+} and the E309 carbonyl side chain. In this configuration, we note the loss of one water molecule in the Ca^{2+} hydration shell, as illustrated in the Supporting Information movie. As $\psi(x)$ decreased from 6 Å, E309 rapidly flipped between the binding site and solvent-exposed conformations. The binding site-facing orientation of E309 toward D800 promoted binding of

Ca^{2+} via mono-dentate and bidentate interactions, respectively and thus forming the bound state, shown in Fig. 2-4b:

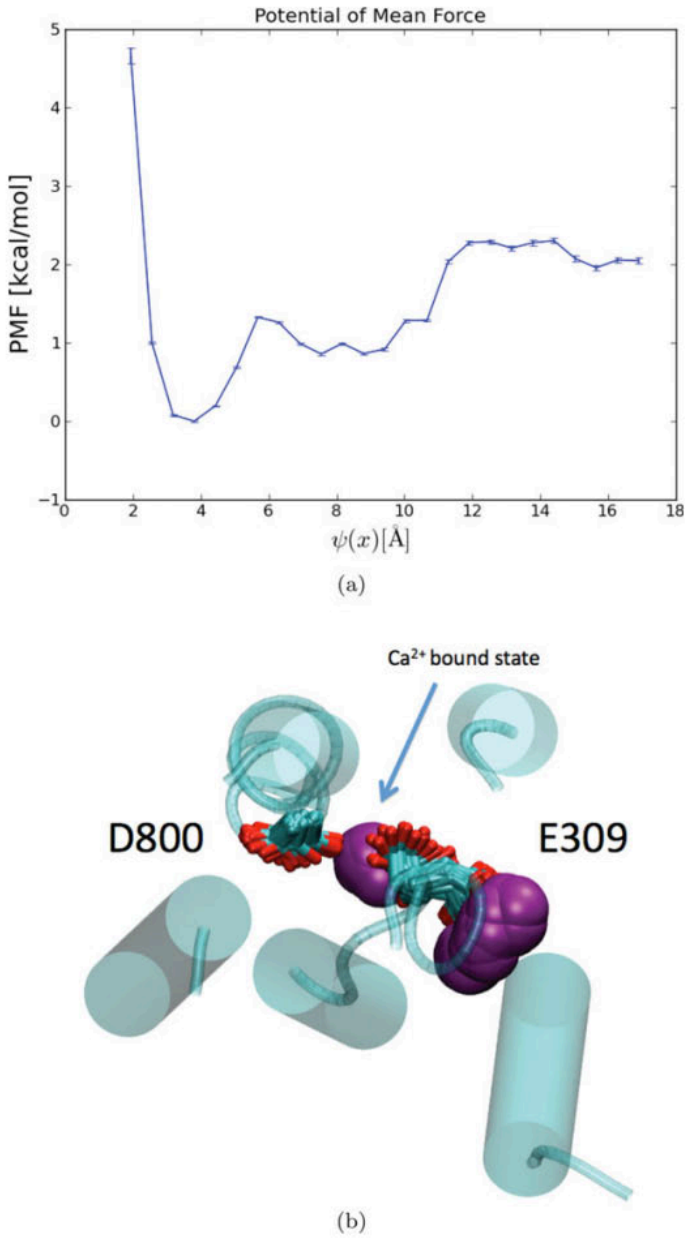

Figure 2-4. *a)* Potential of mean force corresponding to translation of Ca^{2+} from bulk ($\psi(x)$ = 18 Å) to the bound conformation with D800 ($\psi(x)$ = 2 Å). *b)* Figure showing gating of E309 with Ca^{2+} in *purple* space-filling spheres.

Based on our findings that E309 appears to switch conformations as Ca^{2+} approaches site II, we sought to characterize its gating rate as a function of Ca^{2+} position. To this end, we identified two E309 conformational states based on our observations and the convention in (1) a closed state oriented toward the binding site with a C_α/C_β angle of −70 degrees, which is typical of the holo enzyme and (2) an open state, typical of the apo configuration, with a C_α/C_β angle of 180 degrees, that points the carboxylic acid toward the L3 vestibule [21]. In Figure 2-5, we assign 1 (blue) when E309 assumes the open state, and 0 when closed. We find that when Ca^{2+} is far from the binding site (measured by Ca^{2+}/D800 distance in red), E309 was predominantly open (open probability, p_0, of nearly 80%), while exchanges between the open and closed states were very fast (nearly on the order of 1 ns). These data imply that there is a small energetic barrier to rotation between the two states. As Ca^{2+} approaches D800, the distribution rapidly changes and nearly entirely favors the closed state, especially after Ca^{2+} associates with E309 at t = 38 ns.

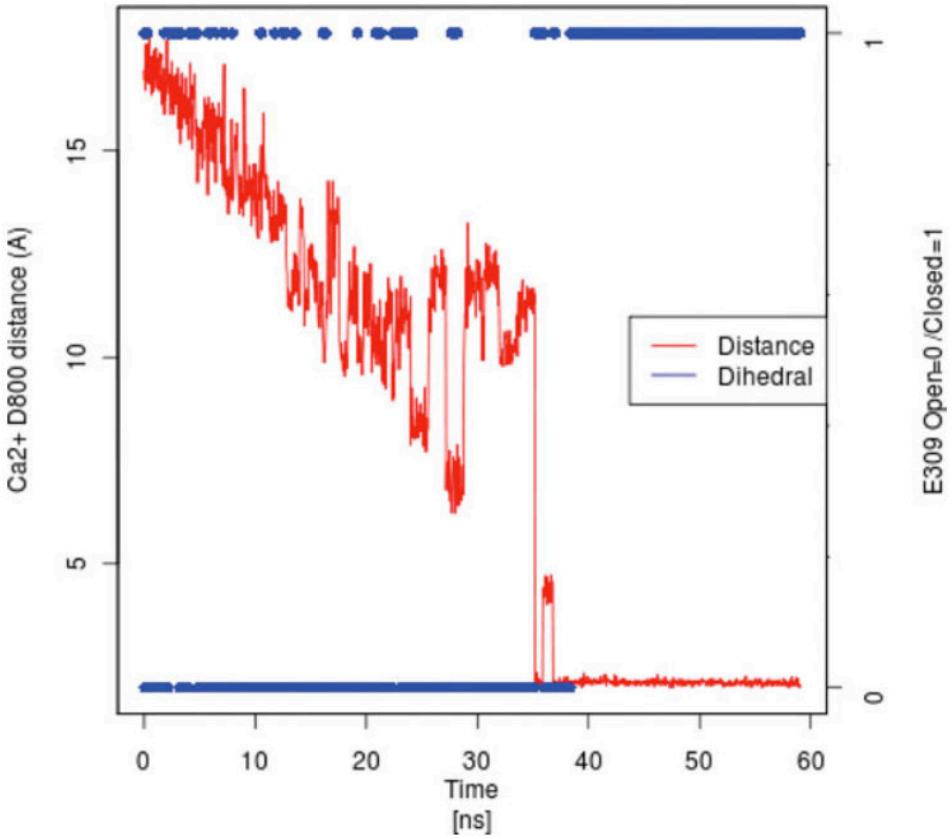

Figure 2-5. Plot of distance between Ca^{2+} and D800 of the bound configuration *(red)* versus E309 open/closed state. E309 is considered open when its C_α /C_β angle is approximately -50 degrees.

Structure and dynamics of E1 and E1(Ca)

Collective motions

To investigate the extent to which Ca^{2+} binding promotes conformational changes leading to E1P, we examined SERCA conformational motions linking the E1(Ca) and E1P states via MD. Principal Component Analysis (PCA) based on all available crystal structures separated 96% of structural variation into three principle modes, of which Principal Component 1 (PC1) and Principal Component 2 (PC2) captured 86% of the variance (Supporting Information, Figure S4, [18]). The crystal structures were partitioned into four tightly clustered, well-separated states; each cluster exclusively contained structures belonging to a specific catalytic state (E1, E1P, E2, and E2P). The first principal component (PC) primarily describes the transition between the E2 and E1(Ca) catalytic states (Fig. 2-6). The primary conformational motions involve an approximately 110 degree rotation of the cytosolic A domain in E2 structure parallel to the plane of the membrane and concurrent tilting of the cytosolic N domain away from the central TM bundle. PC1 also includes the straightening of helix M1. Helix M1 is bent along the plane of the bilayer in E2 but straightens to be nearly perpendicular to the plane of the bilayer in the E1(Ca) structure. Bundle motions were comparatively smaller, with the most obvious movement restricted to M5 progression toward M6. The second principal component (PC2) describes the transition between the E1(Ca) state and the E1P catalytic state, whereby the cytosolic domains A and N undergo a closing motion. This component corresponds to the A domain rotating perpendicular to the plane of the membrane with movement of the N domain toward the TM bundle. Together, these principal components correspond to large-scale collective motions that readily partition crystallographic SERCA data into catalytically-relevant states and comprise a relevant basis for characterizing our MD simulations.

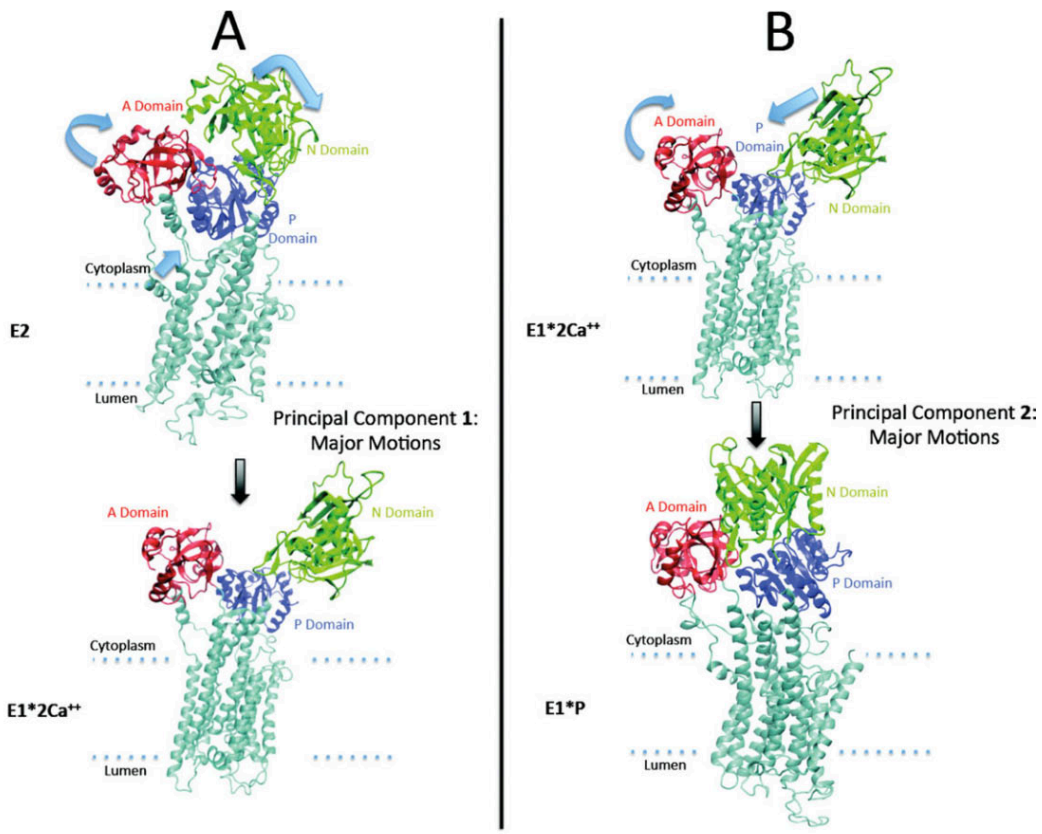

Figure 2-6. *a)* PC1 linking E2 and E1 states. *b)* PC2 linking E1 and E1P structures.

We performed four CMD simulations (run1: 2 × 75 ns and run2: 2 × 45 ns) and two AMD simulations (AMD: 2 × 225 ns) of the apo and holo states to investigate dynamic consequences of Ca^{2+} binding. As the closing motion identified by PC2 is a known requirement for E1P formation upon Ca^{2+} binding, we projected our molecular dynamics simulation data along this component (and PC1) to determine the extent to which we sample the E1→E1P transition (Fig. 2-7). We found that for two of the three independent apo cases, the trajectories progressed along the negative PC2 direction away from the E1P state, and to some extent along the negative PC1 direction toward the E2 state. In contrast, the holo cases consistently approached the E1P state along PC2 and away from the E1(Ca) crystal structures.

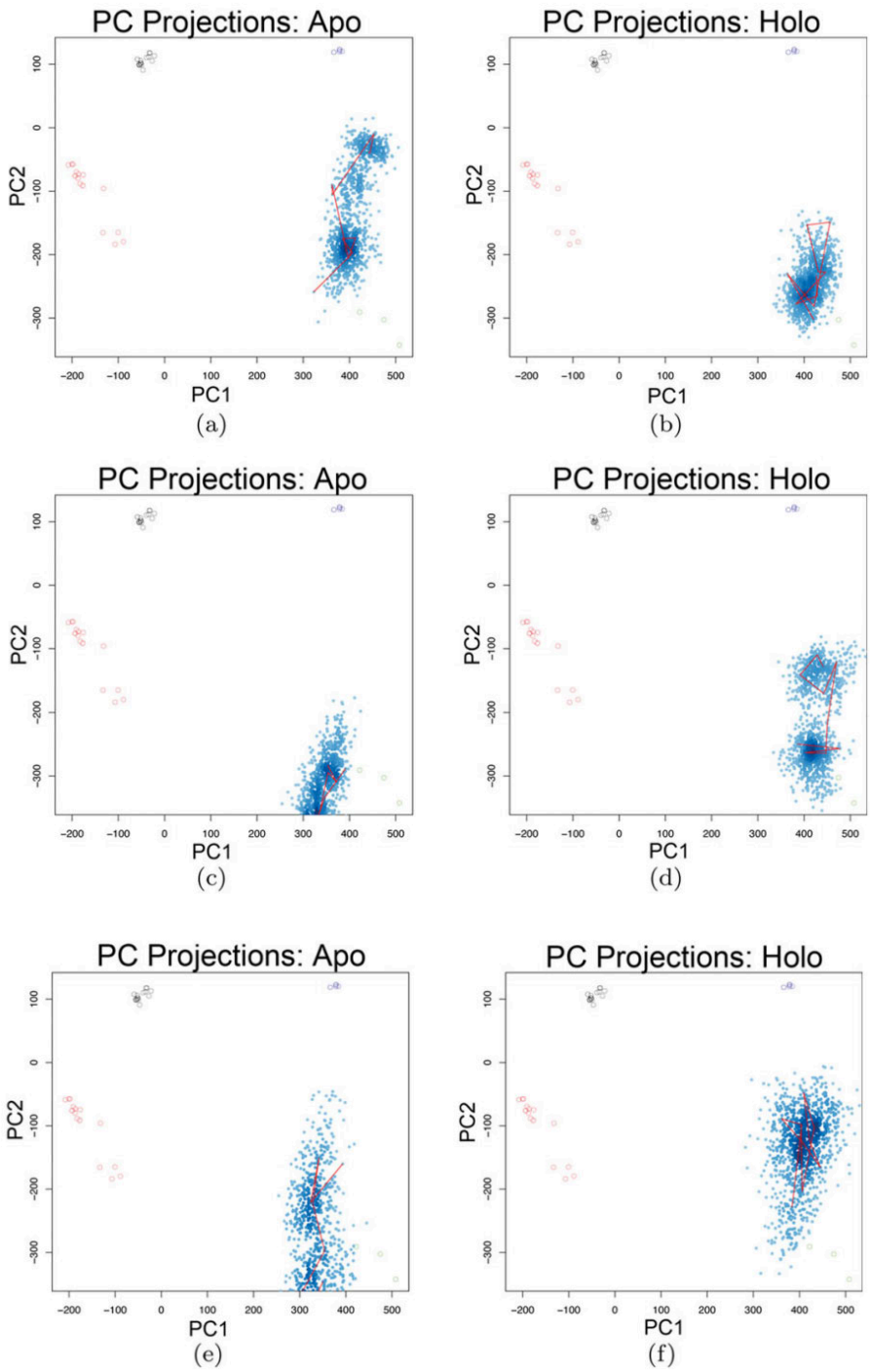

Figure 2-7. PCA projections of 75 ns conventional MD run 1 (top), 45 ns conventional MD (middle), and 225 ns AMD (bottom) simulations of *(a,c)* apo and *(b,d)* holo states. PC2 (y axis) and PC1 (x axis) separate crystallographic data into distinct regions: E1(*green*), E1P (*blue*), E2P (*black*) and E2 (*red*).

To gain insight into the domain motions underlying the E1→E1P transition, we examined the root mean squared deviations (RMSD) corresponding to the A, N, and P cytosolic domains, as well as the TM bundle from the conventional and accelerated MD simulations (Fig. 2-8). We consistently found that the N domain is the most mobile region of the protein with RMSDs in excess of 20 Å for some cases, while A is similarly mobile with ranges from 5–10 Å. The P domain, however, was found to be more mobile in the apo cases (run2 and amd have RMSDs around 5 Å), while all holo cases report substantially lower RMSDs (<3 Å with minor excursions). We also discovered that for the apo case in which the P domain moved comparatively little (run 1), considerable progress was made along PC2 toward E1P, in contrast to the other apo cases (run2 and aMD) (Supporting Information, Table 3).

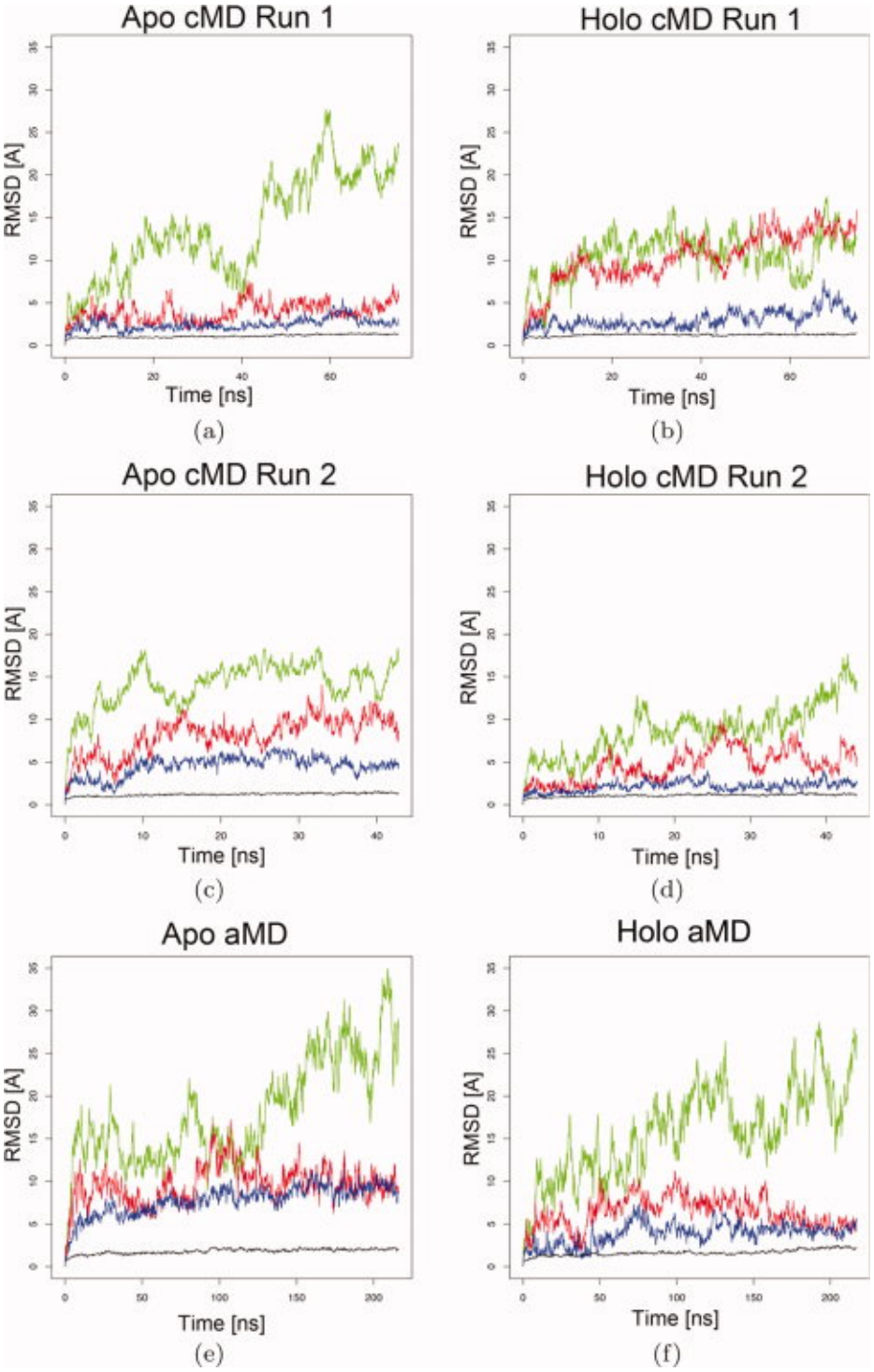

Figure 2-8. Overall RMSD for domains A,N, and P (*a,c,e*) apo and (*b,d,f*) holo configurations. Rows correspond to CMD run 1 (*a,b*), CMD run 2 (*c,d*) and AMD run (*e,f*). Plots are colored according to cytosolic domains A (*red*), N (*green*), P (*blue*), and bundle helices (*purple*).

Residue dynamics

To investigate whether these large-scale conformational motions are accompanied by localized changes in the dynamics of individual domains, we examined the root mean squared fluctuations (RMSF) in the apo and holo states (Fig. 2-9). Independent of Ca^{2+}, we report large RMSF values indicating that the cytosolic domains A (red), N (green), and P (blue), as well as the cytosol-exposed TM bundle loops (L12, L34, L67 and L89) were relatively mobile compared to the rigid TM bundle (purple). Among the TM loops, the L67, and L89 (black) bordering the hypothesized L1 binding pathway, were comparatively more rigid than the L12/L34 loops along the L3 binding pathway. These findings are in agreement with Costa *et al.* [14], although in contrast, Huang *et al.* [8] found that L67 was quite mobile; the discrepancy is very likely due to the difference in simulation lengths and sensitivity to initial conditions. Upon binding Ca^{2+}, we observe consistent increases in RMSF for A domain (red, +15–35% change in RMSF over amino acids in domain) and bundle loop L34 (+10–50%) across all holo simulations (See Supporting Information, Fig. S5 in [18]). While large changes were also noted for the N domain (green, >10%) and the loops linking the bundle and cytosolic domains (gray, >5–15%), both increases and decreases were observed without any clear correspondence to the apo versus holo states. Thus, while little change in fluctuations was noted within the bundle where Ca^{2+} binds, it is apparent that binding allosterically impacts the dynamics of distant regions of the protein.

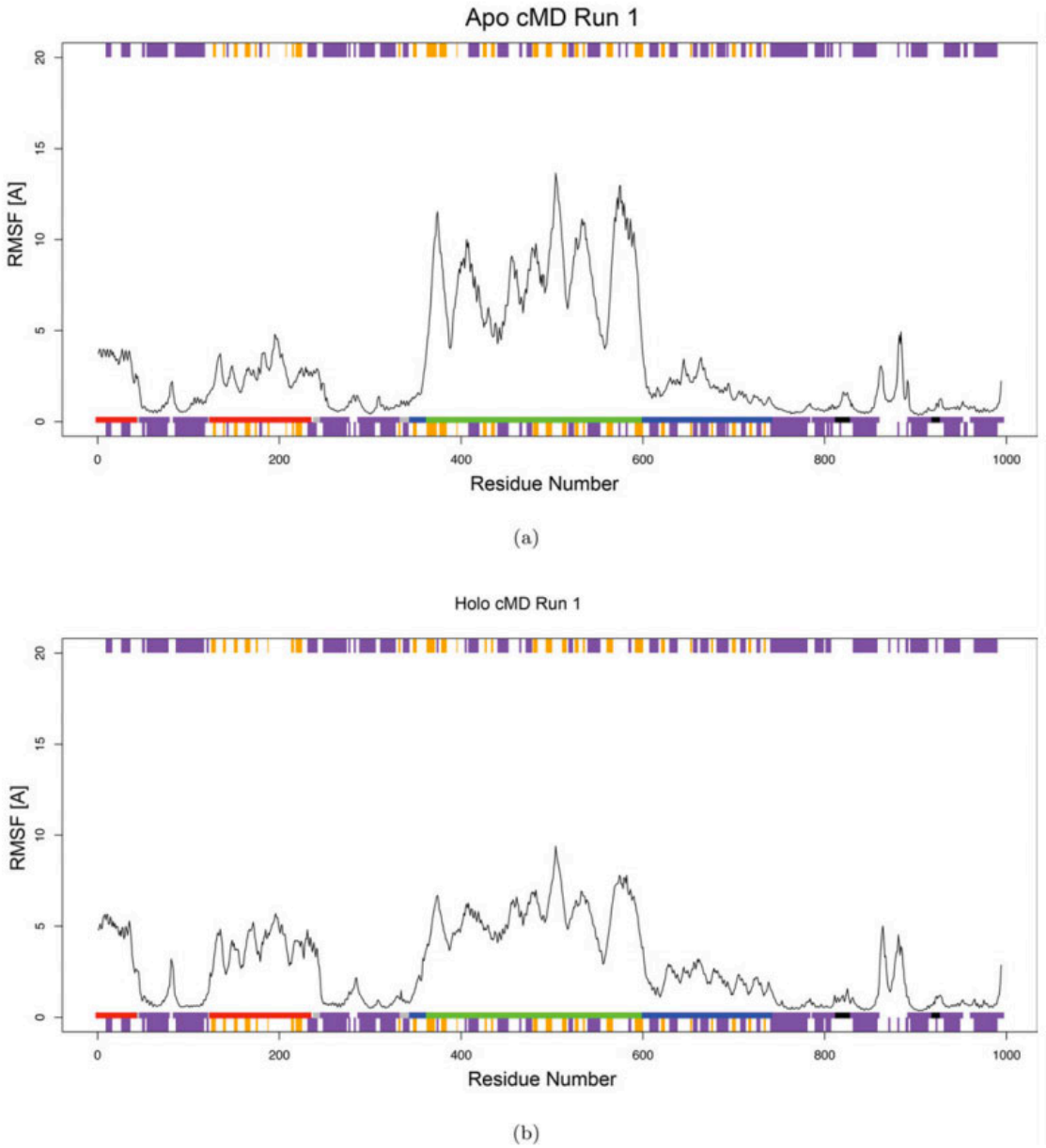

Figure 2-9. RMSF distribution for (*a*) apo and (*b*) holo based on CMD run1 simulation. Residues are colored according to cytosolic domains A (*red*), N (*green*), P (*blue*), cytosolic loops (*gray/yellow*), bundle helices (*purple*), and bundle loops (*black*).

Discussion

Diffusion-limited Ca^{2+} binding

Brownian dynamics studies reveal that Ca^{2+} binding is diffusion-limited, guided by electrostatic interactions and impacted by E309 gating. Other studies [17,19] reported apparent equilibrium constants ranging from 0.32 to 2.3 μ*M* for several SERCA isoforms; assuming k_{off} is roughly 0.1 s^{-1} [22] these equilibrium constants suggest k_{on} could range from 1.2×10^6 and 5×10^8 $M^{-1}s^{-1}$. While our predictions of 3.13×10^9 $M^{-1}s^{-1}$ are within the diffusion-limited regime, they are between one and three orders of magnitude faster than experimental estimates. Nevertheless, the very fast association rate suggests the importance of strong electrostatic interactions between SERCA and Ca^{2+}, which is a common mechanism for achieving large diffusion-limited rates in a variety of enzyme reactions [23].

The contribution of favorable electrostatic interactions is evidenced by the accumulation of BD Ca^{2+} trajectories near the negatively-charged region at L3 (particularly at E51, E55, E58, D59, E109 in agreement with [10,13]. Furthermore, we showed that k_{on} at physiologically-relevant ionic strength is nearly two-orders of magnitude faster than when a purely hypothetical ionic strength is used to nullify the electrostatic interactions. We considered the possibility that the electrostatic driving force might vary due to the highly mobile charged amino acids or the occasional lipid head-group diffusing toward the binding pathway, and these variations may partially explain the discrepancy between our predictions and experimental estimates of k_{on}. However, we obtained very similar Brownian dynamics association rates using a multitude of SERCA structures, which suggests that the long-ranged electrostatic driving force is relatively insensitive to the SERCA conformational state or lipid configuration.

Therefore, we believe the disparity between our predicted and experimentally observed k_{on} estimates may in fact be due to post-encounter effects occurring after the initial

association of Ca^{2+} with the SERCA exterior. One potential post-encounter effect, gated access to site II via E309 suggested by experimental [10,13] and computational studies [16], may partially account for the difference between theoretical and experimental estimates of k_{on}. According to [24], the impact of a gated binding site on the observed association rate, $k_{on,obs}$, can be estimated by comparison of the gating rate, ω, to the characteristic diffusion time of the substrate, τd, to escape the binding site. If $\omega \gg \tau d^{-1}$, a fast limit is obtained in which $k_{on,obs} = k_{on}$; for $\omega \ll \tau d^{-1}$ a slow limit is obtained, in which the association rate is weighted by the probability that the gate assumes the holo configuration, p_h ($k_{on,obs} = p_h\, k_{on}$). Assuming for simplicity a diffusion constant of $D = 7.7$ cm^2/s for a bare Ca^{2+} ion and an escape distance one Debye length $x \approx 7$ Å (1×10^{-7} cm), we might anticipate $\tau d \approx 10$ ns using $x^2 = 6D\tau d$, which places our system within an order of magnitude of the slow-gating regime. Combining the estimated holo probability ($ph = 1 - p_o \approx 20\%$) and the slight PMF barrier (0.5 kcal/mol) could reduce our k_{on} by an order of magnitude and within experimental estimates. Numerical estimation of the local diffusion constant would be necessary to more adequately describe the binding kinetics and is the subject of further inquiry. Additional considerations, such as including polarization effects due to Ca^{2+}, and assessment of the entropic change during the dehydration of Ca^{2+}, could also significantly impact estimations of k_{on}.

Binding pathways

M6/M7 (L1) [12,25] and M1 (L3) [10] have been proposed as potential pathways in early MD studies [7,14]. However, recently Musgaard *et al*. [13] provide convincing electrostatic and molecular dynamics evidence that only L3 supports binding. Our studies confirm their findings, and also demonstrate that ligand-dependent E309 gating is further involved in Ca^{2+} entry. Based on BD results, the accumulation of Ca^{2+} near L3 and not L1 suggests the possibility that only the former supports cation association, in agreement with

findings from Musgaard *et al* [13]. To further rule out the possibility of Ca^{2+} entry via L1, we examined solvent exchange into L3 and L1 from our MD studies as a probe for Ca^{2+} entry and found the water exchanges more freely at L3 than L1 (data not shown). We attribute this to two factors: (1) there is a significant deformation of the lipid bilayer near L3 found in this study and others [26,27] that provides a larger interfacial area for solvent entry and (2) the relatively rigid L67/L89 regions evidenced by RMSF constitutes a restrictive gateway to solvent exchange. These findings, together with our POVME calculations showing no clear pathway between L1 and site I, challenge the idea of L1 serving as a Ca^{2+} binding route in absence of substantial rearrangement. Nevertheless, it is possible that ions with smaller effective radii or coordination shells could diffuse into or out of L67/L89, such as the proton release from E309/E771 preceding the E1→E1P transition [13].

For Ca^{2+} binding at L3, the ion must diffuse from the solvent-exposed vestibule toward the buried Ca^{2+} binding site. Our estimates of the PMF along this pathway (from just prior to association with E309) suggest favorable electrostatic interactions between Ca^{2+} and the negatively-charged residues lining the L3 region facilitate Ca^{2+} entry. Impeding binding, however, is a barrier between the L3 vestibule and site II where E309/Ca^{2+} interactions predominate. The barrier characterized in this study involves both a rotation of the E309 χ_1 angle and a reduction in the water coordination number of Ca^{2+}. In our simulations, the energetic cost of dehydrating Ca^{2+} in order to traverse the narrow binding region underneath E309 appears to be offset by the bidentate coordination of Ca^{2+} with the carboxylic acid. These findings could explain why E309Q [21] and E309D [22] increase Ca^{2+} dissociation, as E309Q could disrupt Ca^{2+} coordination and E309D could widen the pore leading out of site II. Thus, these factors together could constitute a filter selective for Ca^{2+} relative to K^+ and Mg^{2+}. Investigating the interplay between E309 gating rates and PMFs associated with K^+, Ca^{2+}, and Mg^{2+} entry may provide further insight into this phenomenon.

Site I residues serve an important role for stabilizing Ca^{2+} within site II, particularly when already occupied by the first bound Ca^{2+}. In particular, site I bound Ca^{2+} orients the D800 backbone carbonyl oxygen toward the site II binding site, thereby presenting a necessary coordination oxygen for site II Ca^{2+} binding. While we expect the potential of mean force near $\psi = 0$ Å to vary depending on whether site I is occupied by Ca^{2+}, we do not expect the electrostatic component to the PMF to change considerably beyond $\psi = 2$ Å, therefore, our estimates of the E309 gating rate and diffusional encounter of Ca^{2+} should be comparable. We base this speculation on the abundance and relative mobility of charged amino acids in site I, which would likely screen the strong positive charge of a bound Ca^{2+}. We believe this speculation is in line with findings from Musgaard et al [13], who showed that cation accumulation in the binding region is found in both their apo and bound states, therefore, evidencing a similar electrostatic field near the binding region. Nevertheless, local variations, such as differences in the relative order of M4 between the E2 and E1(Ca) states [14], could impose additional steric barriers to Ca^{2+} diffusion.

Protein dynamics

It is apparent from crystallographic data that Ca^{2+} binding to the apo E1 state induces conformational changes that promote formation of the ATP-bound E1P state. Our data underestimate this conformational change, yet nevertheless demonstrate that binding of Ca^{2+} alters loop and cytosolic domain dynamics. While we found that the motions of the cytosolic domains varied considerably between simulations, we found trends that could explain the effects of Ca^{2+} binding. One particularly interesting trend is the correlation between motion of the P domain and progression toward E2, whereas motion along PC2 toward E1P seems to occur spontaneously when the P-domain is immobile. As the P domain is consistently immobile in the Ca^{2+} state, and mobile for two of the three apo simulations, it is possible that Ca^{2+} binding

shifts the equilibrium between P-mobile and P-fixed states and thus increases the likelihood of progressing toward the E1P state relative to the apo state. Interestingly, we also observed that the most probable conformation indicated by principal component (PC) space was somewhat distinct from the crystal structures suggesting that the stable A/N distance is smaller than the crystal structure, as concluded from fluorescence resonance energy transfer (FRET) experiments [2]. Hence, the structural data obtained from x-ray crystallography may benefit from inquiry into the dynamics underlying SERCA function that is afforded by MD simulation and dynamical measurements such as FRET and nuclear magnetic resonance (NMR).

This MD study and that of Espinoza-Fonseca *et al.* [17] also consistently found that Ca^{2+} binding alters the dynamics of the cytosolic domains in the absence of major bundle rearrangement. As such, it is possible that they contribute an entropic driving force toward conversion to the E1P state upon ATP hydrolysis, which would help explain its temperature-dependence [9]. An additional contribution of enhanced motion of the cytosolic domains toward E1P via immobilization of the P domain is the promotion of ATP binding by decreasing the distance between domain A and D351 of domain P, thus enabling the latter's phosphorylation [17]. Upon ATP binding, sufficient free energy would be provided to promote substantial bundle rearrangement that ultimately stabilizes the E1P structure. This stepwise-interpretation would explain why there is an estimated millisecond timescale for the E1→E1P transition observed experimentally [28], despite possible sub-microsecond A/N closing dynamics observed in MD studies [17].

As a whole, we did not observe significant rearrangements of bundle helices upon Ca^{2+} binding. We anticipated that in absence of Ca^{2+}, the disordered region of M4 near E309 reported in the E1 state would reform the alpha helix found in E2 upon binding as was assumed in the MD study from [14]. We instead found that M4 remained disordered, which we propose facilitates the transfer of Ca^{2+} from the binding vestibule into site II via E309. It is possible that

protonation of E309 and E771, as expected in the E2 state [9], may be required to reestablish the helical region in the disordered region about E309.

Despite little change in the structure of M4, we found the magnitude of fluctuations (RMSF) for the L34 loop was increased in the holo state. Based on the enhanced cytosolic domain and loop mobility in absence of bundle rearrangement, we postulate that one effect of Ca^{2+} binding is that the TM bundle is locked in place, thereby promoting a redistribution of vibrational motion to the cytosolic domains. Shifting of fluctuations upon substrate binding has been observed in other systems by NMR [29] and simulation [30], and may constitute a common mechanism of allosteric signaling. As M4 has been postulated as a transducer of the signal between the Ca^{2+} binding site and phosphorylation regions of the P-domain [1,31], it is possible that enhanced fluctuations of L34 may allosterically contribute to dynamics along PC1 and PC2 by modulating P domain mobility. In contrast, L67 and L89 were found to be quite rigid, which may help lock the TM bundle with the P domain and thereby promote progression toward E1P. Disrupting this lock might then be expected to reduce ATPase turnover, as was observed by [12] for L67 at the D813, D815, and D818 positions. Overall, however, changes in SERCA conformational dynamics due to Ca^{2+} are anticipated to be small relative to those induced by ATP binding [32].

Limitations

In this study, we chose an apo state based on removal of Ca^{2+} from the E1(Ca) structure, in line with [17,27]. Experimental data suggest that at least one additional choice of apo state may be possible [12,33]. In [33], Trp quenching was measured during sequential binding of Ca^{2+}, which suggested a conformational difference between the E1(Ca) and E1 free states. Specifically, the data suggest that binding of Ca^{2+} to site I does not change the fluorescence signal, whereas site II binding leads to a drop indicative of a conformational change that might

not be apparent in our model choice. However, we believe it is reasonable to anticipate that fluorescence does not give a strong indication of the amplitude of such conformational changes [2]. Furthermore, it is not clear from the experiment, which TM Trp were impacted by the conformational change, and whether these changes are evidence of differences in the L3 binding vestibule considered in our study. Given that the nearest Trp to site II is 12 angstroms from the L3 vestibule, and the other eleven Trp are toward the periphery of the bundle, it is equally possible that quenching indicates distant conformational changes not pertinent to the Ca^{2+} binding domains. In our opinion, there is not sufficient evidence to rule out our choice of model.

One possibility to reconcile the apparent contradiction between our model and the Lenoir experiment is that several apo states are in thermodynamic equilibrium, and the population of these states is dependent on pH and Mg^{2+}, which are important factors in SERCA turnover. Binding of Ca^{2+} then, may shift this population to favor the E1(Ca) state, similar to what had been endorsed by Winters *et al.* [2] for the cytosolic SERCA domains. Thus, our starting point with the E1(Ca) state could represent one of the possible states for Ca^{2+} binding.

In fact, we believe that our model may be the most representative conformational under physiological conditions, based on findings from Inesi *et al*. [9] In this study, it is suggested that deprotonation of E309 and E776 favors conversion to the E1 state, even in absence of Ca^{2+} binding, in contrast to the findings of Lenoir et al. [33]. One difference between the preparations is that the Lenoir experiment was conducted in Mg^{2+} free conditions, whereas Inesi appeared to use 3 mM Mg^{2+}, which is a more representative concentration in physiological systems. Therefore, the findings of [33] might not be universal and thus it is our opinion that a change in SERCA protonation state, as done by us and argued by others [17], should be adequate to represent the apo structure.

It is further possible that the apo state might bear closer resemblance to the E2 structure as opposed to the E1(Ca). We note that in [13], the E2 (3NAL) structure was used as a starting point for apo simulations to explore cation binding pathways toward (but not into) sites I and II. Here, the authors state that the E2 structure corresponds to the conformation just prior to Ca^{2+} binding in which the binding sites are occluded. Comparison of the E2 and E1(Ca) structures suggest that the M4 helix unwinds near the Ca^{2+} binding domain and M1 straightens. As the E2 structure does not bind cytosolic calcium (see Figure 4 in [13]), whereas the E1(Ca) does, we believe it is plausible that M4 and M1 require rearrangement before Ca^{2+} may be bound. Indeed our PC analysis indicates that the majority of conformational motion linking the E2 and E1(Ca) state owes to the cytosolic domains and these helices, though preliminary simulations with the E2 structure did not indicate significant motion of these components. As we do not anticipate that the E1 apo state would be drastically different from all other known SERCA crystallographic structures, we believe it is likely that the conformational changes due to sequential binding of Ca^{2+} to prevent open exchange of site I Ca^{2+} with solvent may be subtle and are thus not likely to influence our modeling of Ca^{2+} association and protein dynamics to a large degree.

Summary and conclusions

Our study explores Ca^{2+} binding as a three stage binding model consisting of (1) rapid binding of ion to the SERCA exterior, (2) fast entrance of the ion into the binding site via L3 and 3) slow time-scale reorganization of binding site that initializes allosteric signaling to the cytosolic domains (Fig. 2-2). Diffusion-limited, electrostatically-driven binding of Ca^{2+} to the SERCA surface is supported by kinetic measurements [28,31] and our simulated k_{on} experiments. The role of negatively charged amino acids in L3 and especially

E309 in escorting surface-bound Ca^{2+} to the binding site is supported by mutagenesis studies, [21] as well as our PMF simulations. The development of an allosteric signal between the TM region and the cytosolic domains upon Ca^{2+} binding is supported by FRET studies [2,34] of M4 and M6, as well as our MD data and in particular, differences in RMSF between apo and holo states.

We believe these analyses complement those of Espinoza *et al.* and provide additional insight into the basis of conformational motion due to the presence of Ca^{2+} in the calcium binding sites. Namely, we found that that free movement of the P domain tends to lead to propagation toward the E2 state, whereas reduced movement of P domain leads to the ATP bound state. Binding of Ca^{2+} was consistently found to reduce P-domain movement. Moreover, by performing several calculations, we show that dynamics of the receptor change significantly, and suggest that a single trajectory may be one of many possible pathways.

This model may constitute a general allosteric mechanism governing the P-type ATPase family, of which SERCA is a representative member. Furthermore, our model opens doors for strategies for controlling SERCA activity including mutation of uncharged surface residues to acidic residues to further increase k_{on} and modification of bundle and cytosolic residues to modulate allosteric signaling.

Methods

Molecular Dynamics

The Ca^{2+}-bound (holo E1(Ca) SERCA state, PDB id 1SU4) was obtained from the RCSB Protein Databank; the Ca^{2+}-free state (holo) was obtained by removal of the two coordinated Ca^{2+} ions. ProPka [35] was used to assign protonation states to the ionizable residues. Following reference [16], E58 and E908 were protonated for the holo state; E771 and

D800 were protonated in the apo state in accordance with reference [36]. Based on references [9] and [37], E309 is deprotonated to simulate the E1(Ca) state. Thus, we elected to remove the Ca^{2+} ions from the holo enzyme and allow sufficient reorganization of the protein using molecular dynamics. Indeed, our simulations reveal conformational changes near the calcium binding domains upon removal of Ca^{2+}, predominantly involving E309. The soundness of this approach was demonstrated in [17], in which the Ca^{2+}-dependent, catalytically-relevant motions of the SERCA cytosolic domains were examined in the presence and absence of Ca^{2+}.

The psfgen package in visual molecular dynamics (VMD) [38] was used to apply patches for ionizable residues and also for disulfide bonds between C636-C675 and C876-C888. The structure was inserted into a 1-palmitoyl-2-oleoylphosphatidylcholine (POPC) lipid bilayer of dimension 140 × 140 angstroms with 483 POPC molecules using the VMD 1.9 Membrane Builder Tool. TIP3P solvent molecules were added to the space above and below the POPC lipid bilayer around the protein. 0.15M equivalents of K+ and Cl- were added to neutralize the system and resemble typical intracellular concentrations of the electrolyte. The CHARMM27 force field with NBFIX [39] was used for parameterization of all atoms. The system was partially equilibrated using NAMD 2.8b3 [40] with all atoms fixed except for the lipid tails that were allowed to melt at 310 K. Next, 1000 2 fs steps of additional equlibration were performed with only the protein fixed. The system was then equilibrated with no fixed atoms at constant pressure for 0.5 ns prior to production conventional (CMD) and accelerated (AMD) MD runs. Production CMD and AMD simulations were performed with an NVT ensemble using a 2 fs timestep and periodic boundary conditions; 12.0 Å cutoffs were used for non-bonded terms, and tolerance, interpolation order and grid spacing were set to 1×10^{-6}, 4, and 1.0 Å, respectively, for the Particle-Mesh Ewald algorithm [41]. AMD simulations utilized the dihedral-boost method [42] implemented in NAMD 2.8b3, with a threshold dihedral energy value of 35,100 kcal/mol and acceleration factor α = 1,820 kcal/mol. All other preparations follow from the

conventional MD simulations. For this study we refer to three sets of simulations: CMD run1 (2 × 75 ns for apo and holo configurations), CMD run 2 (2 × 45 ns) and AMD (2 × 225 ns).

Principal component analysis

Principal component analysis of all homologous SERCA pump structures (approximately 40 structures with ≥ 70% sequence identity) was performed using Bio3D [43]. Bio3D identified an invariant core, which refers to the set of atoms with the smallest variation across available crystal structures. This invariant core was predominantly comprised of P-domain residues (620–624, 636–642, 653, 654, 657–667, 669–671, 674–678, 683, 686–692, 696–699) and a small loop region spanning M4 and the N domain (347–352). All structures were aligned to the invariant core for subsequent PCA. For convenience, we have summarized the key SERCA domains and their constituent amino acids in Supporting Information Table 2.

POVME

POVME v1.1.0 [20] was used to determine the solvent accessible volume around the L1 and L3 vestibules. The pocket-encompassing region was computed using an initial set of spheres at 0.5 Å intervals within 30 Å of E309 of L3 and D813. Spheres in this region that intersected with the protein were culled by using a padding radius of 1.4 Å. Using VMD, we displayed the remaining spheres with VDW radii of 1.4 Å and identified connected sets of spheres bridging the protein exterior and E309/D813.

BrownDye

BrownDye [44] was used for Brownian dynamics simulations of Ca^{2+} binding to SERCA structures generated from MD. We selected ten structures to determine if the k_{on} rates were dependent on conformation. We included explicit lipids in these simulations from the MD-

equilibrated structures, as they prevented spurious diffusion of Ca^{2+} into the TM bundle where the lipid-bilayer would typically be found. PDB2PQR [45] using the CHARMM27 [39] force field for atomic charges and radii was used to generate APBS input. APBS v1.2.1 [46] was used to compute the electrostatic potential using the linearized Poisson-Boltzmann equation assuming an ionic strength of 150 mM. 500,000 simulation trajectories were used to determine k_{on} association rates according to the NAM algorithm [47]. BrownDye assumes a spherical reaction geometry for which k_{on} scales as $4 \pi D R$, where D is the diffusion constant and R is the radius of the reacting sphere. For a planar geometry with a reacting disk of radius R, k_{on} scales as $4 D R$ [24]. Therefore, we anticipate a factor of π error in the predicted k_{on} s.

Umbrella Sampling

A truncated version of the SERCA site II was created by selecting all contiguous residues within 10 Å of E309, including residues 47–60 (M1), 98–112 (M2), 300–315 (M4), 758–771 (M5), and 790–807 (M6). Our choice of truncation was based on the observation that these helices changed insignificantly over the course of our simulations. Hence, a truncated system for which the helices are constrained to their average position constitutes a suitable model for potential of mean force calculations, similar to the protocol described in reference [48]. While bilayer lipids border the exterior of the L3 vestibule, they do not appear to enter the L3 vestibule where the PMF calculations are performed; rather, their contribution is included in the BrownDye calculations. We defined our reaction coordinate in 0.5 Å intervals along L3 based on the connected set of spheres yielded by POVME; this linear trajectory led from the bound configuration (single ion) to an arbitrary region in the solvent (22 Å separation). For the bound configuration, we chose coordination with D800 in site II, since experimental studies [7] indicate that site I binding precedes site II, and D800 is the primary residue that bridges the site I and site II. For each window, the ion was constrained to the appropriate position using a force

constant of 10.0 kcal/mol, and then equilibrated for 2 ns. Statistics were collected for 6.0 ns per window following equilibration. PMF determination followed from application of the WHAM protocol (26 bins, 310K), including 50 Monte Carlo trials for bootstrap analysis of statistical error.

Trajectory Analysis

The Bio3D [43] package was used to analyze MD trajectories. MD trajectories were projected along the first and second PCs identified from the available crystal structures and hierarchically clustered according to the Mahalanobis distance in PC space. The top ten structures were selected for estimation of diffusion-limited Ca^{2+} binding rate.

Table 1-1. Predicted k_{on} Values at Various Ionic Strengths

Ionic strength [M]	0.05	0.15	0.20	0.25	2.00	Inf
k_{on} [x 10^9 M^{-1} S^{-1}]	7.9 ± 0.08	3.40 ± 0.04	3.51 ± 0.05	3.15 ± 0.05	1.41 ± 0.3	0.062 ± 0.5

Acknowledgements

The authors thank Jeff Wereszczynski, Yi Wang, and Peter Tieleman for interesting discussions and careful reading of the manuscript. The computations were in part performed on Kraken at the National Institute for Computational Sciences (http://www.nics.tennessee.edu/) and the DAVinCI cluster acquired with funds from NSF. This work used the Extreme Science and Engineering Discovery Environment (XSEDE), which is supported by the NSF.

Chapter 2 is a minimally modified reprint of the material as it appears in Kekenes-Huskey PM*, Metzger, VT*, Grant BJ, McCammon JA. Calcium Binding and Allosteric Signaling Mechanisms for Sarcoplasmic Reticulum Ca^{2+} ATPase (SERCA). Protein Sci.

Oct;21(10):1429-43. doi: 10.1002/pro.2129. (2012) *Metzger VT and Kekenes-Huskey PM contributed equally to this research. I served as a primary investigator and author of this publication.

Chapter 3: Electrostatic channeling in *P.falciparum* DHFR-TS: Brownian dynamics and continuum modeling

Abstract

We perform Brownian dynamics simulations and continuum modeling of the bifunctional *Plasmodium falciparum* dihydrofolate reductase−thymidylate synthase (*P.falciparum* DHFR-TS) with the objective of understanding the electrostatic channeling of dihydrofolate generated at the TS active site to the DHFR active site. The results of Brownian dynamics simulations and continuum models suggest that compared to *L. major* DHFR-TS, *P. falciparum* DHFR-TS has a lower but significant electrostatic-mediated channeling efficiency (~15% - 25%) at physiological pH (7.0) and ionic strength (150mM). We also find that removing the electric charges from key basic residues located between the DHFR and TS active sites significantly reduces the channeling efficiency of *P. falciparum* DHFR-TS. Although several protozoan DHFR-TS enzymes are known to have similar tertiary and quaternary structure, subtle differences in structure, active-site geometry, and charge distribution appear to influence both electrostatic-mediated and proximity-based substrate channeling.

Introduction

Many biochemical reactions in cells are sequential enzymatic reactions where the product of one enzyme serves as the substrate of a second enzyme [49,50]. Experimental evidence suggests that some of these consecutive enzyme-catalyzed reactions exploit substrate channeling in order to maximize the efficiency of the transport of product from the first active site to the second active site, at which the next enzyme-catalyzed reaction occurs [50]. More precisely, substrate channeling refers to the scenario where intermediate from one reaction site is transferred to a consecutive reactive site without complete mixing of the intermediate with the

bulk solvent [51]. This efficient transfer can be achieved through molecular tunnels, electrostatic channeling, or active sites in close proximity [51,52]. While a molecular tunnel relies on the geometric confinement of intermediates to prevent their diffusion into bulk solvent, electrostatic-mediated substrate channeling utilizes electrostatic interactions to create a virtual tunnel that confines the intermediate between the two reaction sites [52,53].

A well-known example of electrostatic channeling along a solvent-exposed surface is the bifunctional protozoan DHFR-TS enzyme from *L. major*. In this enzyme, the negatively charged (-2 net charge under physiological conditions) dihydrofolate intermediate synthesized at the thymidylate synthase (TS) active site subsequently reacts at the dihydrofolate reductase (DHFR) active site. Both kinetic experiments [54] and Brownian dynamics simulation studies [55] support the existence of electrostatic channeling of dihydrofolate between the two active sites of *L.major* DHFR-TS. The experimental evidence of substrate channeling is based on an observed decrease in the transient time compared to that expected in the system without channeling for the appearance of the final coupled enzyme product (in this case tetrahydrofolate) and an increased overall sensitivity of the net reaction rate to competitive inhibitors. Kinetic experiments on the bifunctional DHFR-TS enzyme from *L.major* DHFR-TS suggest that 80% or more of dihydrofolate molecules are channeled directly from the TS active site to the DHFR active site of this bifunctional enzyme [54]. Brownian dynamics simulations performed in the past on *L. major* DHFR-TS also showed high transfer efficiency of intermediate that is >95% at zero ionic strength and >50% transfer efficiency at physiological (150mM) ionic strength [55].

Although human DHFR and TS reactions are catalyzed by separate, monomeric enzymes, in some plants and protozoa, these two enzymes exist in a dimer structure with four active sites, including two TS active sites and two DHFR active sites [56,57], as in *L. major* and *P. falciparum* (Fig. 3-1A and Fig. 3-1B).

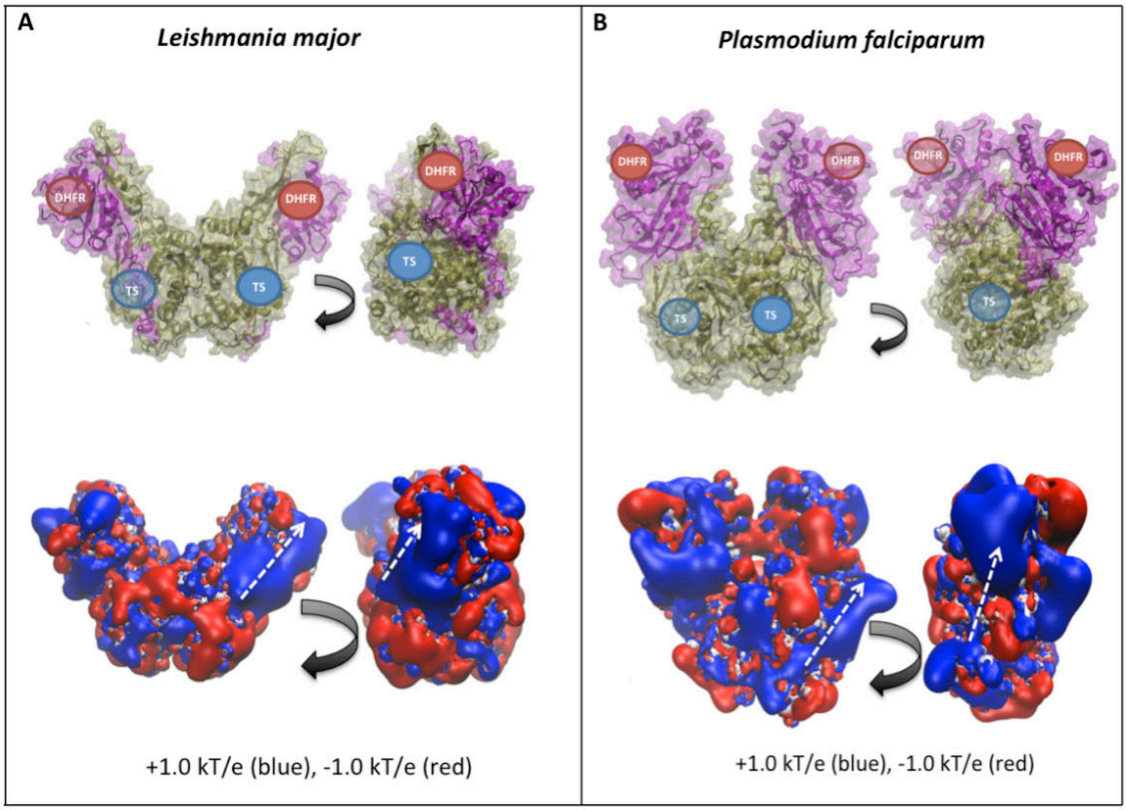

Figure 3-1: *a)* Structure of *L. major* DHFR-TS (top) and the electrostatic potential visualization (bottom). *b)* Structure of *P. falciparum* DHFR-TS (top) showing TS and DHFR active sites and electrostatic potential visualization (bottom). The approximate location of the TS and DHFR active sites are labeled, with transparent circles representing the active-site labels that are obscured in the current view of the enzyme. *White* lines indicate hypothesized electrostatic-mediated dihydrofolate channeling path between the TS and DHFR active sites on each monomer. The electrostatic potential maps were created with APBS at physiological (150 mM) ionic strength and a pH of 7.0.

Since the x-ray crystal structure of *L. major* DHFR-TS was determined, additional structures of DHFR-TS in other protozoan species such as *P. falciparum* [56] and *C. hominis* [58] have also been solved. Interestingly, these bifunctional protozoan enzymes share a common V-shaped geometry; the main interface between the two monomers is located at the bottom of the "V" shape where the TS domains intersect (as depicted in Fig. 3-1). Because of the structural similarity between *L. major* DHFR-TS and other protozoan DHFR-TS enzymes, we hypothesized that other protozoan DHFR-TS enzymes may also support significant electrostatic channeling of dihydrofolate. However, the structurally similar DHFR-TS enzyme from *C. hominis* has been shown to not exhibit any measurable substrate channeling [59] despite multiple kinetic experiments investigating substrate channeling in this system. This experimental result suggests that different protozoan DHFR-TS enzymes may exhibit varying efficiency of substrate channeling. In these systems, it appears that substrate channeling is dependent on the magnitude and position of important attractive electrostatic interactions between dihydrofolate and the enzyme as well as the geometry and proximity of the TS active site relative to the DHFR active site. For example, the distance between the TS and DHFR active sites of *L. major* DHFR-TS is shorter than in *P. falciparum* and *C. hominis* DHFR-TS. Also, there is a greater density of basic, electropositive residues between the TS and DHFR active sites of *L. major* DHFR-TS compared to *P. falciparum* and *C. hominis* DHFR-TS.

P. falciparum DHFR-TS is a particularly important enzyme because it is from the protozoan species that is associated with most malaria infections. Since this enzyme is responsible for catalyzing sequential reactions in the thymidylate cycle, its inhibition slows malarial dTMP production and therefore interferes with the process of DNA synthesis [56]. Most antifolate antimalarial drugs act by inhibiting the DHFR activity of the *P. falciparum* enzyme [56] because there is greater structural variance between monomeric human DHFR and protozoan bifunctional DHFR domains compared to the very similar TS domains. However,

because of growing drug resistance [56], new strategies for designing novel classes of malarial drugs should be considered. If the transfer of the intermediate is highly dependent on electrostatic channeling, the disruption of this channeling could be an alternative strategy to selectively interfere with the thymidylate cycle in *P. falciparum*.

P. falciparum DHFR-TS has been suspected as an enzyme that makes use of electrostatic channeling [56,60]. The wild-type crystal structure of *P. falciparum* DHFR-TS reveals a long, winding electropositive groove that connects the TS and DHFR active sites on each monomer of the bifunctional enzyme. As shown in Fig. 3-1B and first described by Yuvaniyama et al [56], a groove exists in the solvent-accessible surface connecting the TS and DHFR active sites on each monomer and the electrostatic representations show that this groove is positively charged. Also, a second path of lower electropositive magnitude and width also appears between the TS active site of one monomer and the DHFR active site of the other monomer [56]. The electrostatic potential contour maps suggest that electrostatic channeling is possible because the TS and DHFR active sites are connected by regions of opposite charge compared to that of the channeled intermediate. As suggested by Eun et al [52], "mediators" of charge opposite to that of the channeled intermediate can promote electrostatic channeling, even for well-separated active sites. Hence, we seek to determine whether the distribution of electropositive, solvent-exposed amino acids between the DHFR and TS active sites is sufficient for dihydrofolate channeling.

In order to quantitatively measure the strength of electrostatic channeling, we calculate the transfer efficiency of newly synthesized dihydrofolate at the TS active site to the DHFR active site. A substrate channel that guides all of the intermediate synthesized at the first active site to the second active site would represent complete channeling efficiency (100% transfer efficiency), while substantial diffusion of intermediate away from the protein to the bulk solution would result in transfer efficiencies approaching 0%. Because most instances of

substrate channeling observed in nature are less than 100% [51], the transfer efficiency is an important quantity used to compare the relative "leakiness" of substrate channels. An objective of this study is to understand the magnitude of electrostatic channeling in wild type *P. falciparum* DHFR-TS through theoretical methods by using a variety of modeling approaches. To study the reaction kinetics, we employ Brownian dynamics simulations, and to calculate steady-state values, we rely on a continuum model approach. While Brownian dynamics has been the computational method of choice for studying intermediate transfer efficiencies in systems suspected of electrostatic channeling, combining this approach with a continuum method allows us to explore the properties of the system more comprehensively and to generate the steady-state intermediate concentration maps on the enzyme's solvent accessible surface.

Methods

To study electrostatic substrate channeling, we employed two methodologies: 1) Brownian dynamics and 2) a continuum model. While Brownian dynamics simulations are useful for tracking the motion of individual particles, the continuum model is convenient for calculating probabilities (ensemble averaged quantities) such as the steady-state intermediate concentration distribution on the solvent-accessible surface of an enzyme. The major difference between these methods comes from the fact that Brownian dynamics is based on the Langevin equation and the continuum model is based on the Smoluchowski equation. [52,61,62]. The equivalence of the two approaches within certain limits is well established [63]. Since each approach has its own advantages, we use both methodologies in this study of substrate channeling in *P. falciparum DHFR-TS*. Below, we describe the preparation of the molecular structures that are used in either Brownian dynamics simulations or in the continuum model. Details of each approach are also summarized below.

Preparation of Molecular Structures

The wild-type crystal structures of *P. falciparum* DHFR-TS (PDB ID 1J3I), *L. major* DHFR-TS [54], and *C. hominis* (PDB ID 1QZF) were obtained from the RCSB Protein Data Bank. The software PDB2PQR version 1.8 [45,64] was used with ProPka [65] and the CHARMM27 force-field [66] to generate a PQR file containing the coordinates, charge, and the radius of each atom in the system. ProPka [65] was implemented with pH=7.0 to assign static protonation states while running PDB2PQR. The same PQR file is used in the continuum models as well as in the Brownian dynamics simulations. APBS version 1.2.1 [46,67] was used to generate electrostatic grids in the OpenDX format at a variety of ionic strengths using Na+ and Cl- as the cation and anion, respectively. The same APBS input settings are used to create electrostatic grids for use in Brownian dynamics simulations of *P. falciparum*, *L. major* and *C. hominis* DHFR-TS enzymes.

Brownian Dynamics Simulations

For Brownian dynamics simulations, we place the DHFR-TS prepared from the PDB structures in the system and we run the channeling simulations using the Brownian dynamics simulation software package BrownDye [44] on each system implementing the Northrup-Allison-McCammon (NAM) algorithm [68]. The q and b radii for the algorithm, which are associated with the simulation system size, are automatically calculated from BrownDye as detailed in [44]. In the BrownDye simulation settings, the "start-at-site" option is used to position a dihydrofolate with net charge of -2 near the TS active site. For the purpose of comparison to the previous Brownian dynamics simulations performed by Elcock et al. on *L. major* DHFR-TS [55], we consider only one TS active site, and near this site we position the same simple 2-angstrom radius charged-sphere model of dihydrofolate (which reacts at either of the two DHFR active sites) along with similar reaction conditions at the two DHFR active sites.

After performing BrownDye simulations, the trajectory results are analyzed to compute the predicted probability of channeling to the DHFR site compared to the probability of escape into the bulk solvent. Specifically, the transfer efficiency is defined as the predicted number of "channeled" substrates divided by the sum of "channeled" substrates and substrates that escape into the bulk solution. To better understand electrostatic-mediated channeling, for some simulations, the net charge on the 2-angstrom radius dihydrofolate sphere was eliminated or altered to study proximity-mediated substrate channeling effects in the absence or reduction of electrostatic interactions between the dihydrofolate sphere and the enzyme. Also, the ionic strength is varied in some simulations to study the influence of electrostatic interactions. 10,000 BrownDye trajectories were required in each simulation of a system in order to ensure that the results are statistically reasonable. Calibrating the size of the DHFR reactive zone centered at the DHFR active site is possible because the transfer efficiency of the structurally similar protozoan *L. major* DHFR-TS enzyme has been experimentally measured. Details about the validation of the DHFR reactive-zone size are located in Section A of the Supporting Information (SI).

Continuum Model

In the continuum model, we assume that the dihydrofolate (intermediate) generated at the TS active site diffuses to the bulk and toward the DHFR active sites, where the reduction of dihydrofolate to tetrahydrofolate occurs immediately. This assumption can be implemented in a reaction-diffusion model based on the Smoluchowski equation (Eq. 1) with proper boundary conditions,

$$\frac{\partial c}{\partial t} = \nabla \cdot D\left(\nabla c + \frac{c}{k_B T}\nabla U\right) \quad (1)$$

where c, D, k_B, T, and U are the concentration of dihydrofolate, the relative diffusion constant,

the Boltzmann constant, the absolute temperature, and the external potential, respectively. In this case, U is given by the electrostatic interaction between the enzyme and the intermediate and the electrostatic potentials used in this calculation are obtained from APBS [46,67]. The operators in Eq. 1 describe the diffusive motion of intermediate under the electrostatic interaction, and the production and reaction events of the intermediate are taken into account through boundary conditions. Before we set up the boundary conditions, we first define where to apply them in the model. For the production of intermediate, similar to the Brownian dynamics simulations, we define the production zone near the TS active site, which produces dihydrofolate. However, for the reaction of intermediate, we simply define the reaction zones through the enzyme's solvent-accessible surface, as is usually implemented in a continuum model [62]. This implementation allows us to easily adjust the effective size of reaction zones, similar to the determination of reactive-zone size in the Brownian dynamics simulations. Using this strategy, we optimize the reactive-zone sizes so that the transfer efficiency in the non-electrostatic case has similar magnitude of that observed in Brownian dynamics simulation results (which were in turn calibrated using the relationship between experimentally determined channeling efficiencies in *L. major* DHFR-TS and Brownian dynamics results). With these defined zones serving as boundaries, we next define the applicable boundary conditions.

In this model, we require four boundary conditions to account for the TS zone, the DHFR zones, the non-reactive enzyme surface, and the system's outer boundary. The first boundary condition is for the production of intermediate near the TS active site given by Eq. 2.

$$\left(\nabla c + \frac{c}{k_B T}\nabla U\right) = -\kappa \hat{u} \qquad (2)$$

where $\hat{u}$ is the unit vector normal to the surface of the production zone defined near the TS

active site and κ represents the magnitude of the production flux. This gives the production rate of intermediate at the TS production zone,

$$k_{TS} = \int D(-\kappa\hat{u}) \cdot d\vec{S}_{TS} = D\kappa A_{TS} \quad (3)$$

which is the surface integral of the flux of dihydrofolate over the production zone, while A_{TS} is the area of the production zone. For the sake of simplicity, we set κ equal to 1. For the second boundary condition, we assume an absorbing condition (c=0) at the DHFR active sites, which means that the intermediate is depleted because of the reaction. The outer enzyme surface has a reflecting (non-reactive) boundary condition for the intermediate, which is the third boundary condition employed. The fourth and final boundary condition that was used is the outer boundary condition at the periphery of the entire system, for which we assumed a reflecting boundary condition.

In principle, Eq. 1 can be used to calculate the time dependent concentration of intermediate. However, here we report steady-state properties, which are difficult to calculate from Brownian dynamics simulation trajectories.

To solve the equation, we use the finite element method (FEM), which is convenient to handle the complex geometry of an enzyme. The essence of this method is to discretize the space so that the continuous domain is divided into a set of discrete subdomains, and to then assemble the element equations in the subdomains into a global system of equations to obtain the solutions. The solutions in this procedure can be well approximated to the exact solutions by forcing the residuals to zero through weak formulation, where we use the Galerkin method [69], with the original partial differential equation (PDE) problem transformed into a variational problem. The weak form corresponding to the original equation (Eq. 1) is given by Eq. 3:

$$\int_{\Omega} e^{(-\beta U(r))} \nabla u \cdot \nabla v \, dx - \int_{\mathrm{TS}} e^{(-\beta U(r))} \frac{\partial u}{\partial n} v \, ds = 0 \quad \forall v \in \hat{V} \tag{3}$$

where Ω is the spatial domain, and TS is the production zone of intermediate. v is the function called a test function in some function space $\hat{V}$ such that v is zero on the parts of the boundary where u is known. u is the function to be approximated to the exact solution, referred to as a trial function. $\partial u/\partial n$ is the derivative of u in the outward direction at the TS boundary.

Here, we apply the Galerkin method for the weak form given in Eq. 3, and this leads to a linear algebraic problem. However, when $\beta U(r) \gg 1$, we encounter an ill-conditioned linear problem. To avoid this difficulty, we only consider the weak potential region where $\beta U(r) \leq 1$. Because of this approximation, we use Brownian dynamics simulations as the main investigative tool. Moreover, due to the limitation, we applied the continuum method to the high ionic strength regime (≥150 mM). For this entire numerical procedure, we use the program Smolfin specialized for solving Smoluchowski-type equations [62], which is based on the finite element method software package, FEniCS [70].

After solving the equation, we calculate the transfer efficiency in the steady-state by dividing the total reaction rates on the DHFR reaction zones by the production rate on the TS production zone. The production rate is given in Eq. 2 and the total reaction rate is given by the following equation:

$$k_{DHFR} = \int D \left(\nabla c + \frac{c}{k_B T} \nabla U \right) \cdot d\vec{S}_{DHFR,1} + \int D \left(\nabla c + \frac{c}{k_B T} \nabla U \right) \cdot d\vec{S}_{DHFR,2} \tag{4}$$

which can be summarized as the sum of surface integrals of the flux of dihydrofolate over the DHFR active sites.

Results and Discussion

Dihydrofolate Channeling Efficiency in *P. falciparum* DHFR-TS

Brownian dynamics simulations of *P. falciparum* DHFR-TS indicate that under physiological pH, ionic strength, and dihydrofolate charge (-2), the total dihydrofolate transfer efficiency is ~20%. Slightly less than half of this transfer efficiency is present with neutral (uncharged) dihydrofolate as shown in Fig. 3-2A, suggesting that at physiological conditions, electrostatic-mediated dihydrofolate channeling is a smaller effect (~15%) compared to *L.major* DHFR-TS channeling (~55%), with proximity-based substrate channeling comprising another significant source of the overall transfer efficiency.

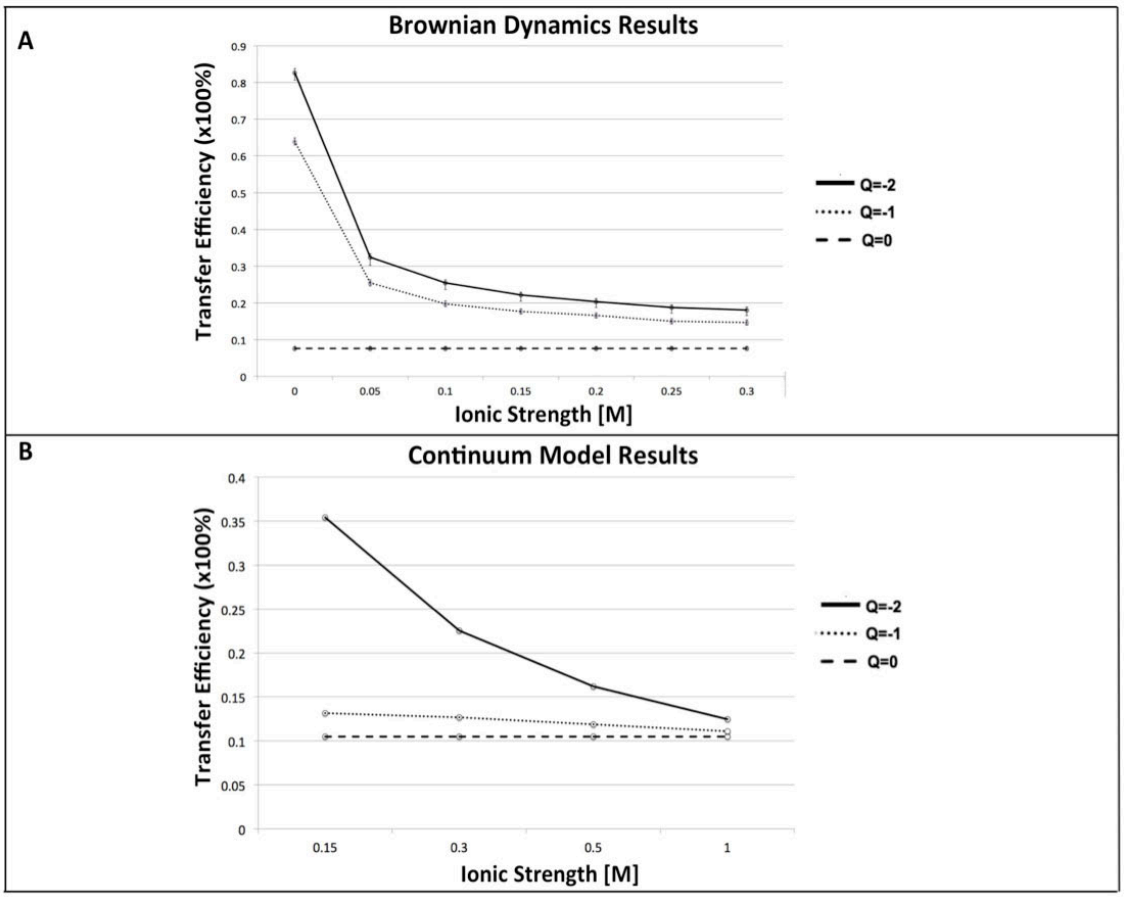

Figure 3-2: *a)* Brownian dynamics simulation results for *P. falciparum* DHFR-TS; predicted channeling efficiency vs ionic strength from 0 M to 0.3 M ionic strength. The error bars show statistical error +/- two standard deviations from the mean computed from a binomial distribution of outcomes for Brownian dynamics trajectories that either react or escape and the magnitude of this error is approximately +/- 1%. *b)* Continuum model prediction for *P. falciparum* DHFR-TS; predicted channeling efficiency vs ionic strength from physiological ionic strength (0.15 M) to 1.0 M.

As shown in Fig. 3-2B, the continuum model results also predict relatively low dihydrofolate transfer efficiency (~35%) at physiological ionic strength (150mM) and a -2 dihydrofolate charge. Since the non-electrostatic transfer efficiency is ~10% in both cases, the electrostatic contribution to the transfer efficiency is ~15% in the Brownian dynamics simulations and ~25% in the continuum model. The difference in the results obtained using these two methods appears to be caused by the excluded volume of dihydrofolate which is only considered in the Brownian dynamics simulations. In the continuum model, the dihydrofolate is represented as a point-charge. For both the Brownian dynamics simulation results as well as the continuum model results, we observe a significant decrease in the dihydrofolate transfer efficiency of the system as the dihydrofolate charge is increased from -2 to 0. Additionally, both models indicate that the transfer efficiency for the charged cases (dihydrofolate with charges of -2 and -1) decreases as the ionic strength is increased. Although the most biologically relevant case is at physiological ionic strength (0.15M) and with a -2 dihydrofolate charge, it is informative to calculate the predicted dihydrofolate transfer efficiency at other ionic strengths, including non-physiological ionic strengths. At the low ionic strengths investigated in the Brownian dynamics simulations (Fig. 3-2A), a high (<80%) transfer efficiency is observed, but this transfer efficiency decreases significantly as the ionic strength is increased to physiological ionic strength (0.15M) and higher. Consistent with this observation, as the ionic strength is increased from physiological ionic strength in the continuum model, a similar trend in decreased transfer efficiency is observed, and the transfer efficiency in the electrostatic cases (-2 and -1 charges) converge to what is calculated in the non-electrostatic case (0 charge).

In addition to the transfer efficiency in the steady-state cases, the continuum model results are useful for visualizing the steady-state dihydrofolate concentration map along the solvent-exposed surface of *P. falciparum* DHFR-TS as depicted in Fig. 3-3.

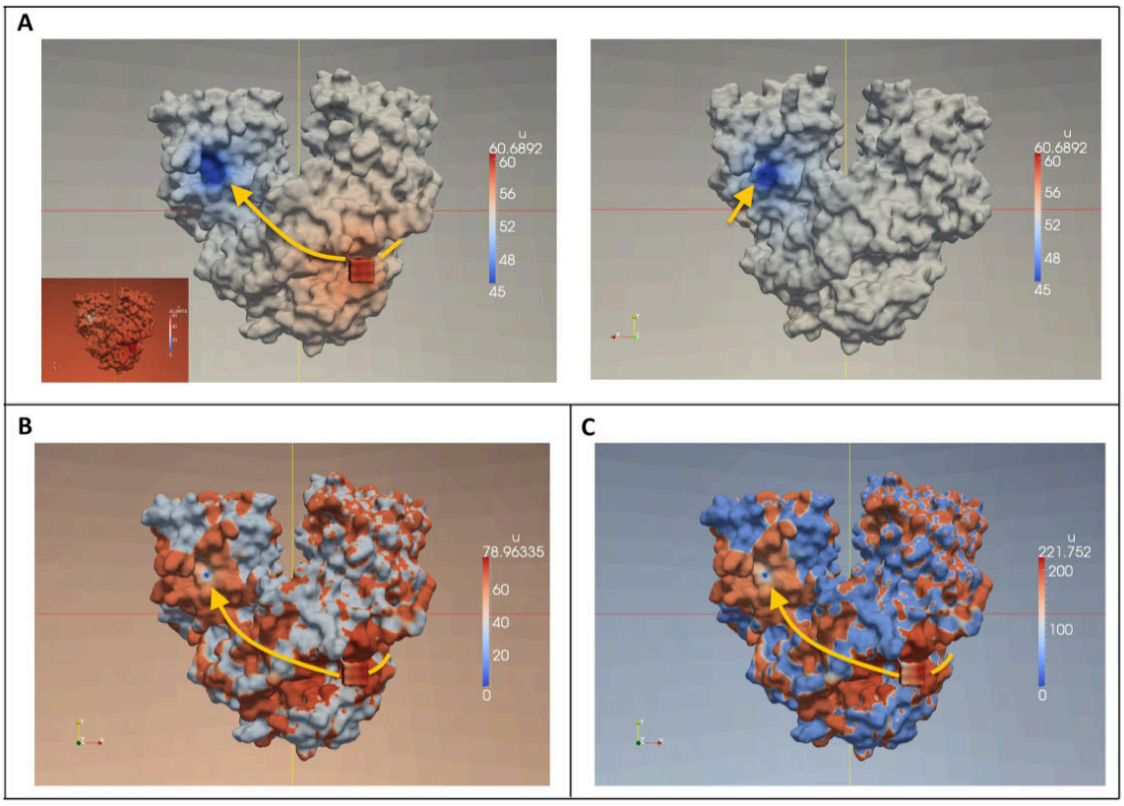

Figure 3-3. *a)* Steady-state concentration maps of intermediate with a charge of 0 on the front side (left) and on the back-side (right). To clearly see the active sites, source (*red*) and sink (*blue*), we change the lower limit of concentration in the color scheme from 0 to 45. The original color map is depicted in the inset. *b)* The steady-state concentration map of intermediate with a charge of -1 on the front side of the bifunctional enzyme. *c)* The steady-state concentration map of intermediate with a charge of -2 on the front side of the bifunctional enzyme. The *orange* lines indicate electrostatic channeling pathways on the enzyme surface. Here, the concentration has arbitrary unit, which is determined by the production rate given in Eq 2. If we increase the magnitude of flux ($\hat{u}$), the scale of concentration is increased.

In Fig. 3-3, the intermediate steady state distribution is shown along the enzyme surface. When the electric charge of the intermediate is set to zero (see Fig. 3-3A), we can clearly see the concentration gradient formed between the production zone (red) and the reaction zones (blue; front side in the left and back side in the right). Also, the color is smoothly changing along the enzyme's solvent accessible surface from the source (red) to the sinks (blue). In contrast, as the electric charge becomes more negative from 0 to -1 (Fig. 3-3B) or -2 (Fig. 3-3C), we observe a sharp concentration change on the enzyme surface according to the electrostatic potential of *P. falciparum* DHFR-TS (Fig. 3-1B). This inhomogeneous concentration distribution underlies why *P. falciparum* DHFR-TS has lower transfer efficiency than *L. major* DHFR. Namely, the electrostatic repulsion surrounding the hypothesized electrostatic channeling pathways in *P. falciparum* DHFR-TS (orange lines in Fig. 3-3) restrict the calculated concentration of intermediate to a narrow region. In contrast, *L. major* DHFR-TS is expected to have more prominent electrostatic channeling paths between the active sites due to increased electrostatic attractions between the enzyme and the intermediate (see Fig. 3-1A for an electrostatic visualization of *L. major* DHFR-TS; the blue electropositive region covers a fair amount of the area including the TS and DHFR active sites).

Comparison between Protozoan DHFR-TS Enzymes

Although our main focus is on the electrostatic channeling of dihydrofolate in *P. falciparum* DHFR-TS, to see if this inefficient channeling observed in *P. falciparum* DHFR-TS is exceptional or general in the family of protozoan DHFR-TS enzymes, we include one more protozoan species, *C. hominis*, of the bifunctional DHFR-TS enzyme family that has been the focus of experimental kinetic studies [59], and we calculate the dihydrofolate channeling efficiency to compare the channeling efficiency between three species of protozoan DHFR-TS enzymes (*P. falciparum*, *L.major* and *C.hominis)*. It is known that *L.major* DHFR-TS exhibits

substantial dihydrofolate channeling with some predictions of 80% or greater transfer efficiency [54], while dihydrofolate channeling in *C.hominis* DHFR-TS is known to be minimal or nonexistent [59]. 3-4A shows Brownian dynamics results for three species of bifunctional DHFR-TS enzymes at 150 mM ionic strength, including the focus of this investigation, *P. falciparum* DHFR-TS.

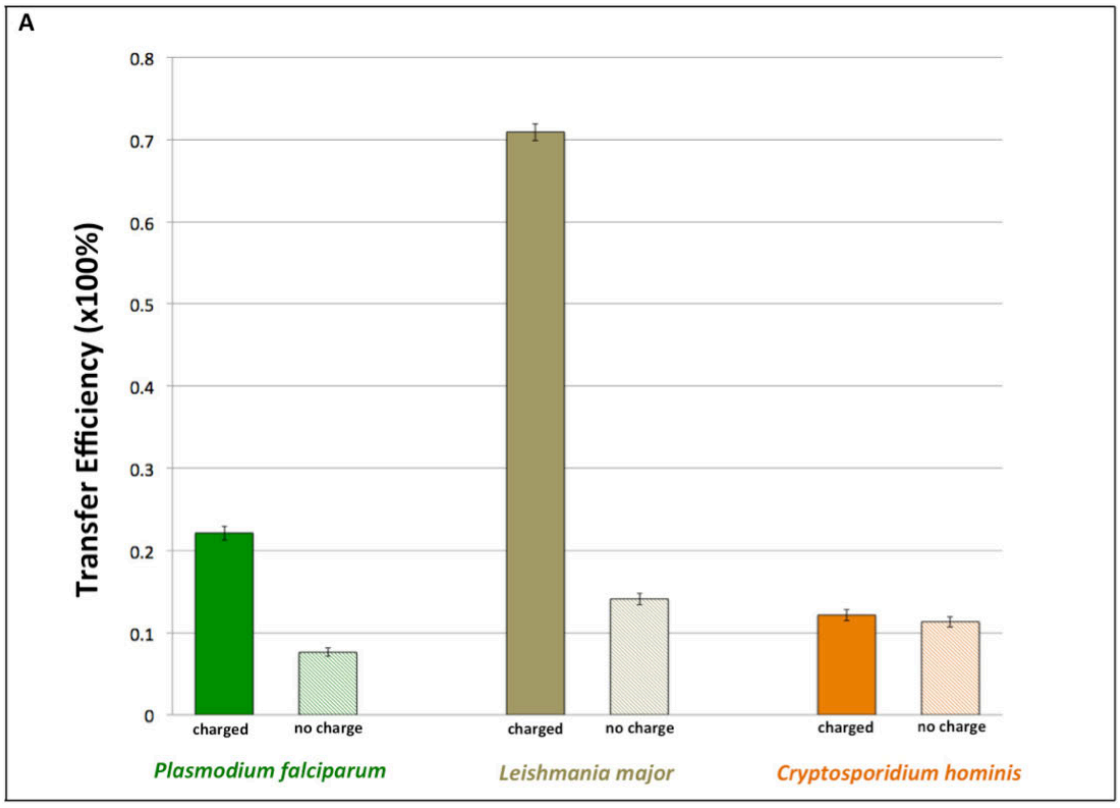

Figure 3-4. Brownian dynamics simulation results showing predicted dihydrofolate channeling for DHFR-TS from three protozoan species (*P. falciparum, L. major, and C. hominis*) at physiological ionic strength (150mM). The "no charge" simulations exclude all protein-substrate electrostatic interactions, while the "charged" simulations were performed at pH=7 and 150mM ionic strength with a -2 net charge on the dihydrofolate sphere. The DHFR "reactive-region" size was kept constant in the three species of DHFR-TS enzymes (the 12.5 Angstrom radius sphere size that was calibrated in Supporting Figure S1). The error bars show statistical error as computed in Fig. 3-2.

Consistent with the experimental results, *L major* and *C. hominis* DHFR-TS enzymes exhibit high and low channeling efficiencies, respectively. The predicted transfer efficiency of *P. falciparum* DHFR-TS is significantly greater than the low (~10%) levels of channeling efficiency of *C. hominis* DHFR-TS, but is still much lower than the high (< 70 %) transfer efficiency of *L.major* DHFR-TS. Thus, *P. falciparum* DHFR-TS has moderate transfer efficiency among these three species and this implies that the transfer efficiency could vary, depending on the molecular geometry and electrostatic environment of each enzyme. For example, in *L. major* DHFR-TS, the distance between the TS and DHFR active sites on a monomer of the enzyme is ~15 angstroms shorter than on *P. falciparum* DHFR-TS (Fig. 3-1), and therefore when comparing the "no-charge" cases of *P. falciparum* and *L. major* DHFR-TS in Fig. 3-4, *L. major* DHFR-TS has higher transfer efficiency, indicating that shorter distances between consecutive active-sites are beneficial for proximal substrate channeling [52,71]. Additionally, a more favourable electrostatic potential for transferring dihydrofolate in *L. major* DHFR-TS increases the transfer efficiency further than in *P. falcipar*um DHFR-TS. Finally, it is important to note that while experiments have not detected dihydrofolate channeling in *C. hominis* DHFR-TS, these Brownian dynamics results suggest that some proximity-mediated dihydrofolate channeling appears to occur in this system, although there does not seem to be any statistically significant electrostatic-mediated dihydrofolate channeling in *C. hominis* DHFR-TS, which is consistent with experimental results [59].

The Structural and Biophysical Basis for Channeling in *P. falciparum* DFHR-TS

Although the electrostatic-mediated dihydrofolate transfer between TS and DHFR in the *P. falciparum* enzyme is modest, we further investigate the cause of this electrostatic channeling by modulating the electrostatic interactions in this system. To do so, we create a "charge-removed" *P. falciparum* DHFR-TS system that was created by assigning zero charge to

all atoms in a series of “key basic residues” identified and listed in [56] that helps to form electropositive grooves in the enzyme’s solvent-accessible surface (See Supporting Information Section C for complete list of residues). These electropositive “grooves” have been postulated as being responsible for promoting electrostatic-mediated dihydrofolate channeling. In order to understand whether these key basic residues (lysine and arginine residues) are indeed associated with electrostatic-mediated dihydrofolate transfer in *P. falciparum* DHFR-TS, Brownian dynamics simulation results (Fig. 3-5A) as well as continuum model results (Fig. 3-5B) for both the wild-type *P. falciparum* DHFR-TS and the “charge-removed” *P. falciparum* DHFR-TS were compared.

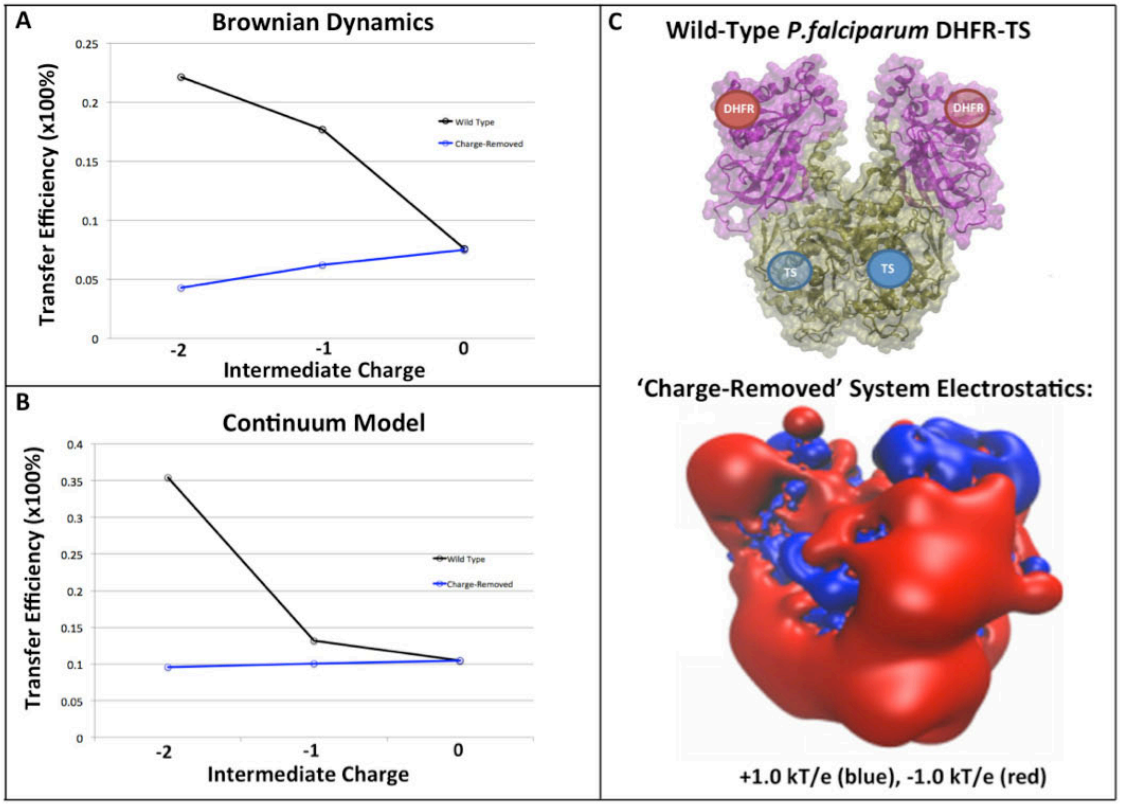

Figure 3-5: *a)* Brownian dynamics simulation results of *P. falciparum* DHFR-TS showing the relationship between the predicted dihydrofolate channeling efficiency and the charge assigned to the 2 angstrom-radius sphere dihydrofolate model. The dihydrofolate transfer efficiency for a "charge-removed" *P. falciparum* DHFR-TS system that lacks charges on key basic residues (*blue*) is compared to the wild-type results (*black*). *b)* Continuum model results showing the calculated dihydrofolate channeling efficiency of *P. falciparum* DHFR-TS using a dihydrofolate charge of 0, -1, and -2. As in panel *a*, the wild-type system and the "charge-removed" system results are included in black and in blue, respectively. *c)* Structure of *P. falciparum* DHFR-TS "charge-removed" system (top) and its electrostatic potential visualization (bottom) of the "charge-removed" system with +1.0 kT/e (*blue*), and -1.0 kT/e (*red*).

In both methods, we observe that the "charge-removed" system has minimal dihydrofolate channeling and is relatively insensitive to the charge (or lack of charge) on the dihydrofolate intermediate. As expected, Fig. 3-5C shows that for the "charge-removed" enzyme, the hypothesized channeling regions between the TS and DHFR active sites which are electropositive in the wild-type enzyme are negatively charged. This difference in electric charge distribution and magnitude could enhance repulsive electrostatic interactions between the intermediate and the DHFR active sites, resulting in lower transfer efficiencies in the "charge-removed" system. Furthermore, we see an opposing trend in the wild-type case that the transfer efficiency decreases as the intermediate charge is more negative. These results highlight the importance of the "key" basic residues identified in promoting dihydrofolate channeling in *P. falciparum* DHFR-TS [56]. Thus, it appears that the location and density of positive charge is the most important factor for either promoting or prohibiting electrostatic channeling.

Summary and Conclusions

By performing Brownian dynamics simulations as well as continuum modeling, we estimate the predicted transfer efficiency of dihydrofolate in *P. falciparum* DHFR-TS with electrostatic-mediated and proximity-mediated substrate channeling. Furthermore, we identify the crucial role of specific solvent-exposed basic residues in supporting this dihydrofolate channeling phenomenon. The electrostatic contribution to the total transfer efficiency is determined via comparison to the transfer efficiency in the non-electrostatic cases (it was estimated to be ~15% - ~25%) which is lower than ~55% in *L. major* DHFR-TS. This result clearly indicates that the electrostatic channeling in *P. falciparum* DHFR-TS is modest compared to the *L. major* DHFR-TS enzyme. While *L. major* DHFR-TS has an abundance of

positively charged residues connecting the TS and DHFR active sites and they are geometrically located on the same face of each monomer (See Fig 3-1A), *P. falciparum* DHFR-TS [56] has repulsive negatively charged patches near the electrostatic channeling pathways, which are also relatively long and nonlinear in geometry with the TS and DHFR active sites on each monomer facing opposite planes. This geometry requires the channeled substrate to "turn a corner" in order to reach the DHFR active sites (See Fig 3-1B), which leads to increased mixing with bulk solvent and corresponding attenuated reaction rates. Therefore, despite having similar tertiary and quaternary structures, it is clear that subtle differences in structure, active-site geometry, and charge distribution between bifunctional protozoan DHFR-TS enzymes influence both electrostatic-mediated and proximity-mediated substrate channeling. Specifically, the channeling in *P. falciparum* DHFR-TS is more prominent than what was predicted in *C. hominis*, a system known experimentally to not channel dihydrofolate, but was far less efficient channeling than in *L. major* DHFR-TS. Thus, our characterization of substrate channeling in this system suggests that suspected *P.falciparum* DHFR-TS channeling regions would not be an attractive anti-malaria drug target because it appears that the majority of dihydrofolate reaches the DHFR active site via diffusion through bulk solvent rather than through kinetic channeling.

In this study, we investigated electrostatic channeling quantitatively using computational models, however, since we used simple models, future computational studies could benefit from improvements in methodology. One improvement would be to use a flexible, more realistic model of dihydrofolate in the Brownian dynamics simulation instead of using a simple charged-sphere model of dihydrofolate. Dihydrofolate is a fairly flexible small molecule with a significant dipole moment and these substrate properties are not considered in this study or previous computational studies of electrostatic substrate channeling. It is likely that dihydrofolate adopts a range of conformations as it traverses the relatively long distance between the TS and DHFR active sites in *P. falciparum* DHFR-TS. Another potential

improvement is to take into account the non-electrostatic interactions between dihydrofolate and the enzyme, which may contribute to channeling or interfere with dihydrofolate channeling. Also, the interactions between dihydrofolate and residues on the solvent-exposed surface of the enzyme could induce conformational changes in the enzyme. Such interactions could be considered in the future with more detailed modeling efforts focused on substrate channeling. Features like this could be implemented in future advances in Brownian dynamics simulation software that incorporates flexibility to make improved predictions about the nature of transient protein-dihydrofolate interactions that may exist during dihydrofolate channeling in *P. falciparum* DHFR-TS. Additionally, future work on this system could involve extended accelerated molecular dynamics simulations [72] of the bifunctional enzyme to search for any interesting dynamics that might influence dihydrofolate channeling or any potential dynamics that might alter the geometry and proximity of the TS and DHFR active sites.

Acknowledgements

We thank Prof. Michael Holst for useful discussions regarding numerical issues in the continuum model. This work was supported in part by the Howard Hughes Medical Institute, the National Institute of Health, the National Science Foundation, the National Biomedical Computational Resource, and the Center for Theoretical Biological Physics. PKH also thanks the American Heart Association (13POST14510036) and the National Institutes of Health (NIH award 1F32HL114365-01A1) for generous postdoctoral funding. Chapter 3 is a minimally modified reprint of the material as it appears in Vincent T Metzger*, Changsun Eun*, Peter M. Kekenes-Huskey, Gary Huber, and J. Andrew McCammon. Electrostatic channeling in *P.falciparum* DHFR-TS: Brownian dynamics simulations and continuum modeling. 2014 [Biophysical Journal – currently accepted for publication with minor revisions]. I served as the

primary investigator and author of this publication.

Chapter 4: Autonomous Targeting of Infectious Superspreaders Using Engineered Transmissible Therapies

Abstract

Infectious disease treatments, both pharmaceutical and vaccine, face three universal challenges: the difficulty of targeting treatments to high-risk 'superspreader' populations who drive the great majority of disease spread, behavioral barriers in the host population (such as poor compliance and risk disinhibition), and the evolution of pathogen resistance. Here, we describe a proposed intervention that would overcome these challenges by capitalizing upon Therapeutic Interfering Particles (TIPs) that are engineered to replicate conditionally in the presence of the pathogen and spread between individuals--analogous to 'transmissible immunization' that occurs with live-attenuated vaccines (but without the potential for reversion to virulence). Building on analyses of HIV field data from sub-Saharan Africa, we construct a multi-scale model, beginning at the single-cell level, to predict the effect of TIPs on individual patient viral loads and ultimately population-level disease prevalence. Our results show that a TIP, engineered with properties based on a recent HIV gene-therapy trial, could stably lower HIV/AIDS prevalence by ~30-fold within 50 years and could complement current therapies. In contrast, optimistic antiretroviral therapy or vaccination campaigns alone could only lower HIV/AIDS prevalence by <2-fold over 50 years. The TIP's efficacy arises from its exploitation of the same risk factors as the pathogen, allowing it to autonomously penetrate superspreader populations, maintain efficacy despite behavioral disinhibition, and limit viral resistance. While demonstrated here for HIV, the TIP concept could apply broadly to many viral infectious diseases and would represent a new paradigm for disease control, away from pathogen eradication but toward robust disease suppression.

Introduction

From ‘core groups’ to ‘superspreaders’, epidemiologists have long recognized the immense potential of targeting high-risk groups for efficient control of infectious diseases [73-76] These groups are often described by the classic ‘80/20 rule’ [77] where 20% of the individuals drive 80% of disease transmission and thus dominate the overall pattern of disease prevalence. For sexually transmitted and blood-borne infections such as Hepatitis C [78], syphilis [79], and HIV-1 [80,81] (here termed HIV), superspreading is driven by high-risk sexual or needle-sharing behaviors. For many other pathogens, spanning a broad range of transmission modes and life histories, superspreading plays an important role in transmission dynamics but the underlying mechanisms remain poorly understood [76,82,83].

Targeting these superspreader subpopulations for therapeutic or preventive measures would tremendously increase the efficacy of disease control [75,76], while failure to target high-risk groups weakens efforts to achieve ‘herd immunity’ by vaccination and severely limits the ability to reduce disease at the population level [84]. Unfortunately, identifying these crucial high-risk populations requires in-depth knowledge of the social or sexual networks that underlie disease spread, which is rarely attainable [85], as well as knowledge of as-yet unknown biological correlates of risk. Further aggravating the problem of targeting superspreaders are: (i) non-healthseeking behaviors in the key populations, such as injection drug users (IDUs); and (ii) self-concealment motivated by social stigmas and criminal barriers in high-risk individuals, such as IDUs, men who have sex with men, people with extra-marital sexual partners, and commercial sex workers and their clients.

The resulting high cost and effort involved in identifying high-risk populations has meant that—despite the huge potential benefits—targeting of disease control measures to high-risk populations is often not feasible in practice [86]. Here, we propose a fundamentally different approach that obviates the need to directly identify high-risk populations by

engineering a therapeutic version of interfering particles (i.e. TIPs) that spread between individuals to autonomously target high-risk groups. The results demonstrate the potential of TIPs to control HIV in sub-Saharan Africa and we benchmark the performance of TIPs against the more familiar alternatives of antiretroviral therapy (ART), which is known to effectively reduce HIV incidence and prevalence, and a hypothetical protective vaccine against HIV. We further demonstrate that the effect of TIPs is complementary to ART programs, so our proposed therapy could be rolled out synergistically with current campaigns.

The concept: A proposal for transmissible gene therapies

The TIP concept capitalizes upon and extends the phenomenon of interfering particles that occur naturally in many viruses, spread along with the viral pathogen [87], and have demonstrated potential therapeutic efficacy against HIV [88-91]. TIPs are minimal versions of the pathogen engineered to lack the virulent replication and structural genes of the wild-type pathogen and instead encode therapeutic elements that target key host or viral processes. Since a TIP genome is significantly shorter than the wild-type virus genome, TIP genomes are synthesized at a faster rate, resulting in increased numbers of TIP genomes compared to wild-type virus genomes in the infected cell (see Text S1 in [92] and [87]). Specifically, for HIV, the proposed TIP is a lentiviral gene-therapy vector that lacks all structural and envelope genes required to self-replicate, but retains HIV's genomic packaging signals. The TIP can mobilize out of the infected cell only by co-opting wild-type HIV capsid and envelope gene-products [88]. By parasitizing a pathogen's resources, TIPs mobilize from cell to cell [88], [90] and, in a recent clinical trial, this mobilization of a gene-therapy vector against HIV did not appear to be detrimental to patient health [89]. Due to their ability to mobilize and reproduce within hosts, TIPs have the potential to decrease wild-type pathogen levels *in vivo* by many orders of magnitude [91].

By sharing all packaging elements with the wild-type pathogen, TIPs also have the potential to spread between individuals [93], and would spread via the same transmission routes as the disease-causing pathogen. In this respect, combating an infectious disease using TIPs raises unique safety and ethical concerns but bears similarity to the use of live attenuated vaccines. In particular, a recognized advantage of Oral Polio Vaccine (OPV) is that it replicates *in vivo* and sheds, thereby transmitting among susceptible hosts and delivering additional protection via 'transmissible immunization' at the population scale [94]. There are, however, crucial differences between TIPs and live attenuated vaccines: (i) TIPs cannot replicate in uninfected hosts and, at most, the TIP will remain dormant until the host is coinfected by wildtype pathogen [95]; and (ii) replication elements are missing from the TIP, so, unlike OPV, TIP cannot revert to virulence in healthy individuals.

Results/Discussion

Projected impact of TIPs as HIV control measures

To test whether a TIP against HIV could autonomously target high-risk groups, and effectively reduce HIV prevalence, we build upon an established epidemiological model of HIV/AIDS transmission in sub-Saharan Africa that includes four classes of sexual risk behavior based on field data [84]. We develop a data-driven, three-scale model (Fig. 4-1) that translates molecular-level characteristics of the TIP to predict patient-level HIV viral load and ultimately predict HIV/AIDS incidence and prevalence at the population scale. At the single-cell level, the model considers the dynamics of competition between TIP genomic mRNA and HIV genomic mRNA for packaging components [96]. These molecular-level effects of the TIP are translated to viral loads using an established *in vivo* model of HIV dynamics [97] that includes TIP dynamics [91]. Measured relationships between viral load and transmission [98] are used to

estimate TIP and HIV transmission rates between individuals, and the rate of disease progression is estimated based on field data of HIV viral load [99] (see Text S1 in [92] for details).

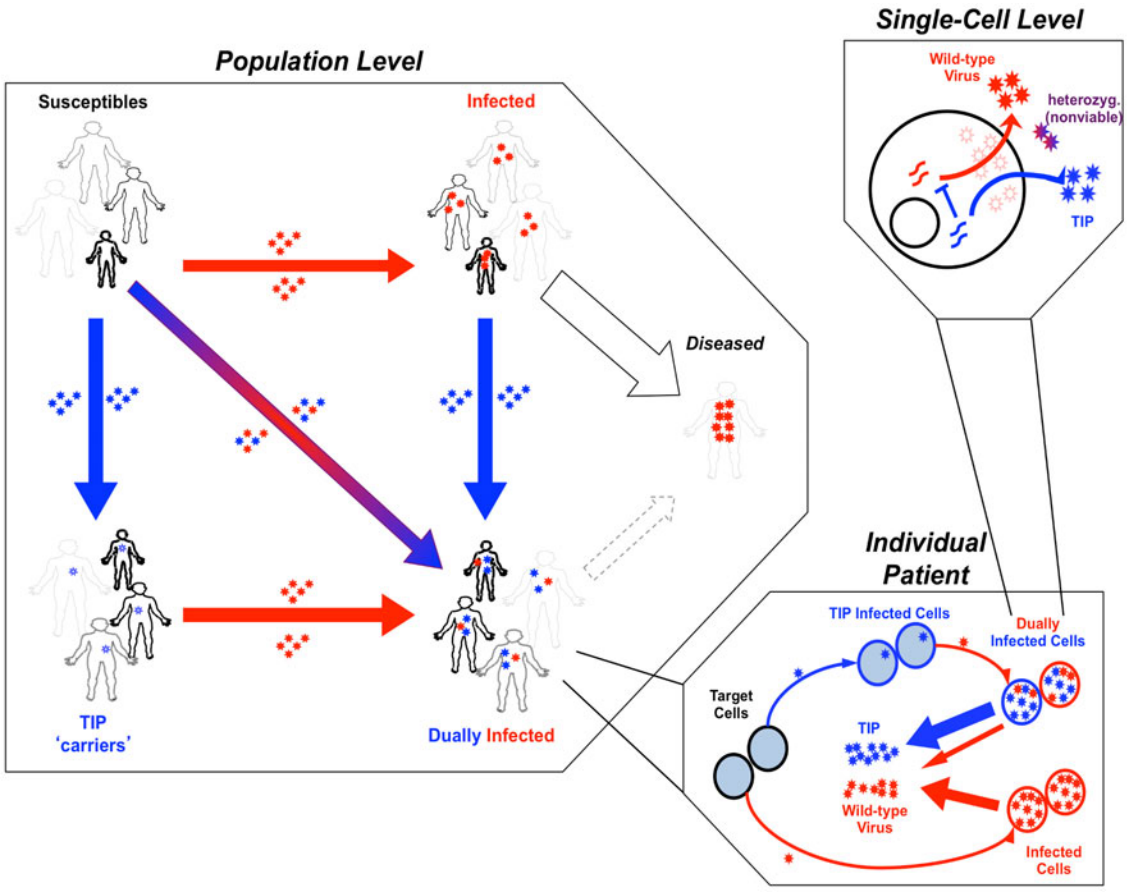

Figure 4-1. Therapeutic Interfering Particle (TIP) intervention modeled at multiple scales. (*Upper right box*) Schematic of the sub-cellular level model where TIP genomes (blue) mobilize by 'stealing' packaging elements from the wild-type virus (red, e.g. HIV) within a dually infected cell [95]. (*Lower right box*) Schematic of the *in vivo* model where TIP (blue) is produced from dually infected cells and reduces wild-type HIV viral set-point [91] within a dually infected individual. (*Left box*) Schematic of the population model where TIP and HIV transmit between individuals of different sexual activity classes (based on UNAIDS Malawi antenatal clinic data [84]). Boldness of figures represents transmission rate, size of figures represents size of sexual activity class. Smallest but boldest figures represent the superspreaders (the least in number but the highest transmission rate). Largest but lightest figures represent individuals with the lowest transmission rates (the greatest in number). Infection by TIP alone (blue) converts susceptible individuals to into latent 'carriers' of integrated TIP genomes [95]. Infection by HIV converts susceptible individuals to individuals who progress to disease in ~10 yrs. Dual infection generates individuals who progress to disease more slowly. Disease progression and transmission rates are proportional to *in vivo* viral loads [98].

For ART, the model assumes an optimistic 'test-and-treat' deployment [100] where 75% of all infections in both high-risk and low-risk populations are treated with regimens that stop 99% of all HIV transmission [100]. Our test-and-treat model differs from some previous projections [100,101] by incorporating two additional behavioral factors described in real populations [102]: (i) ART failure or dropout rates that have been measured in sub-Saharan African populations [103-105]; (ii) population risk structure. While our model predicts smaller benefits from test-and-treat programs than some earlier work [100,101], the results are consistent with previous ART projections that have incorporated risk structure [84,106].

For the vaccine, the model assumes optimistic immunization coverage (80% or 95% coverage) of both high-risk and low-risk populations and considers a vaccine that is 30% protective, slightly higher than reported in the recent 'Thai trial' [107], or a hypothetical 50% protective vaccine; life-long efficacy is assumed for both vaccines (i.e. no HIV mutational escape) but not for the TIP. For the TIPs, we analyze interventions that generate a 0.5-Log to 1.5-Log viral-load reduction *in vivo*, as reported in a recent HIV gene-therapy trial [89]. The model predicts the effects of vaccination or TIP intervention on HIV/AIDS prevalence in a resource-poor sub-Saharan setting.

Strikingly, TIP intervention reduces disease prevalence and incidence more effectively than either widespread ART or a 30% or 50% protective vaccine against HIV/AIDS (Fig. 4-2a – Fig. 4-2b). The least effective TIP analyzed—which reduces HIV *in vivo* viral load by 0.5-Log (from 10^5 to $10^{4.5}$ copies/mL)—leads to a reduction in HIV/AIDS prevalence from 29% to 6.5% in 50 years, despite initial deployment to only 1% of individuals while a TIP that generates a 1.5-Log decrease in HIV viral-load—as transiently achieved in a Phase-I clinical trial for an HIV gene-therapy [89] —would reduce HIV/AIDS prevalence from 29% to below 1% prevalence in 30 years (Fig. 4-2a). In comparison, a 30% protective vaccine deployed to 80% of

the entire population (including 8 out of 10 uninfected high-risk individuals) reduces HIV/AIDS prevalence from 29% to 23.9% in 50 years and a 50% protective vaccine deployed to 95% of the entire population (including virtually all uninfected high-risk individuals) reduces HIV/AIDS prevalence from 29% to 18.7% in 50 years. ART to treat 75% of all new infections would reduce disease prevalence to a level between a 30% and 50% protective vaccine. A striking short-term impact of TIP intervention on HIV incidence, as compared to vaccines and ART, is also projected (Fig. 4-2B) despite extremely rapid rollout of vaccines and ART (See Figure S1 in [92]). Similar results are obtained when comparing TIP intervention to vaccination and ART in terms of either the fraction-of-individuals-living-with-AIDS or AIDS incidence (Figure S2 in [92]). Thus, TIPs constructed using parameters recently reported in Phase-I trials [89], and given to a small fraction of the population (1%), have the potential to swiftly and substantially reduce disease burden at the population level.

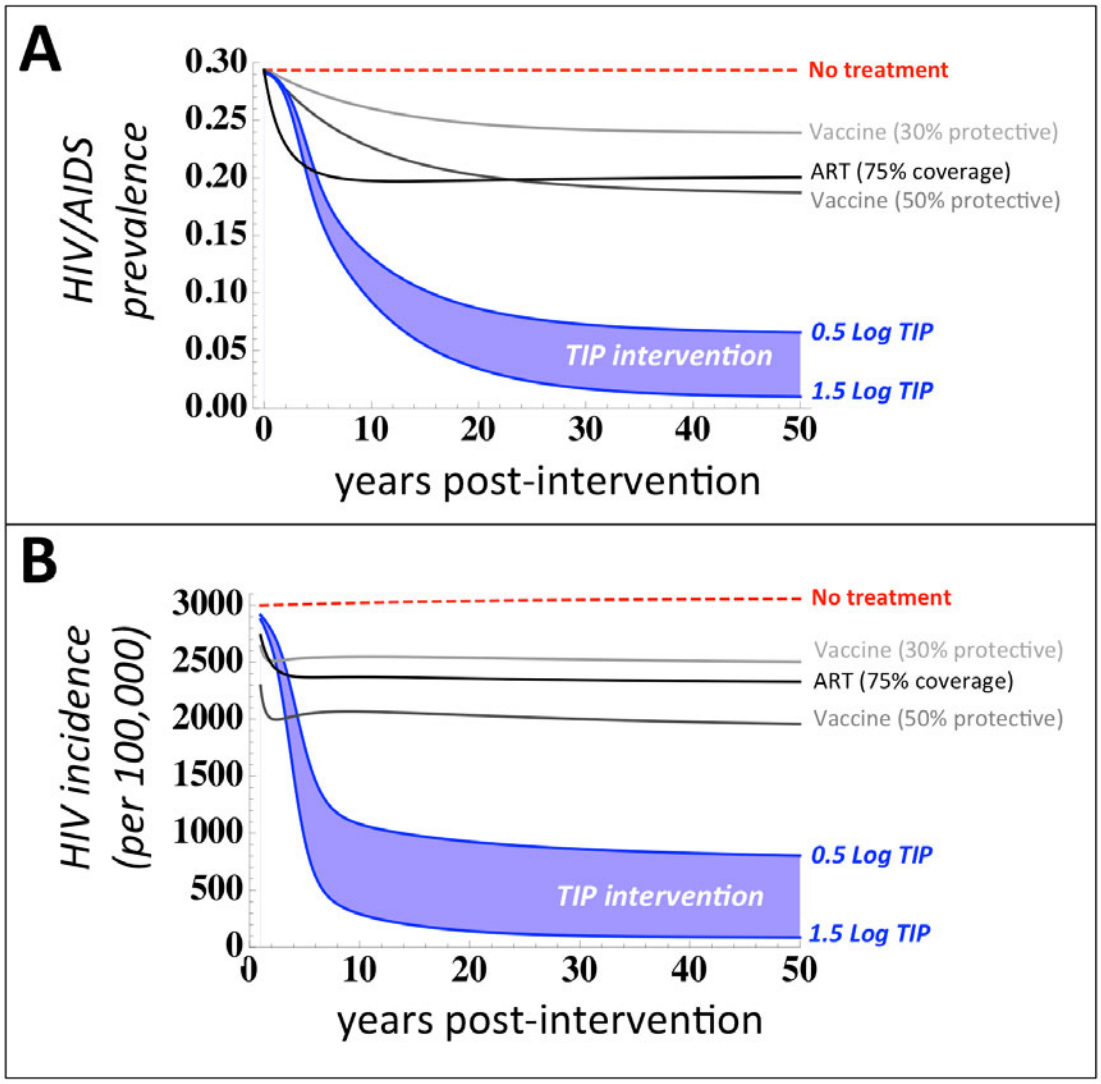

Figure 4-2. TIPs out-perform optimistic HIV vaccines and antiretroviral therapy (ART)**.**
Projected impact of TIP intervention on *a*) HIV/AIDS disease prevalence over 50 years *b*) and HIV incidence per 100,000 individuals over 30 years, for two scenarios of TIP efficacy: a 0.5-Log viral-load reduction (upper *blue* line) and a 1.5-Log viral load reduction (lower *blue* line), based on a recent clinical trial [89], both initially deployed to 1% of individuals. TIP intervention is compared to a 30% protective vaccine (*light grey*), a 50% protective vaccine (*dark grey*), and ART (*black*). Vaccine scenarios are based on protection levels reported in a recent clinical trial [107] and UNAIDS target protection goals (50% protection) where each vaccine is assumed to have lifelong efficacy and optimistic levels of coverage (80% and 95% coverage of all risk groups, respectively). The ART scenario is assumed to treat 75% of all infections using a universal test-and-treat approach [100] where ART has 99% efficacy in halting HIV transmission.

This efficacy and robustness of TIP intervention arises from the unique and defining ability of TIPs to transmit between hosts. Analysis of TIPs that generate a 0.5–1.5 Log decrease in viral load, but do not transmit between hosts, shows only a minimal decrease in population-level disease burden (Figure S3 in [92])—in agreement with the projected impact of acyclovir treatment which also generates a ~0.5 Log decrease in HIV viral load [106]. Accordingly, we have paid particular attention to ensuring that our results are robust with respect to changes in basic model assumptions about transmission biology and robust under parameter sensitivity analysis (see Text S1 in [92]). We also consider two competing models of HIV transmission biology—infection by either a single 'founder' virus that enters the new host individual or 'bottlenecking' where multiple viruses enter and replicate locally but are then winnowed down by competition within the host [108-110] —and we provide arguments that our treatment of TIP transmission is consistent with either transmission mode and that TIPs could transmit efficiently in either case (refer to Text S1 in [92] section entitled: "*Considerations for TIP transmission to uninfected hosts*"). To be completely sure that our model results are robust to changes in assumptions about TIP transmission, we repeated the simulations under the worst-case assumption that TIPs are completely unable to transmit in the absence of HIV, and found results that are qualitatively unchanged from Fig. 4-2 (refer to Text S1 [92] section: "*Sensitivity of model to removal of independent transmission of TIPs (i.e. removal of S_T individuals)*"). This somewhat surprising result arises because TIPs autonomously target the highest-risk groups, which are highly likely to be already infected with HIV due to their high-risk status, and thus the majority of the TIP infection 'flow' occurs through the already infected individuals. In summary, while there is physiological basis to support that TIPs could transmit efficiently to HIV-uninfected persons, the efficacy of TIP intervention is largely independent of this

assumption (i.e. TIPs need not convert susceptible individuals into 'TIP carriers' for population-level efficacy to be retained).

These results are not intended to argue that ART campaigns be abandoned or vaccine trials be halted. On the contrary, as we show below, the TIP's ability to target high-risk groups allows the TIP to complement ART (or vaccine) campaigns and significantly enhance the population-level efficacy of these approaches.

TIPs would circumvent behavioral barriers and complement pharmaceutical treatment

Current prevention and treatment approaches also face the challenges of poor compliance and behavioral disinhibition, wherein successful disease control leads to a reduced sense of personal risk from the disease and can result in increases in risk behavior. Disinhibition is a significant concern for current HIV prevention and control [111] and has the potential to generate the perverse outcome that a successful therapeutic may actually increase HIV incidence [112]. The transmissibility and single-dose administration of TIPs effectively circumvent these problems, unlike current pharmaceutical approaches (i.e. ART) or vaccination. Indeed, the public health benefits of TIPs are uniquely robust to disinhibition, since the intervention spreads more effectively if contact rates increase (Fig. 4-3A). In contrast, the same degree of disinhibition in the presence of ART or a 30% or 50% protective vaccine could have the unfortunate effect of increasing HIV/AIDS prevalence and could increase the number of deaths due to AIDS (Fig. 4-3B), as highlighted by previous analyses [112].

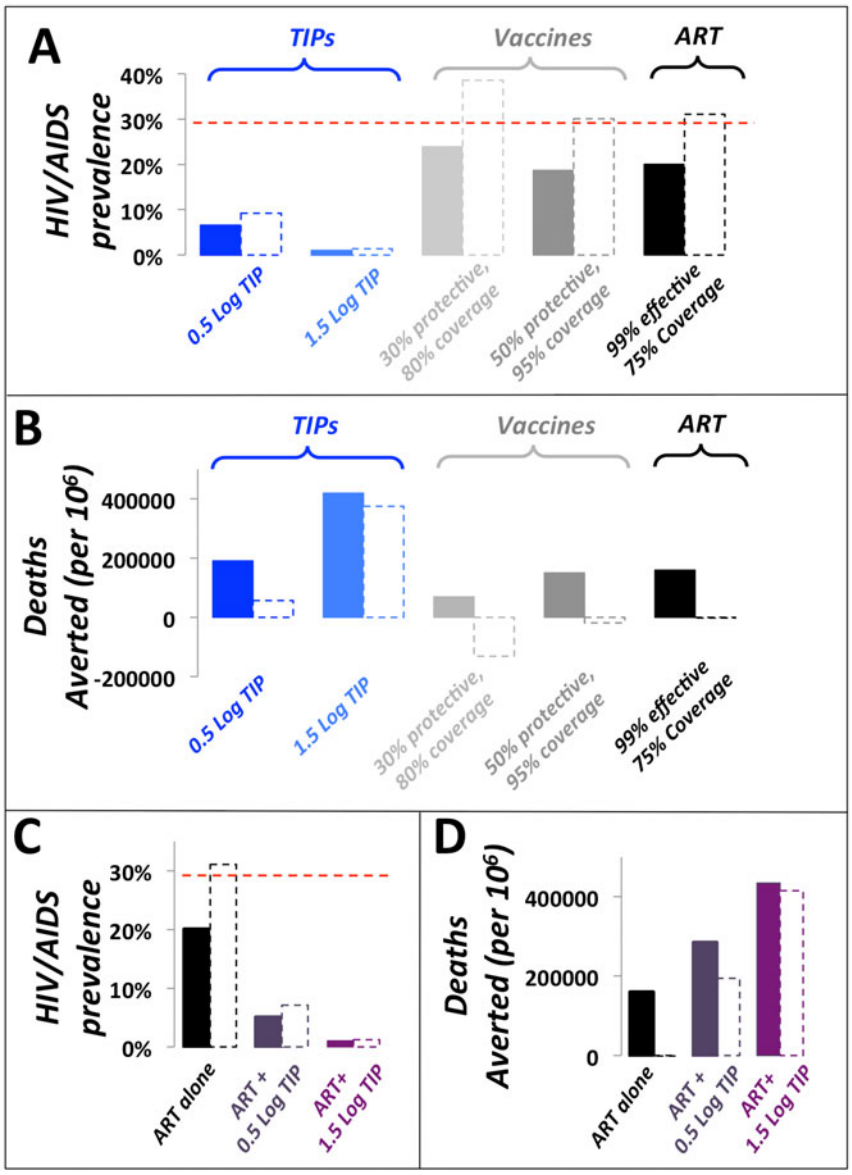

Figure 4-3. TIPs are resistant to behavioral disinhibition and could complement pharmaceutical approaches to reduce HIV/AIDS disease prevalence. Projected 50-year impact of TIP intervention on *a*) HIV/AIDS disease prevalence and *b*) number of deaths averted in the presence and absence of behavioral disinhibition (*dashed and solid lines*, respectively). TIP interventions (*light and dark blue*) are compared to vaccination (*light and dark grey*), ART (*black*), and the scenario of no intervention (*dashed red line*). Disinhibition is modeled as in [112] by assuming that individual person-to-person contact rates increase upon introduction of vaccine or TIP intervention. Projected 50-year impact of ART in presence of TIP intervention (*light and dark purple*) on *c*) HIV/AIDS disease prevalence and *d*) number of deaths averted compared to projected 50-year impact of ART alone (*black*, 75% ART coverage without TIP intervention). *Dashed and solid* lines are the presence and absence of behavioral disinhibition, respectively. ART and vaccine campaigns are modeled as in Figure 4-2.

Any intervention against HIV is likely to be administered in the context of the existing 'standard of care': ART. Since ART halts HIV transmission, ART would also halt TIP transmission from an individual, leading to the potential that the TIP intervention could be severely hampered. However, the TIP's ability to concentrate in highest-risk groups (see next paragraph), where ART is at best the target coverage fraction (e.g. 75%), would allow TIP intervention to maintain efficacy, reduce HIV/AIDS disease prevalence, and reduce AIDS deaths, more effectively than ART alone, even under optimistic coverage scenarios for ART campaigns (Fig. 4-3C – Fig. 4-3D). Thus, ART would not interfere with TIP intervention at the population scale, and TIPs could be used as a powerful complement to ART and pharmaceutical treatments in general.

TIPs would autonomously target high-risk groups

The increased efficacy of TIPs relative to vaccination is due to the TIP's transmissibility along the same transmission routes as the pathogen. Consequently, the TIP transmits to a specific risk group in proportion to that group's risk behavior, leading to more focused targeting of TIPs in more heterogeneous populations and resulting in TIPs concentrating in the highest-risk populations (Fig. 4-4A). In contrast, reaching high-risk classes with ART depends upon active and sustained targeting of these rare high-risk individuals, while partially-protective vaccines tend to concentrate in the lowest risk classes (because higher-risk individuals still become HIV-infected, given partially protective vaccines) and lack the ability to dynamically redistribute between risk classes (Fig. 4-4B).

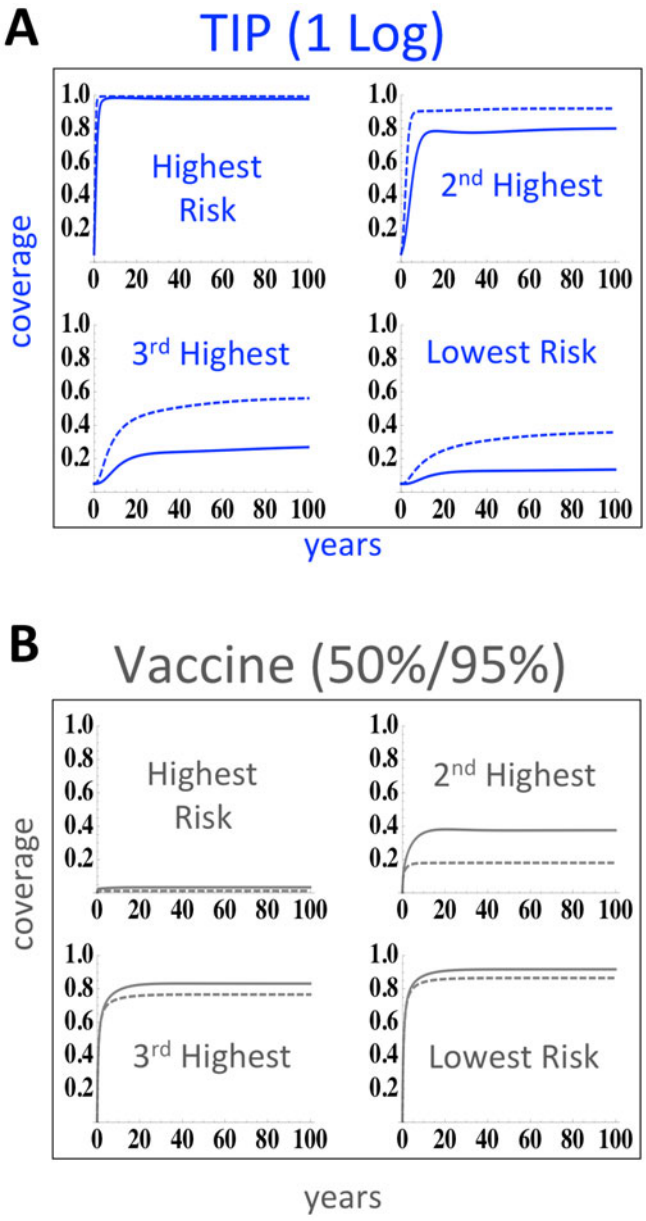

Figure 4-4. TIPs autonomously target superspreaders. *a*) Ability of TIP intervention to penetrate each risk-class as reported by fraction of each risk-class exposed to intervention over time. Despite introduction into far more individuals in the lowest risk class (due to our assumption of uniform 1% initial coverage), TIPs can mobilize into the highest risk superspreader class. *Solid* and *dashed* lines represent simulations in the presence of behavioral disinhibition, respectively. *b*) Ability of 50% protective vaccine, administered to 95% of the population, to penetrate each risk-class as reported by fraction of each risk-class exposed to vaccination over time. *Solid* and *dashed* lines represent simulations in the presence of behavioral disinhibition, respectively. In contrast to TIPs, a 50% protective vaccine that is directly targeted to the highest risk class is quickly depleted from the highest risk-class because, given partial protection, high-risk individuals still become infected relatively rapidly.

Evolutionary Considerations

Vaccines and drug treatment strategies also face the challenge of mutation and the strong selective pressure for the pathogen to escape any successful control. For HIV, rapid mutation leads to resistance against anti-retroviral therapy and poses significant challenges for vaccine development [113]. However, unlike conventional therapies, TIPs replicate with the same speed and mutation rate as the pathogen, which sets up an evolutionary arms race between the TIP and the pathogen.

To examine how HIV might respond in such an arms race resulting from TIP intervention, we consider the multi-scale dynamics across a range of parameter values for the molecular-level properties used to design a TIP. Specifically, we consider the interplay of HIV and TIP levels as a function of both the strength of TIP-encoded inhibition of HIV and the engineered TIP genomic abundance within a dually infected cell. For HIV, the TIP design encodes an inherent evolutionary tradeoff that generates conflicting selection pressures at different scales (Fig. 4-5). On the one hand, inhibition of HIV replication by TIP-encoded therapy genes inevitably limits TIP production—since any TIP-encoded antiviral that inhibits HIV will compromise the TIP's ability to mobilize. However, due to the diploid nature of retroviral genomes, high concentrations of TIP genomic mRNA alone will inhibit HIV production by wasting the majority of HIV genomes in virions containing one HIV RNA and one TIP RNA, and these heterozygous-diploid virions are not viable [90,96]. Thus, the lowest TIP-mediated inhibition generates the highest production of TIPs from an infected cell (Fig. 4-5A). The increased numbers of TIP virions then compete more effectively against HIV for target cells which generates a greater reduction in HIV viral-load at the patient-level (Fig. 4-5B), and the lowest HIV/AIDS prevalence in the population (Fig. 4-5C). These results suggest a non-intuitive design criterion for a TIP against HIV: TIPs lacking an inhibitory factor for HIV will be most effective in reducing HIV levels, both in individual patients and at the population

level. Similarly, the cellular-scale selective pressure for HIV to escape from TIP-encoded inhibition would point in the same direction (toward zero TIP inhibitory effect) and would lead to increased TIP production (Fig. 4-5A). So, counter-intuitively, HIV escape from TIP-mediated inhibition (at the molecular scale within cells) would reduce HIV viral load and HIV population prevalence to lower levels (Fig. 4-5C).

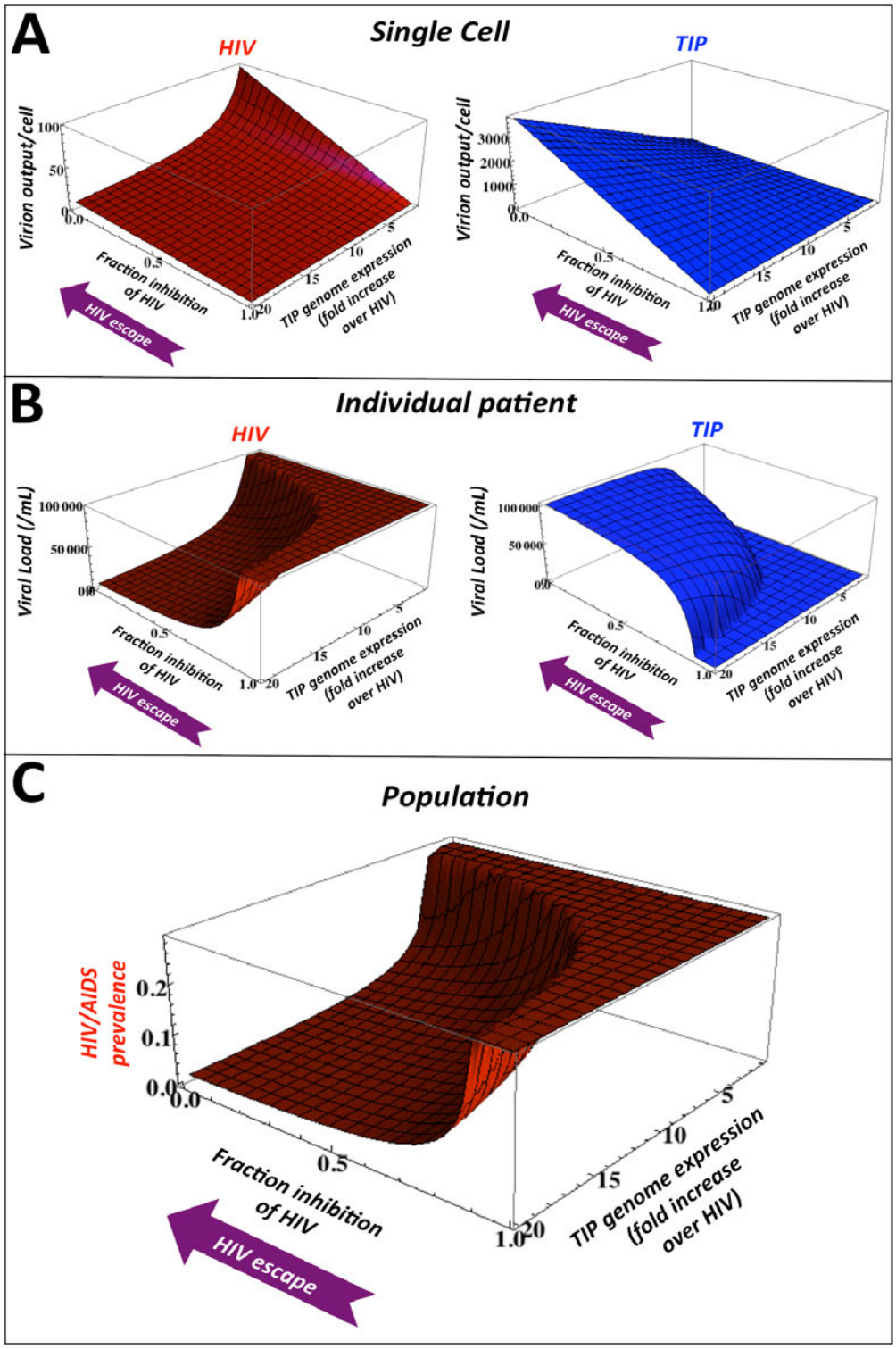

Figure 4-5. TIP intervention is robust to pathogen evolution. Projected steady-state values for: *a*) HIV and TIP production from dually infected cells at the single-cell level; *b*) HIV and TIP viral loads *in vivo*; and *c*) HIV/AIDS prevalence at the population level.

Safety and ethical considerations

The TIP approach carries unique safety concerns [114] and ethical concerns associated with introducing an intervention that transmits and evolves, even in the TIP's limited fashion, within the population. Importantly, clear ethical precedents for transmissible therapies exist in the use of live-attenuated vaccines. Regarding safety, one major concern is that the TIP may recombine with (i.e. acquire) an element that 'upregulates' pathogen production and in turn upregulates its own production from the cell. To explore this concern, we examine HIV viral load and population prevalence in the regime where TIP encodes HIV inhibition and in the regime where TIP encodes potential upregulation of HIV gene expression within a single cell. (Fig. 4-6A). As expected, at the single-cell level upregulation of HIV generates increased HIV and TIP production. However, at the individual patient level upregulation of HIV leads to increased TIP viral loads (Fig. 4-6A, inset) which actually generate even lower HIV viral loads (Fig. 4-6A) and HIV population prevalence (Fig. 4-6B). Interestingly, at the population level, there is an optimal value of TIP-encoded inhibition, which yields a maximum in TIP prevalence (Fig. 4-6B, inset). Thus, the TIP appears to be subject to competing selection pressures at multiple scales which may limit the potential for evolutionary breakdown of TIP therapies, echoing recent proposals for antivirals that resist viral escape [115] and 'evolution-proof' malaria insecticides [116].

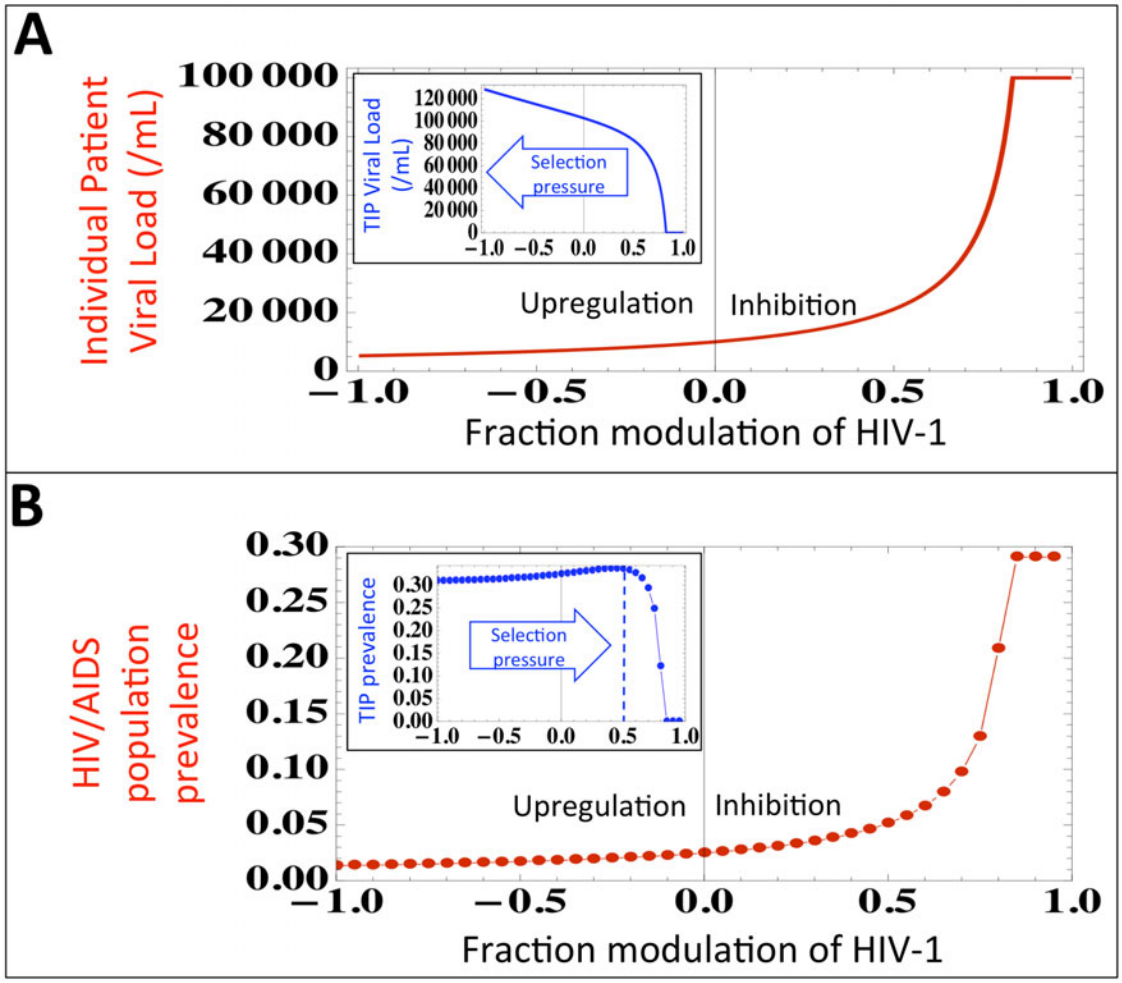

Figure 4-6. TIPs evolve toward robust reduction in disease prevalence. *a*) Predicted HIV viral set point as a function of TIP encoded inhibition of HIV (parameter *D* from the intracellular model, see Text S1) where negative inhibition values indicate TIP evolving to upregulate HIV gene expression within a single cell. Inset: Increasing upregulation generates higher TIP viral loads at the individual patient level and leads to lower HIV viral loads. *b*) HIV/AIDS disease prevalence as a function of TIP encoded inhibition of HIV where negative inhibition values indicate TIP evolving to upregulate HIV expression. Increasing upregulation generates lower HIV/AIDS prevalence at the population level. Inset: TIP prevalence is reduced as upregulation increases, potentially creating an evolutionary trap for the TIP.

Detailed experimental and theoretical study is required to predict the ultimate direction of TIP evolution, but the competing selection pressures may effectively constrain TIP phenotypes to a range that assures low HIV viral load and low HIV disease prevalence. TIP evolution is likely to be dominated by mutational processes, since recombination between TIPs and wild-type HIV appears to be severely limited by fundamental sequence-homology constraints on retroviral recombination [117] that render recombination between full-length 9.7 kb HIV genomes and shorter lentiviral genomes (e.g. TIP) non-competent for integration [90]. This molecular argument against recombination between HIV and TIP is also supported by data from murine models [118,119] and the recent human clinical trial data [89], neither of which detected recombination between wild-type HIV-1 and shorter lentiviral therapy vectors.

To fully address safety, there is obviously a need for cautious trials *in vitro*, and *in vivo*, before a TIP intervention could ever be considered for implementation. Importantly, TIPs for HIV would not specifically target, or require, stem cells since the TIP would target the same cells as HIV (primarily $CD4^+$ T lymphocytes) and thus oncogenic concerns as a result of insertional mutagenesis [120] are minimized. This argument is supported by a recent Phase-I lentiviral gene-therapy clinical trial for HIV [89] and previous gene therapy in peripheral blood lymphocytes in patients followed since 1995 [121], neither of which detected insertional mutagenesis or oncogenic transformation in patients.

Conclusion and the way forward

As with all models, our analysis is a relatively simple representation of a complex system and necessarily makes certain assumptions. Importantly, the TIP's robustness and efficacy stems from the unique and defining ability of TIPs to transmit between hosts and, as such, the general results presented for the TIP are qualitatively robust to changes in parameter

values or in basic model assumptions about transmission biology (see Text S1, [92]). TIP efficacy also appears qualitatively robust to decreases in transmission efficiency as a result of widespread ART coverage (Fig. 4-3C – Fig. 4-3D) or re-parameterization of transmission functions (see Text S1, [92]). Nevertheless, our analysis is intended as a first step towards motivating research into transmissible therapies, rather than a proof of efficacy. The molecular, epidemiological, and ethical bases of using TIP intervention against pathogens will require extensive study, but our results show that TIPs may offer a unique strategy for targeting both high-risk and hard-to-reach populations, overcoming behavioral barriers, and circumventing mutational escape to achieve indefinite disease suppression of HIV, and possibly other pathogens, in resource-limited settings.

As an added benefit for intervention in resource-limited settings, TIPs may have the potential to be administered as a therapy requiring only a single dose, thereby allowing for increased treatment access and minimizing treatment compliance issues. Our results shows that deploying TIPs as a therapy to even a few individuals who are already infected can reduce the prevalence of a disease to very low levels. Due to the rapid and sustained transmission dynamics in high-risk groups, the impact of TIP intervention is robust even if the TIP is quickly cleared from TIP 'carriers' so that these individuals rapidly revert back to 'susceptibles' (for details, refer to Text S1, [92]). With the ability to enter proviral latency, dormant TIPs could be complementary to ART on an individual scale, by reactivating during ART failure and acting to reduce viral load. While recent models argue that widespread ART campaigns alone could halt the HIV/AIDS pandemic [100,101], there remains significant controversy as to whether ART can succeed in reducing overall HIV transmission [84,102], especially in the presence of high-risk groups exhibiting treatment non-compliance. Significant challenges to achieving widespread ART coverage in resource-limited settings include: slower-than-hoped rollout, persistent logistical problems linked to insufficient health systems and weak infrastructure, the

need for on-going high-level donor funding, and the social stigmas that prevent people from getting tested and hence starting treatment. These factors will likely produce long-term heterogeneity in coverage, with the most impoverished and disadvantaged groups receiving the least access to ART. Based on these challenges, it is prudent to consider alternative and complementary approaches.

Materials and Methods

The multi-scale analysis of TIPs and HIV-1 is built upon previous data-driven models [84,91] and is composed of three constituent ordinary differential equation models describing dynamics at different hierarchical scales: (i) among a population of host individuals ('population level') (ii) within host individuals ('individual patient') (iii) within infected host cells ('intracellular'). The multi-scale model specifies mechanistic links between each scale and the next scale of organizational complexity (intracellular → in vivo → population level).

The population-level TIP model is a simplified version of a risk-structured model constructed from UNAIDS field-data collected from antenatal clinics in Malawi [84], which includes a risk-structure formulation with four distinct sexual-activity classes (SACs) and which we refer to as the 'Baggaley model'. Individuals are classified as susceptible (S), HIV infected (I), susceptible to HIV but infected with TIP (S_t), dually infected with HIV and TIP (I_d), as an AIDS patient with wild-type virus (A_w), or as a dually infected AIDS patient (A_d). Individuals in all disease-states are divided into SACs in accordance with field data (indicated by subscript i), except that all individuals in the A_w class are assumed (as in [84]) to have sexual contacts at the rate corresponding to the lowest risk group (SAC 4) owing to their poor health. The model equations are as follows:

$$\frac{dS_i}{dt} = \lambda\theta_i n_0 - \beta_W^I C(S_i,I_i) - \beta_W^{I_d}(1-\beta_T^{I_d})C(S_i,I_{d_i})$$
$$- \beta_W^{I_d}\beta_T^{I_d} C(S_i,I_{d_i}) - \beta_T^{I_d}(1-\beta_W^{I_d})C(S_i,I_{d_i})$$
$$- \beta_W^A C_A(S_i,A_w) - \beta_W^{A_d}\beta_T^{A_d} C_A(S_i,A_d)$$
$$- \beta_W^{A_d}(1-\beta_T^{A_d})C_A(S_i,A_d) - \beta_T^{A_d}(1-\beta_W^{A_d})C_A(S_i,A_d) - \mu S_i$$

$$\frac{dS_{t_i}}{dt} = \beta_T^{I_d}(1-\beta_W^{I_d})C(S_i,I_{d_i}) - \beta_W^I C(S_{t_i},I_i)$$
$$- \beta_W^{I_d} C(S_{t_i},I_{d_i}) + \beta_T^{A_d}(1-\beta_W^{A_d})C_A(S_i,A_d)$$
$$- \beta_W^{A_d} C_A(S_{t_i},A_d) - \beta_W^A C_A(S_{t_i},A_w) - \mu S_{t_i}$$

$$\frac{dI_i}{dt} = \beta_W^I C(S_i,I_i) + \beta_W^{I_d}(1-\beta_T^{I_d})C(S_i,I_{d_i})$$
$$- \beta_T^{I_d} C(I_i,I_{d_i}) + \beta_W^A C_A(S_i,A_w) + \beta_W^{A_d}(1-\beta_T^{A_d})C_A(S_i,A_d)$$
$$- \beta_T^{A_d} C_A(I_i,A_d) - (\mu+\gamma_1)I_i$$

$$\frac{dI_{d_i}}{dt} = \beta_W^{I_d}\beta_T^{I_d} C(S_i,I_{d_i}) + \beta_W^I C(S_{t_i},I_i) + \beta_W^{I_d} C(S_{t_i},I_{d_i})$$
$$+ \beta_T^{I_d} C(I_i,I_{d_i}) + \beta_T^{A_d} C_A(I_i,A_d) + \beta_T^{A_d}\beta_W^{A_d} C_A(S_i,A_d)$$
$$+ \beta_W^{A_d} C_A(S_{t_i},A_d) + \beta_W^A C_A(S_{t_i},A_w) - (\mu+\gamma_2(V))I_{d_i}$$

$$\frac{dA_w}{dt} = \gamma_1 \sum_{i=1}^{4} I_i - \beta_T^{I_d} C(A_w,I_{d_i}) - \beta_T^{A_d} C_A(A_w,A_d) - (\mu+\alpha)A_w$$

$$\frac{dA_d}{dt} = \gamma_2(V) \sum_{i=1}^{4} I_{d_i} + \beta_T^{I_d} C(A_w,I_{d_i}) + \beta_T^{A_d} C_A(A_w,A_d) - (\mu+\alpha)A_d$$

$$\forall i = 1,2,3,4$$

Detailed parameter definitions, values, and corresponding references are shown in Text S1 in [92]. The transmission probabilities per partnership are denoted β_X^Y where Y represents the disease state of the source of the infection, and X represents the viral strain (which is wild-type HIV, denoted X = W, for the vaccine model). The per-partnership transmission probability β_W^I (describing transmission of wild-type HIV by individuals in the I disease state) is set to agree with the weighted average of the Baggaley model [84] and β_W^A is the per-partnership probability of wild-type HIV infection originating from an AIDS patient, and is set following the Baggaley model [84]. Consideration of alternative parameterizations of the viral load transmission curve did not qualitatively affect the results (see Text S1 in [92]). The parameters β_W^I and γ_1 are static parameters that represent the transmission probability and the duration of the asymptomatic phase of individuals infected with only wild-type virus. In contrast, to describe quantities that depend on the specific design of the TIP, such as: (i) transmission probabilities, and (ii) the duration of the asymptomatic period, functions are used in place of parameters. These functions are calculated based on measured correlations between transmission, disease progression, and viral load [98,99] where viral load is predicted from the *in vivo* TIP model (see Text S1 in [92]). For example, the transmission probabilities in the presence of TIP and the duration of the asymptomatic phase in dually-infected individuals in the TIP population models are represented by functions of steady-state viral load (i.e. viral set point) as predicted by the *in vivo* model (see Text S1 [92] for a description of the transmission-probability functions). The function $\gamma_2(\mathrm{V})$ is used to compute the duration of the asymptomatic phase in dually-infected individuals, and is also calculated in Text S1 in [92].

Contacts between individuals in the TIP population model are weighted by statistically independent transmission probabilities (β) which are calculated from steady-state HIV and TIP viral loads from the *in vivo* model (see Text S1 section in [92]: 'Calculation of Transmission-

Rate Function'). There are six distinct transitions between infection classes in the TIP population model (see Text S1 in [92] for details). Briefly, contact between two individuals is represented by a contact function that considers asymmetric mixing of individuals among the four SACs:

$$C(X_i, Y) = c_i X_i \left[\varepsilon \left(\frac{Y_i}{N_i} \right) + (1 - \varepsilon) \frac{\sum_{j=1}^{4} c_j Y_j}{\sum_{j=1}^{4} c_j N_j} \right]$$

This contact function describes an individual in disease state X (and SAC *i*) becoming infected by an individual in disease state Y. The subscript *j* denotes SAC *j*, c_j is the average number of sexual partners per year in SAC *j*, and N_j is the sum of all sexually active individuals in SAC *j*. In the contact function, ε is the degree of assortative mixing with ε=1 corresponding to entirely assortative mixing and ε=0 corresponding to entirely random mixing. The first term inside the brackets of the contact function describes assortative mixing in which infected individuals are encountered in proportion to their prevalence in SAC *i*. The second term describes random contacts in which infected individuals are encountered in proportion to their contribution to all of the sexual contacts being made in the entire population. We set the mixing parameter ε equal to 0.37, as estimated in [84].

Simulation of the TIP population model is conducted as follows: the Baggaley model is allowed to reach steady-state and then a TIP is introduced to 1% of all individuals without any targeting to high-risk classes. Similar benefits were obtained using much more restrictive initial conditions (e.g. utilizing TIP as a therapy and targeting TIP to <1% of only *I* and A_w individuals in the least active SACs—SAC 3 and SAC 4—generates similar results to Fig. 4-2). Behavioral

disinhibition is simulated as in [122] by increasing the contact rates *c* for all SACs and number of AIDS deaths averted by the vaccination campaign is defined as:

AIDS deaths averted = (AIDS deaths during 100 years of epidemic without treatment) – (AIDS deaths during a 50 year epidemic followed by 50 years of treatment).

Vaccine and ART models use the same risk structure as above and are presented in Text S1 in [92]. A complete list of model parameters and state variables are presented in Tables S1, S2, S3, S4, S5, S6, and S7 located in Text S1 in [92]. All numerical simulations were performed in Mathematica 7.0.

Acknowledgments

We are grateful to John J. Holland, Douglas Richman, Davey Smith, Alan Perelson, Ariel Weinberger, Ruian Ke, Travis Porco, John Mittler and Matt Strain for helpful comments, and to Harish Nagarajan for technical assistance. This manuscript is dedicated to our late friend and colleague Eran Karmon who helped initiate this work with engaging discussions and enthusiasm.

Chapter 4 is a minimally modified reprint of the material as it appears in Metzger VT, Lloyd-Smith JO, Weinberger LS (2011). Autonomous Targeting of Infectious Superspreaders Using Engineered Transmissible Therapies. PLoS Computational Biology 7(3): e1002015. doi:10.1371/journal.pcbi.1002015. I was the primary investigator and author of this publication.

Chapter 5: Remarks on Molecular Simulations of Enzymes and Multi-Scale Biological Modeling

Conclusions and the way forward

Although the detailed description of protein dynamics gained from conventional molecular dynamics (CMD) simulations can be extremely useful in understanding potential mechanisms of protein or enzyme function, unfortunately many biochemically interesting protein dynamics cannot be well-explored by CMD in systems that either contain a large number of atoms and/or proteins in systems that make use of long-timescale dynamical events. In order to explore the dynamics in such systems, it is necessary to achieve enhanced conformational sampling during the course of the MD simulation so that interesting dynamics can be observed in the resulting trajectory. Numerous methods of enhanced sampling have been developed such as accelerated molecular dynamics (AMD) and are implemented in large systems like the SERCA Ca^{2+} pump imbedded in a patch of phospholipid bilayer. Without enhanced sampling via AMD, dynamical insights into systems such as SERCA would be difficult if not impossible to achieve with CMD utilizing currently-available computational power.

As computers become faster and more efficient with the recent widespread adoption of GPU clusters optimized for MD simulations and as novel methods of enhanced conformational sampling are developed, it is likely that it will someday be possible to explore the dynamics of very large proteins and/or systems that exhibit relatively slow dynamics. Through computational advances and improvements in enhanced sampling techniques, it may someday be possible to observe biologically important molecular dynamics in the majority of published protein and enzyme structures.

Future advances in simulation techniques and computer technology may someday make it possible to discover important biomolecular motions in systems containing many simultaneously interacting proteins or enzymes. Future computational advances could also lead to the development of novel mathematical models that describe the dynamics of a variety of human disease states, with each disease model making use of multiple linked biological scales of organization to better understand mechanisms of disease proliferation and to more accurately predict the efficacy of hypothetical treatments. As new protein and enzyme structures are solved in the future (assuming that computational power continues to improve) it may be possible to construct detailed multi-scale biological models of many human disease states that are each informed by the results of molecular simulations.

While the future of theoretical and computational biochemistry is exciting to imagine, it is important to acknowledge the crucial contributions made by experimental biochemists in solving previously unknown structures and meticulously studying kinetic and thermodynamic properties of biological systems. Without high-resolution structural data and experimentally validated observations and measurements, it is impossible to perform meaningful molecular simulations and to parameterize complex mathematical models of multi-scale biological systems. Finally, it is important to add that all computational results predicted from molecular simulations or biological models should ideally be verified experimentally, especially if there is disagreement between the theoretical and experimental results.

References

1. Toyoshima C (2008) Structural aspects of ion pumping by Ca2+-ATPase of sarcoplasmic reticulum. Arch Biochem Biophys 476: 3-11.

2. Winters DL, Autry JM, Svensson B, Thomas DD (2008) Interdomain fluorescence resonance energy transfer in SERCA probed by cyan-fluorescent protein fused to the actuator domain. Biochemistry 47: 4246-4256.

3. Lewis SM, Thomas DD (1992) Resolved conformational states of spin-labeled Ca-ATPase during the enzymatic cycle. Biochemistry 31: 7381-7389.

4. Toyoshima C, Asahi M, Sugita Y, Khanna R, Tsuda T. (2003) Modeling of the inhibitory interaction of phospholamban with the Ca2+ ATPase. Proc Natl Acad Sci U S A 100: 467-472.

5. Toyoshima C, Inesi G (2004) Structural basis of ion pumping by Ca2+-ATPase of the sarcoplasmic reticulum. Annu Rev Biochem 73: 269-292.

6. Sorensen TL, Moller JV, Nissen P (2004) Phosphoryl transfer and calcium ion occlusion in the calcium pump. Science 304: 1672-1675.

7. Zhang Z, Lewis D, Strock C, Inesi G, Nakasako M. (2000) Detailed characterization of the cooperative mechanism of Ca(2+) binding and catalytic activation in the Ca(2+) transport (SERCA) ATPase. Biochemistry 39: 8758-8767.

8. Huang Y, Li H, Bu Y (2009) Molecular dynamics simulation exploration of cooperative migration mechanism of calcium ions in sarcoplasmic reticulum Ca2+-ATPase. J Comput Chem 30: 2136-2145.

9. Inesi G, Lewis D, Toyoshima C, Hirata A, de Meis L (2008) Conformational fluctuations of the Ca2+-ATPase in the native membrane environment. Effects of pH, temperature, catalytic substrates, and thapsigargin. J Biol Chem 283: 1189-1196.

10. Lee AG, East JM (2001) What the structure of a calcium pump tells us about its mechanism. Biochem J 356: 665-683.

11. Einholm AP, Vilsen B, Andersen JP (2004) Importance of transmembrane segment M1 of the sarcoplasmic reticulum Ca2+-ATPase in Ca2+ occlusion and phosphoenzyme processing. J Biol Chem 279: 15888-15896.

12. Zhang Z, Lewis D, Sumbilla C, Inesi G, Toyoshima C (2001) The role of the M6-M7 loop (L67) in stabilization of the phosphorylation and Ca(2+) binding domains of the sarcoplasmic reticulum Ca(2+)-ATPase (SERCA). J Biol Chem 276: 15232-15239.

13. Musgaard M, Thogersen L, Schiott B, Tajkhorshid E (2012) Tracing cytoplasmic Ca(2+) ion and water access points in the Ca(2+)-ATPase. Biophys J 102: 268-277.

14. Costa V, Carloni P (2003) Calcium binding to the transmembrane domain of the sarcoplasmic reticulum Ca2+-ATPase: insights from molecular modeling. Proteins 50: 104-113.

15. Sugita Y, Ikeguchi M, Toyoshima C (2010) Relationship between Ca2+-affinity and shielding of bulk water in the Ca2+-pump from molecular dynamics simulations. Proc Natl Acad Sci U S A 107: 21465-21469.

16. Sugita Y, Miyashita N, Ikeguchi M, Kidera A, Toyoshima C (2005) Protonation of the acidic residues in the transmembrane cation-binding sites of the ca(2+) pump. J Am Chem Soc 127: 6150-6151.

17. Espinoza-Fonseca LM, Thomas DD (2011) Atomic-level characterization of the activation mechanism of SERCA by calcium. PLoS One 6: e26936.

18. Kekenes-Huskey PM, Metzger VT, Grant BJ, Andrew McCammon J (2012) Calcium binding and allosteric signaling mechanisms for the sarcoplasmic reticulum Ca(2)+ ATPase. Protein Sci 21: 1429-1443.

19. Inesi G, Kurzmack M, Coan C, Lewis DE (1980) Cooperative calcium binding and ATPase activation in sarcoplasmic reticulum vesicles. J Biol Chem 255: 3025-3031.

20. Durrant JD, de Oliveira CA, McCammon JA (2011) POVME: an algorithm for measuring binding-pocket volumes. J Mol Graph Model 29: 773-776.

21. Inesi G, Ma H, Lewis D, Xu C (2004) Ca2+ occlusion and gating function of Glu309 in the ADP-fluoroaluminate analog of the Ca2+-ATPase phosphoenzyme intermediate. J Biol Chem 279: 31629-31637.

22. Sorensen TL, Dupont Y, Vilsen B, Andersen JP (2000) Fast kinetic analysis of conformational changes in mutants of the Ca(2+)-ATPase of sarcoplasmic reticulum. J Biol Chem 275: 5400-5408.

23. Wade RC, Gabdoulline RR, Ludemann SK, Lounnas V (1998) Electrostatic steering and ionic tethering in enzyme-ligand binding: insights from simulations. Proc Natl Acad Sci U S A 95: 5942-5949.

24. Szabo A, Shoup D, Northrup SH, Mccammon JA (1982) Stochastically Gated Diffusion-Influenced Reactions. Journal of Chemical Physics 77: 4484-4493.

25. Toyoshima C, Nakasako M, Nomura H, Ogawa H (2000) Crystal structure of the calcium pump of sarcoplasmic reticulum at 2.6 A resolution. Nature 405: 647-655.

26. Sonntag Y, Musgaard M, Olesen C, Schiott B, Moller JV. (2011) Mutual adaptation of a membrane protein and its lipid bilayer during conformational changes. Nat Commun 2: 304.

27. Lervik A, Bresme F, Kjelstrup S (2012) Molecular dynamics simulations of the Ca2+-pump: a structural analysis. Phys Chem Chem Phys 14: 3543-3553.

28. Dode L, Vilsen B, Van Baelen K, Wuytack F, Clausen JD. (2002) Dissection of the functional differences between sarco(endo)plasmic reticulum Ca2+-ATPase (SERCA) 1 and 3 isoforms by steady-state and transient kinetic analyses. J Biol Chem 277: 45579-45591.

29. Tzeng SR, Kalodimos CG (2009) Dynamic activation of an allosteric regulatory protein. Nature 462: 368-372.

30. Li DW, Showalter SA, Bruschweiler R (2010) Entropy localization in proteins. J Phys Chem B 114: 16036-16044.

31. Zhang Z, Sumbilla C, Lewis D, Summers S, Klein MG. (1995) Mutational analysis of the peptide segment linking phosphorylation and Ca(2+)-binding domains in the sarcoplasmic reticulum Ca(2+)-ATPase. J Biol Chem 270: 16283-16290.

32. Mueller B, Zhao M, Negrashov IV, Bennett R, Thomas DD (2004) SERCA structural dynamics induced by ATP and calcium. Biochemistry 43: 12846-12854.

33. Lenoir G, Jaxel C, Picard M, le Maire M, Champeil P. (2006) Conformational changes in sarcoplasmic reticulum Ca(2+)-ATPase mutants: effect of mutations either at Ca(2+)-binding site II or at tryptophan 552 in the cytosolic domain. Biochemistry 45: 5261-5270.

34. Satoh K, Matsu-Ura T, Enomoto M, Nakamura H, Michikawa T. (2011) Highly cooperative dependence of sarco/endoplasmic reticulum calcium ATPase SERCA2a pump activity on cytosolic calcium in living cells. J Biol Chem 286: 20591-20599.

35. Rostkowski M, Olsson MH, Sondergaard CR, Jensen JH (2011) Graphical analysis of pH-dependent properties of proteins predicted using PROPKA. BMC Struct Biol 11: 6.

36. Obara K, Miyashita N, Xu C, Toyoshima I, Sugita Y. (2005) Structural role of countertransport revealed in Ca(2+) pump crystal structure in the absence of Ca(2+). Proc Natl Acad Sci U S A 102: 14489-14496.

37. Weidemuller C, Hauser K (2009) Ion transport and energy transduction of P-type ATPases: implications from electrostatic calculations. Biochim Biophys Acta 1787: 721-729.

38. Humphrey W, Dalke A, Schulten K (1996) VMD: visual molecular dynamics. J Mol Graph 14: 33-38, 27-38.

39. Brooks BR, Brooks CL, 3rd, Mackerell AD, Jr., Nilsson L, Petrella RJ. (2009) CHARMM: the biomolecular simulation program. J Comput Chem 30: 1545-1614.

40. Phillips JC, Braun R, Wang W, Gumbart J, Tajkhorshid E. (2005) Scalable molecular dynamics with NAMD. J Comput Chem 26: 1781-1802.

41. Darden T, York D, Pedersen L (1993) Particle Mesh Ewald - an N.Log(N) Method for Ewald Sums in Large Systems. Journal of Chemical Physics 98: 10089-10092.

42. Wang Y, Harrison CB, Schulten K, McCammon JA (2011) Implementation of Accelerated Molecular Dynamics in NAMD. Comput Sci Discov 4.

43. Grant BJ, Rodrigues AP, ElSawy KM, McCammon JA, Caves LS (2006) Bio3d: an R package for the comparative analysis of protein structures. Bioinformatics 22: 2695-2696.

44. Huber GA, McCammon JA (2010) Browndye: A software package for Brownian dynamics. Computer Physics Communications 181: 1896-1905.

45. Dolinsky TJ, Czodrowski P, Li H, Nielsen JE, Jensen JH. (2007) PDB2PQR: expanding and upgrading automated preparation of biomolecular structures for molecular simulations. Nucleic Acids Res 35: W522-525.

46. Baker NA, Sept D, Joseph S, Holst MJ, McCammon JA (2001) Electrostatics of nanosystems: application to microtubules and the ribosome. Proc Natl Acad Sci U S A 98: 10037-10041.

47. Northrup SH, Allison SA, Mccammon JA (1984) Brownian Dynamics Simulation of Diffusion-Influenced Bimolecular Reactions. Journal of Chemical Physics 80: 1517-1526.

48. Yu HB, Noskov SY, Roux B (2010) Two mechanisms of ion selectivity in protein binding sites. Proceedings of the National Academy of Sciences of the United States of America 107: 20329-20334.

49. Srere PA (1987) Complexes of Sequential Metabolic Enzymes. Annual Review of Biochemistry 56: 89-124.

50. Tyson JJ, Novak B (2010) Functional motifs in biochemical reaction networks. Annu Rev Phys Chem 61: 219-240.

51. Spivey HO, Ovadi J (1999) Substrate channeling. Methods 19: 306-321.

52. Eun C, Kekenes-Huskey PM, Metzger VT, McCammon JA (2014) A model study of sequential enzyme reactions and electrostatic channeling. J Chem Phys 140: 105101.

53. Cheng Y, Chang CE, Yu Z, Zhang Y, Sun M. (2008) Diffusional channeling in the sulfate-activating complex: combined continuum modeling and coarse-grained brownian dynamics studies. Biophys J 95: 4659-4667.

54. Knighton DR, Kan CC, Howland E, Janson CA, Hostomska Z. (1994) Structure of and kinetic channelling in bifunctional dihydrofolate reductase-thymidylate synthase. Nat Struct Biol 1: 186-194.

55. Elcock AH, Potter MJ, Matthews DA, Knighton DR, McCammon JA (1996) Electrostatic channeling in the bifunctional enzyme dihydrofolate reductase-thymidylate synthase. J Mol Biol 262: 370-374.

56. Yuvaniyama J, Chitnumsub P, Kamchonwongpaisan S, Vanichtanankul J, Sirawaraporn W. (2003) Insights into antifolate resistance from malarial DHFR-TS structures. Nature Structural Biology 10: 357-365.

57. Klon AE, Heroux A, Ross LJ, Pathak V, Johnson CA. (2002) Atomic structures of human dihydrofolate reductase complexed with NADPH and two lipophilic antifolates at 1.09 a and 1.05 a resolution. J Mol Biol 320: 677-693.

58. Anderson AC (2005) Two crystal structures of dihydrofolate reductase-thymidylate synthase from Cryptosporidium hominis reveal protein-ligand interactions including a structural basis for observed antifolate resistance. Acta Crystallogr Sect F Struct Biol Cryst Commun 61: 258-262.

59. Atreya CE, Anderson KS (2004) Kinetic characterization of bifunctional thymidylate synthase-dihydrofolate reductase (TS-DHFR) from Cryptosporidium hominis: a paradigm shift for ts activity and channeling behavior. J Biol Chem 279: 18314-18322.

60. Stroud RM (1994) An Electrostatic Highway. Nature Structural Biology 1: 131-134.

61. Eun C, Kekenes-Huskey PM, McCammon JA (2013) Influence of neighboring reactive particles on diffusion-limited reactions. J Chem Phys 139: 044117.

62. Kekenes-Huskey PM, Gillette A, Hake J, McCammon JA (2012) Finite Element Estimation of Protein-Ligand Association Rates with Post-Encounter Effects: Applications to Calcium binding in Troponin C and SERCA. Comput Sci Discov 5.

63. McCammon DLEaJA (1978) Brownian dynamics with hydrodynamic interactions. The Journal of Chemical Physics 69: 1352-1360.

64. Dolinsky TJ, Nielsen JE, McCammon JA, Baker NA (2004) PDB2PQR: an automated pipeline for the setup of Poisson-Boltzmann electrostatics calculations. Nucleic Acids Res 32: W665-667.

65. Li H, Robertson AD, Jensen JH (2005) Very fast empirical prediction and rationalization of protein pKa values. Proteins 61: 704-721.

66. Vanommeslaeghe K, Hatcher E, Acharya C, Kundu S, Zhong S. (2010) CHARMM general force field: A force field for drug-like molecules compatible with the CHARMM all-atom additive biological force fields. J Comput Chem 31: 671-690.

67. Holst MJ, Saied F (1995) Numerical-Solution of the Nonlinear Poisson-Boltzmann Equation - Developing More Robust and Efficient Methods. Journal of Computational Chemistry 16: 337-364.

68. Northrup, S.H., S.A. Allison, J.A. McCammon (1984) Brownian dynamics simulation of diffusion influenced bimolecular reactions. The Journal of Chemical Physics 80: 1517-1524.

69. Liu GR, Quek SS (2003) The finite element method : a practical course. Oxford ; Boston: Butterworth-Heinemann. xv, 348 p. p.

70. (2011) Automated solution of differential equations by the finite element method. New York: Springer.

71. Bauler P, Huber G, Leyh T, McCammon JA (2010) Channeling by Proximity: The Catalytic Advantages of Active Site Colocalization Using Brownian Dynamics. J Phys Chem Lett 1: 1332-1335.

72. Hamelberg D, Mongan J, McCammon JA (2004) Accelerated molecular dynamics: a promising and efficient simulation method for biomolecules. J Chem Phys 120: 11919-11929.

73. Hethcote HW, Yorke JA, Nold A (1982) Gonorrhea Modeling - a Comparison of Control Methods. Mathematical Biosciences 58: 93-109.

74. Anderson R, May R (1991) Infectious disease of humans. Dynamics and Control.

75. Woolhouse ME, Dye C, Etard JF, Smith T, Charlwood JD. (1997) Heterogeneities in the transmission of infectious agents: implications for the design of control programs. Proc Natl Acad Sci U S A 94: 338-342.

76. Lloyd-Smith JO, Schreiber SJ, Kopp PE, Getz WM (2005) Superspreading and the effect of individual variation on disease emergence. Nature 438: 355-359.

77. V P (1971) Manual of Political Economy; Kelley AM, editor. New York.

78. van de Laar T, Pybus O, Bruisten S, Brown D, Nelson M. (2009) Evidence of a large, international network of HCV transmission in HIV-positive men who have sex with men. Gastroenterology 136: 1609-1617.

79. Grassly NC, Fraser C, Garnett GP (2005) Host immunity and synchronized epidemics of syphilis across the United States. Nature 433: 417-421.

80. Woodhouse DE, Rothenberg RB, Potterat JJ, Darrow WW, Muth SQ. (1994) Mapping a social network of heterosexuals at high risk for HIV infection. AIDS 8: 1331-1336.

81. May RM, Anderson RM (1987) Transmission dynamics of HIV infection. Nature 326: 137-142.

82. Woolhouse ME (1998) Patterns in parasite epidemiology: the peak shift. Parasitol Today 14: 428-434.

83. DMERI SITf, Sgh (2005) Strategies adopted and lessons learnt during the severe acute respiratory syndrome crisis in Singapore. Rev Med Virol 15: 57-70.

84. Baggaley RF, Garnett GP, Ferguson NM (2006) Modelling the impact of antiretroviral use in resource-poor settings. PLoS Med 3: e124.

85. Kahn JG (1996) The cost-effectiveness of HIV prevention targeting: how much more bang for the buck? Am J Public Health 86: 1709-1712.

86. Cowan FM, Hargrove JW, Langhaug LF, Jaffar S, Mhuriyengwe L. (2005) The appropriateness of core group interventions using presumptive periodic treatment among rural Zimbabwean women who exchange sex for gifts or money. J Acquir Immune Defic Syndr 38: 202-207.

87. Fields BN, Knipe DM (1990) Fields virology: Raven Press.

88. Klimatcheva E, Planelles V, Day SL, Fulreader F, Renda MJ. (2001) Defective lentiviral vectors are efficiently trafficked by HIV-1 and inhibit its replication. Mol Ther 3: 928-939.

89. Levine BL, Humeau LM, Boyer J, MacGregor RR, Rebello T. (2006) Gene transfer in humans using a conditionally replicating lentiviral vector. Proc Natl Acad Sci U S A 103: 17372-17377.

90. An DS, Morizono K, Li QX, Mao SH, Lu S. (1999) An inducible human immunodeficiency virus type 1 (HIV-1) vector which effectively suppresses HIV-1 replication. J Virol 73: 7671-7677.

91. Weinberger LS, Schaffer DV, Arkin AP (2003) Theoretical design of a gene therapy to prevent AIDS but not human immunodeficiency virus type 1 infection. J Virol 77: 10028-10036.

92. Metzger VT, Lloyd-Smith JO, Weinberger LS (2011) Autonomous targeting of infectious superspreaders using engineered transmissible therapies. PLoS Comput Biol 7: e1002015.

93. Aaskov J, Buzacott K, Thu HM, Lowry K, Holmes EC (2006) Long-term transmission of defective RNA viruses in humans and Aedes mosquitoes. Science 311: 236-238.

94. Fine PE, Carneiro IA (1999) Transmissibility and persistence of oral polio vaccine viruses: implications for the global poliomyelitis eradication initiative. Am J Epidemiol 150: 1001-1021.

95. Weinberger LS, Burnett JC, Toettcher JE, Arkin AP, Schaffer DV (2005) Stochastic gene expression in a lentiviral positive-feedback loop: HIV-1 Tat fluctuations drive phenotypic diversity. Cell 122: 169-182.

96. Chen J, Nikolaitchik O, Singh J, Wright A, Bencsics CE. (2009) High efficiency of HIV-1 genomic RNA packaging and heterozygote formation revealed by single virion analysis. Proc Natl Acad Sci U S A 106: 13535-13540.

97. Perelson AS, Neumann AU, Markowitz M, Leonard JM, Ho DD (1996) HIV-1 dynamics in vivo: virion clearance rate, infected cell life-span, and viral generation time. Science 271: 1582-1586.

98. Fraser C, Hollingsworth TD, Chapman R, de Wolf F, Hanage WP (2007) Variation in HIV-1 set-point viral load: epidemiological analysis and an evolutionary hypothesis. Proc Natl Acad Sci U S A 104: 17441-17446.

99. Mellors JW, Rinaldo CR, Jr., Gupta P, White RM, Todd JA. (1996) Prognosis in HIV-1 infection predicted by the quantity of virus in plasma. Science 272: 1167-1170.

100. Granich RM, Gilks CF, Dye C, De Cock KM, Williams BG (2009) Universal voluntary HIV testing with immediate antiretroviral therapy as a strategy for elimination of HIV transmission: a mathematical model. Lancet 373: 48-57.

101. Montaner JS, Hogg R, Wood E, Kerr T, Tyndall M. (2006) The case for expanding access to highly active antiretroviral therapy to curb the growth of the HIV epidemic. Lancet 368: 531-536.

102. Garnett GP, Baggaley RF (2009) Treating our way out of the HIV pandemic: could we, would we, should we? Lancet 373: 9-11.

103. Fox MP, Rosen S (2010) Patient retention in antiretroviral therapy programs up to three years on treatment in sub-Saharan Africa, 2007-2009: systematic review. Trop Med Int Health 15 Suppl 1: 1-15.

104. Rosen S, Fox MP, Gill CJ (2007) Patient retention in antiretroviral therapy programs in sub-Saharan Africa: a systematic review. PLoS Med 4: e298.

105. Rosen S, Sanne I, Collier A, Simon JL (2005) Rationing antiretroviral therapy for HIV/AIDS in Africa: choices and consequences. PLoS Med 2: e303.

106. Baggaley RF, Griffin JT, Chapman R, Hollingsworth TD, Nagot N. (2009) Estimating the public health impact of the effect of herpes simplex virus suppressive therapy on plasma HIV-1 viral load. AIDS 23: 1005-1013.

107. Rerks-Ngarm S, Pitisuttithum P, Nitayaphan S, Kaewkungwal J, Chiu J. (2009) Vaccination with ALVAC and AIDSVAX to prevent HIV-1 infection in Thailand. N Engl J Med 361: 2209-2220.

108. Keele BF, Giorgi EE, Salazar-Gonzalez JF, Decker JM, Pham KT. (2008) Identification and characterization of transmitted and early founder virus envelopes in primary HIV-1 infection. Proc Natl Acad Sci U S A 105: 7552-7557.

109. Haaland RE, Hawkins PA, Salazar-Gonzalez J, Johnson A, Tichacek A. (2009) Inflammatory genital infections mitigate a severe genetic bottleneck in heterosexual transmission of subtype A and C HIV-1. PLoS Pathog 5: e1000274.

110. Learn GH, Muthui D, Brodie SJ, Zhu T, Diem K. (2002) Virus population homogenization following acute human immunodeficiency virus type 1 infection. J Virol 76: 11953-11959.

111. Dukers NH, Goudsmit J, de Wit JB, Prins M, Weverling GJ. (2001) Sexual risk behaviour relates to the virological and immunological improvements during highly active antiretroviral therapy in HIV-1 infection. AIDS 15: 369-378.

112. Blower SM, Gershengorn HB, Grant RM (2000) A tale of two futures: HIV and antiretroviral therapy in San Francisco. Science 287: 650-654.

113. Barouch DH (2008) Challenges in the development of an HIV-1 vaccine. Nature 455: 613-619.

114. Kirkwood TB, Bangham CR (1994) Cycles, chaos, and evolution in virus cultures: a model of defective interfering particles. Proc Natl Acad Sci U S A 91: 8685-8689.

115. Endy D, Yin J (2000) Toward antiviral strategies that resist viral escape. Antimicrob Agents Chemother 44: 1097-1099.

116. Read AF, Lynch PA, Thomas MB (2009) How to make evolution-proof insecticides for malaria control. PLoS Biol 7: e1000058.

117. Temin HM (1993) Retrovirus variation and reverse transcription: abnormal strand transfers result in retrovirus genetic variation. Proc Natl Acad Sci U S A 90: 6900-6903.

118. Davis BM, Humeau L, Dropulic B (2004) In vivo selection for human and murine hematopoietic cells transduced with a therapeutic MGMT lentiviral vector that inhibits HIV replication. Mol Ther 9: 160-172.

119. Mukherjee R, Plesa G, Sherrill-Mix S, Richardson MW, Riley JL. (2010) HIV sequence variation associated with env antisense adoptive T-cell therapy in the hNSG mouse model. Mol Ther 18: 803-811.

120. Pike-Overzet K, van der Burg M, Wagemaker G, van Dongen JJ, Staal FJ (2007) New insights and unresolved issues regarding insertional mutagenesis in X-linked SCID gene therapy. Mol Ther 15: 1910-1916.

121. Bordignon C, Notarangelo LD, Nobili N, Ferrari G, Casorati G. (1995) Gene therapy in peripheral blood lymphocytes and bone marrow for ADA- immunodeficient patients. Science 270: 470-475.

122. Blower SM, McLean AR (1994) Prophylactic vaccines, risk behavior change, and the probability of eradicating HIV in San Francisco. Science 265: 1451-1454.